TRANSIENT PHOTOLUMINESCENCE SPECTROSCOPY OF GaAs, ZnSe AND GaAs/GaAlAs QUANTUM WELLS

by

Sylvain Charbonneau

B.Sc., University of Ottawa, 1983
M.Sc., University of Ottawa, 1985

THESIS SUBMITTED IN PARTIAL FULFILLMENT OF

THE REQUIREMENTS FOR THE DEGREE OF

DOCTOR OF PHILOSOPHY

in the Department

of

Physics

© Sylvain Charbonneau 1988

SIMON FRASER UNIVERSITY

September 1988

All rights reserved. This work may not be
reproduced in whole or in part, by photocopy
or other means, without permission of the author.

APPROVAL

Name: Sylvain Charbonneau

Degree: Ph.D. Physics

Title of Thesis: Transient Photoluminescence Spectroscopy of GaAs, ZnSe and GaAs/GaAlAs Quantum Wells

Examining Committee:

Chairman: Dr. D.H. Boal

Dr. M.L.W. Thewalt
Senior Supervisor

Dr. B.P. Clayman

Dr. R.F. Frindt

Dr. J.C. Irwin

Dr. M. Plischke

Dr. A.P. Roth
External Examiner
Division of Physics
National Research Council, Ottawa

Date Approved: September 8, 1988

PARTIAL COPYRIGHT LICENSE

I hereby grant to Simon Fraser University the right to lend my thesis, project or extended essay (the title of which is shown below) to users of the Simon Fraser University Library, and to make partial or single copies only for such users or in response to a request from the library of any other university, or other educational institution, on its own behalf or for one of its users. I further agree that permission for multiple copying of this work for scholarly purposes may be granted by me or the Dean of Graduate Studies. It is understood that copying or publication of this work for financial gain shall not be allowed without my written permission.

Title of Thesis/Project/Extended Essay

Transient Photoluminescence Spectroscopy of GaAs, ZnSe and GaAs/GaAlAs Quantum Wells

Author: ______________
(signature)

Sylvain Charbonneau
(name)

Sept 23 1988
(date)

ABSTRACT

The generation of extremely short tunable laser pulses has opened the way for the study of fast transient phenomena such as exciton recombination in direct gap semiconductors. Using high spectral resolution resonant excitation measurements, combined with a novel time rejection technique, we have completed a comprehensive study of the nature and properties of a series of luminescence lines observed in the 1504-1511 meV region in GaAs grown by molecular beam epitaxy (MBE). These lines were found to be due to excitons bound to a series of axial defects having the electronic characteristics of double acceptors. Zeeman measurements were also performed in order to support this model.

In another investigation, intense laser light excitation was used to create high concentrations of free carriers and excitons in various semiconductors. When such high densities of excitons are achieved, a number of new effects can be observed, such as the formation of biexcitons (or excitonic molecules). The binding energies of these excitonic molecules were obtained experimentally for high-purity bulk ZnSe and GaAs, and found to be in good agreement with available theories. GaAs/GaAlAs quantum wells (QW) were also studied under high excitation intensities, and the results showed that biexcitons can also be created in such structures, but that care must be taken in order that they not be confused with extrinsic bound excitons.

Photoluminescence (PL), PL excitation and time-resolved spectroscopy were also employed to interpret fine structure observed in GaAs/GaAlAs single QW grown by MBE under conditions of interrupted

growth. This structure has been interpreted as originating within smooth regions in the QW layer differing in width by exactly one monolayer. Finally, a detailed experimental study of the influence of electric fields on exciton lifetimes in a GaAs/GaAlAs coupled double quantum well structure was undertaken. The decay time of the exciton peak was found to increase by over an order of magnitude as the electric field was increased. This increase is attributed to the change of the nature of the lowest energy exciton transition from spatially direct to spatially indirect.

ACKNOWLEDGEMENT

I would like to thank my supervisor, Dr. Mike Thewalt, for his support, encouragement, and guidance during the course of this research. Without his ideas, suggestions and experimental skills, none of these experiments would have been possible.

I would like to thank Dr. Emil Koteles from GTE Laboratories, Dr. T.D. Harris from Bell Laboratories and Dr. M. Isshiki from Tohoku University for providing me with the various samples used in this work.

To Doreen I express my everlasting gratitude for being with me every page of the way.

I would like to express my thanks to the staff and faculty of the Physics Department who generously gave their time, knowledge, and use of their equipment and facilities.

Finally, the financial support of the Natural Sciences and Engineering Research Council, Simon Fraser University and Dr. M. Thewalt are also gratefully acknowledged.

TABLE OF CONTENTS

Approval ii

Abstract iii

Acknowledgement v

List of Tables vii

List of Figures viii

List of Abbreviations xi

Chapter 1. Excitons In Semiconductors 1
1.1 Free Excitons 1
1.2 Bound Excitons 7
1.3 Donor-Acceptor Pair Recombination 14
1.4 Confined Excitons in 2-Dimensions 17

Chapter 2. Experimental Methods 24
2.1 Introduction 24
2.2 Lasers as Spectroscopic Light Sources 25
2.3 Spectroscopic Instrumentation 39
2.4 Time-Resolved Spectroscopy 43

Chapter 3. Defect-Induced Bound Excitons in MBE GaAs 49
3.1 Introduction 49
3.2 Proposed Models for the DIBE 54
3.3 Nonresonant Excitation 59
3.4 Time-Resolved PL Spectra 67
3.5 Photoluminescence Excitation Spectra 69
3.6 Resonant Excitation of the DIBE Lines 72
3.7 Zeeman Spectroscopy 94
3.8 Model for the Transitions 99
3.9 Conclusion 106

Chapter 4. Excitons at High Density 109
4.1 Introduction 109
4.2 Radiative Recombination in Highly-Excited ZnSe.. 111
4.3 Time Evolution of the Biexcitons in Bulk GaAs .. 125
4.4 Optical Investigation of Biexcitons and Bound Excitons in GaAs Quantum Wells 132
4.5 Conclusion 142

Chapter 5. Photoluminescence of Excitons in Quantum Wells 143
5.1 Introduction 143
5.2 Photoluminescence Study of Single QW Fabricated Under Conditions of Interrupted Growth 144
5.3 Effect of Electric Fields on Excitons in a Coupled Double QW Structure 156
5.4 Concluding Remarks 168

Chapter 6. Conclusions 170

References 172

LIST OF TABLES

Table		Page
2.1	Detector Response	42
3.1	Shallow Donor and Acceptor Binding Energies in GaAs	50
3.2	Recombination Processes in GaAs at 4.2 K	53
3.3	Binding Energies of the KP Lines	85

LIST OF FIGURES

Figure		Page
1.1	Energy level diagram of a GaAs/AlGaAs superlattice	20
2.1	(a) Commercial tuning wedge; (b) Tilted birefringent plate	28
2.2	(a) Spectrum of the cavity modes of a laser; (b) Multimode laser output for constant phases	32
2.3	Schematic diagram of the experimental setup for performing time-resolved PL	45
2.4	Experimental system depicting the imaging detector and its associated electronics	47
3.1	Comparison of MOCVD-GaAs and MBE-GaAs PL spectra	52
3.2	High-resolution PL spectrum of the KP series	60
3.3	PL spectra of MBE-GaAs under different excitation power ..	63
3.4	PL emission spectrum of MBE-GaAs using above gap excitation	65
3.5	Series of time-resolved spectra of the KP lines taken at 1.8 K	68a
3.6	Luminescence decay measurement of some of the KP lines ...	68b
3.7	PLE spectra of the defect-bound exciton region from 1504 to 1511 meV	71
3.8	Time-resolved selective-excitation PL spectrum obtained using the parallel collection system	74
3.9	PL spectra of MBE-GaAs with the dye laser energy tuned to the polariton and line 47	76
3.10	Selectively excited PL spectra with the laser tuned to resonance with different lines of the KP series (lines 42 to 22)	78
3.11	Resonantly excited two-hole replica spectra of some of the KP lines (8-19)	79
3.12	Summary of the resonant PL measurements in the two-hole replica region	82
3.13	Comparison of the BE localization energy for the KP lines <u>vs</u> the acceptor binding energies	86

3.14 The d_n PL spectra using CW and pulse excitation compared with a simulated spectra 88

3.15 Δ replicas obtained by resonantly exciting some of the KP lines 90

3.16 A plot of the KP acceptor binding energy and ground state splitting *vs* KP line energy 91

3.17 Luminescence decay measurement of the 2S two-hole excited states of various KP lines 93

3.18 Nonselective Zeeman PL spectrum at 7 Tesla 96

3.19 Zeeman splitting pattern of line 14 for two magnetic field directions 98

3.20 Energy level diagram for individual centres of the KP series at zero and finite magnetic field 101

3.21 Δ-replicas obtained from resonant excitation of line 14 under a field of 6.9 Tesla 104

3.22 Energy level scheme for resonant excitation of line 14 at 6.9 Tesla 105

4.1 PL spectra of high-purity ZnSe under different excitation powers 113

4.2 Luminescence decay of various ZnSe exciton lines using a peak power of 0.2 kW/cm^2 120

4.3 Luminescence decay of various ZnSe exciton lines using a pump intensity of 3 kW/cm^2 121

4.4 Luminescence decay of ZnSe exciton lines under high excitation intensity 123

4.5 PL spectra of high-purity bulk GaAs under two excitation intensities 128

4.6 Luminescence decay of the free exciton and the biexciton in bulk GaAs 129

4.7 Time-resolved PL spectra of highly excited bulk GaAs 130

4.8 PL spectra of two GaAs quantum wells under different excitation powers 137

4.9 Luminescence decay of the n=1 heavy-hole exciton and the biexciton under different conditions of excitation 138

4.10 Luminescence decay of the n=1 heavy-hole exciton and a donor bound exciton in GaAs QW 140

5.1 PL spectra of a GaAs/AlGaAs QW measured at various temperatures 148

5.2 PLE spectra of a GaAs/AlGaAs QW measured at various temperatures 150

5.3 Schematic diagram illustrating the smoothness of the normal and inverted interfaces 152

5.4 Evolution of the PL peaks as a function of time after the laser pulse for a GaAs QW 154

5.5 PL decay curves for the various peaks observed in a GaAs/AlGaAs QW 155

5.6 Schematic diagrams of the energy levels of a single QW and a symmetrical CDQW 159

5.7 PLE spectra of a CDQW under various bias voltages 162

5.8 Evolution of the PL peaks as a function of time after pulse excitation in a CDQW 164

5.9 Luminescence decay of exciton peaks in a CDQW under various bias voltages 166

5.10 Energies and lifetimes of exciton peaks as a function of forward bias voltage in a CDQW 167

LIST OF ABBREVIATIONS

BE	Bound Exciton
CB	Conduction Band
CDQW	Coupled Double Quantum Well
CFD	Constant Fraction Discriminator
CW	Continuous Wave
DAP	Donor-Acceptor Pair
DIBE	Defect-Induced Bound Exciton
EMA	Effective Mass Approximation
FE	Free Exciton
FSR	Free Spectral Range
FWHM	Full Width Half Maximum
HH	Heavy-Hole
KE	Kinetic Energy
LH	Light-Hole
LO	Longitudinal Optical
MBE	Molecular Beam Epitaxy
MCP	Microchannel-Plate
PHA	Pulse-Height Analyzer
PL	Photoluminescence
PLE	Photoluminescence Excitation
PM	Photomultiplier
QCSE	Quantum-Confined Stark Effect
QW	Quantum Well
SCA	Single Channel Analyzer
SL	Superlattice
SPL	Selectively Excited Pair Luminescence
SQW	Single Quantum Well
TAC	Time-to-Amplitude Converter
TO	Transverse Optical
VB	Valence Band

CHAPTER 1

EXCITONS IN SEMICONDUCTORS

1.1 Free Excitons

The absorption spectrum of light near the fundamental edge in pure direct gap semiconductors reveals two different kinds of electronic transitions. At photon energies greater than the energy gap, the absorption of light corresponds to processes in which a free electron is transferred to the conduction band (CB) and a free hole is left in the valence band (VB). At energies lower than the energy gap there are absorption peaks which correspond to processes in which the conduction electron and the valence hole are bound to one another, via the long range Coulomb interaction in states within the forbidden energy gap. Such mutually bound electron-hole pair states are called free excitons (FE). The centre of mass of the exciton can move through the crystal by diffusion, just like the individual electronic particles. However, this exciton migration does not produce electrical conductivity, since each exciton contains a pair of charges of opposite sign.

Two forms of excitons were postulated in the 1930's, one involving a very localized state, the Frenkel exciton[1.1] and the other, by contrast a much more extended state, the Wannier-Mott exciton.[1.2] The Frenkel exciton has a radius comparable with the interatomic separation and is typically exemplified in strongly ionic crystals with low mobility and dielectric constant, as in alkali halides. According to quantum- mechanical principles, one would expect the binding energy of

the exciton to be large, due to the high degree of localization. The Wannier-Mott exciton is found in materials of opposite extremes – those having a large degree of covalent bonding, high mobility and large dielectric constant, as in type IV and III-V semiconductors. In such cases, one finds the FE binding energy in the meV range. Furthermore, the wavefunction describing the interacting electron and hole pair separation extends over many unit cells of the crystal.

Because the exciton is a two-particle system, the general problem of calculating its energy levels and wavefunctions is, in principle, more complicated than the one electron problem. However, in the limit where the electron and hole are separated by many inter-atomic spacings, one can use the effective mass approximation (EMA)[1.3] and the problem simplifies enormously. In the EMA, the properties of the solid are combined into the effective masses of the interacting electron and hole m_e^* and m_h^* and the dielectric constant.

Let us assume that a free-hole and electron are created in a direct gap material and attract each other. If they are so far apart that the atomic structure of the crystal can be ignored, their mutual potential can be written as:

$$V(r) = -e^2/\epsilon r \qquad (1.1)$$

where r is the electron-hole separation and ϵ is the dielectric constant which takes into account the screening of the Coulomb potential by the polarizability of the host lattice. A Coulomb potential like equation (1.1) gives rise to an infinite series of discrete hydrogenic bound states, with energies given by[1.4]

$$E_n(K) = \frac{-e^4\mu}{2\hbar^2\epsilon^2 n^2} + \frac{\hbar^2 K^2}{2M} \qquad (1.2)$$

where $n = 1,2,\ldots\infty$, $\mu^{-1} = (m_e^*)^{-1} + (m_h^*)^{-1}$, $M = m_e^* + m_h^*$, $\hbar K$ is the momentum of the centre of mass, and E_n is measured from the band edge E_g. Pursuing the analogy with the hydrogen atom, one could evaluate the wave function of the n = 1 exciton ground state to be[1.4]

$$\psi_{1S}(r) = (\pi a_x^3)^{-1/2} e^{-r/a_x} \qquad (1.3)$$

and the most probable value of r is a_x, the FE Bohr radius given by

$$a_x = \frac{\hbar^2\epsilon}{\mu e^2} . \qquad (1.4)$$

The binding energy of the n = 1 FE, relative to a free electron-hole pair at the band edge, often called the "exciton Rydberg", is

$$R_x = \frac{\mu e^4}{2\hbar^2\epsilon^2} = \frac{e^2}{2\epsilon a_x} = \frac{\hbar^2}{2\mu a_x^2} . \qquad (1.5)$$

Equation (1.5) provides a convenient way of estimating a_x from R_x if the value of ϵ or of μ is unknown. R_x can be very small; for example, in GaAs, for which $\mu = 0.058\ m_o$ (m_o is the free-electron mass) and ϵ = 12.5, one obtains $R_x = 5$ meV and $a_x \simeq 110$Å. Such an exciton is clearly only going to be stable at very low temperatures.

Ultimately, the electron and hole forming the FE can radiatively recombine creating a slightly below band gap photon. Since wavevector

must be conserved upon FE annihilation, momentum selection rules require that only zero kinetic energy (KE) excitons can recombine radiatively. However, this condition does not prevent excitons from possessing KE. Exciton emission at other than zero KE can occur through phonon participation. Phonons provide additional means of satisfying the momentum selection rules and thereby reduce the restriction on the exciton momentum, allowing excitons of finite $\vec{K}$ to annihilate.

Now let us consider two ways for which FE can annihilate. Let $\vec{k}$ be the photon wavevector and E_x be the exciton energy $E_x = E_g - \left(\frac{R_x}{n^2}\right) + E_{kin}(\vec{K})$. First, in the no-phonon region of the spectrum, conservation of energy and momentum require that

$$\vec{K} = \vec{k} \cong 0 \qquad (1.6a)$$

$$\hbar\omega = E_x \, . \qquad (1.6b)$$

Thus only stationary FE, with centre of mass momentum $\vec{K} = 0$ can contribute to radiative emission, resulting in a sharp spike for the FE no-phonon line shape. In real life, however, the FE no-phonon line shape is always broadened. This broadening has been calculated in several approximations by Toyozawa.(1.5) In his paper he assumed that the linewidth was essentially determined by the lifetime of $\vec{K} = 0$ excitons before they are scattered to other momentum states $\vec{K} \neq 0$ by phonons. It is known that an eigenstate can be perfectly sharp only if its lifetime is infinite. If its lifetime is finite, then, according to the relation $\Delta E \Delta\tau > \hbar$, some uncertainty in its energy is necessary. In this way, the width of the FE line is determined in part by all of the processes which limit the time that the exciton spends in the $\vec{K} = 0$

state, including phonon scattering. Toyazawa[1.5] obtained analytical expressions for the line shapes in the two limiting cases of weak and strong phonon coupling. For weak coupling, a Lorentzian curve was obtained, whereas a Gaussian curve was obtained for strong exciton-phonon coupling. Other effects may obscure the expected line shape. Crystal imperfections, impurities, and strains can cause inhomogeneous broadening of the FE line.

In direct gap material the principal (no phonon) luminescence should be very narrow since, due to crystal momentum conservation, only excitons near $\vec{K} = 0$ can recombine to form photons. However, phonon replicas are possible via emission of zone centre optical phonons ($\vec{k} \simeq 0$), and these show the true free exciton Maxwell-Boltzmann distribution since here the phonon can take up the initial momentum of the free exciton. Consider such an emission process for which one phonon of energy $\hbar\omega_{ph}$ and momenta $\vec{q}_{ph}$ is emitted. From energy and momenta consideration one requires

$$\vec{K} = \vec{k} + \vec{q}_{ph} \tag{1.7a}$$

$$\hbar\omega = E_x - \hbar\omega_{ph} \ . \tag{1.7b}$$

In polar material like GaAs, the longitudinal optical (LO) phonon coupling is by far the strongest because of the polarization field associated with it. The optical phonon energies are usually nearly independent of momentum, thus $\hbar\omega_{LO}$ is the same for all $\vec{q}_{LO}$.[1.6] It follows that the phonon replica is not significantly broadened by phonon dispersion and occurs at a photon energy of

$$\hbar\omega = E_x - \hbar\omega_{LO} . \quad (1.8)$$

Assuming $\hbar\omega_{LO}$ to be independent of $\vec{q}_{LO}$, the total exciton energy E_x contains the KE of exciton motion and thus depends on the value of $\vec{K}$. Equation (1.8) can be rewritten as

$$\hbar\omega = E_g - (R_x/n^2) + \left(\frac{\hbar^2 K^2}{2M}\right) - \hbar\omega_{LO} . \quad (1.9)$$

As discussed previously, some of the causes of broadening of the zero phonon exciton emission originated from phonon scattering of the exciton out of the $K = 0$ state and also from perturbations due to crystal defects. Another process that can be important under certain circumstances, is that of phonon-assisted transitions involving acoustic phonons. Acoustical-phonon-assisted transitions are completely analogous to the optical phonon assisted case except that their energies are much smaller, so that the acoustic phonons act to broaden the zero phonon emission rather than generate a separate, observable emission line. Nevertheless, the presence of acoustic phonons relaxes the momentum selection rules so that excitons of any KE can be annihilated.

Under certain circumstances, the binding energy of an exciton can be decreased by the presence of a point defect or an impurity such as a donor or an acceptor. Energy is the fundamental criterion that determines whether or not an exciton can be trapped on an impurity. If the total energy of the system is reduced when the exciton is in the vicinity of an impurity, then it is energetically favorable for the FE to remain near the defect; at a low enough temperature the exciton becomes *bound* to the impurity to form a bound exciton.

1.2 Bound Excitons[1.7]

The existence of bound exciton (BE) states was predicted in 1958, when the analogy between the hydrogen molecule and an exciton interacting with a shallow neutral donor or acceptor (which can, like an exciton, be described by the hydrogenic model) became recognized.[1.7] Just as the hydrogen atoms bind to each other in the H_2 molecule, so should the exciton be bound to the neutral impurity. It was established by Hopfield[1.8] and Herbert[1.9] that the BE stability criterion depended on the electron-hole effective mass ratio ($\sigma = m_e^*/m_h^*$). They concluded that excitons bound to neutral impurities were stable for all possible mass ratios, whereas excitons bound to ionized impurities were stable only for restricted values of σ. In GaAs, for example where $m_e^* \ll m_h^*$, an exciton bound to an ionized donor is stable while an exciton bound to an ionized acceptor is not.

The theory of BE shares many of the difficulties which affect all theories of bound states in semiconductors. The basic approximation in semiconductors is normally the effective mass theory, and the major problem is then to treat the interparticle correlations. Effective mass theory provides an admirable qualitative approximation in many cases. However, to make detailed comparisons of theory and experiment, it is essential to be aware of the nature of the many corrections. The most difficult corrections to consider quantitatively are the central cell terms which arise from differences in the impurity and host core potentials, and from associated strain fields.

A BE line is distinguished optically from a FE line by its extremely narrow linewidth, since unlike a FE, a BE is localized and

does not have a Boltzmann tail associated with thermal motion. A BE, upon annihilation, gives off a photon of energy less than that of a FE. This difference in energy is usually referred to as the exciton localization energy E_{BX}. For impurity states dominated by the Coulomb attraction, the central cell corrections often lead to a linear variation of E_{BX} with increasing impurity binding energy (E_i) of the form

$$E_{BX} = a + bE_i \ . \tag{1.10}$$

In this relation, known as Haynes' rule,(1.10) a and b are constants for a given material. Dean(1.11) and Baldereschi(1.12) have used an idea to explain the general trend by using first-order perturbation theory. They introduced a central cell potential V_c and assumed a linear dependence of binding energy on V_c of the form

$$E_i = (E_i)_{EM} + V_c \rho_c \tag{1.11a}$$

$$E_{BX} = (E_{BX})_{EM} + V_c \delta\rho_c \tag{1.11b}$$

where the subscript EM refers to the effective mass binding energy obtained with zero central cell correction, ρ_c is the electronic charge in the central region for the neutral impurity state and $\delta\rho_c$ denotes the increased charge obtained with the exciton present. These equations can be combined in the form

$$E_{BX} = \left[(E_{BX})_{EM} - (E_i)_{EM} \frac{\delta\rho_c}{\rho_c}\right] + \frac{\delta\rho_c}{\rho_c} E_i \ . \tag{1.12}$$

This equation has the form of (1.10) with

$$a = \left[(E_{BX})_{EM} - (E_i)_{EM} \frac{\delta\rho_c}{\rho_c}\right] \quad \text{and} \quad b = \frac{\delta\rho_c}{\rho_c} . \qquad (1.13)$$

For the shallow centres observed in direct gap materials like GaAs where $m_e^* \ll m_h^*$, it is found that E_{BX} is fairly insensitive to E_i for neutral acceptors, but not for donors.(1.13) It is expected that electron-hole exchange interactions dominate the exciton binding for weak central cell corrections. In the case of a neutral acceptor BE, a central cell correction will contract the two-hole orbitals, tending to increase the binding energy. However, the electron state remains diffuse due to its low mass. Consequently the electron-hole correlation can be reduced and offsets the increase in binding from the central cell correction. For the donor BE, the heavy-hole is pinned at the electron radius in the effective mass state, and can follow the electron orbital contraction for a weak central cell correction so that the electron-hole correlation is not initially reduced.

The above discussion of Haynes' rule has treated central cell corrections as a perturbation on the long-range Coulomb potential which was discussed approximately using the effective mass theory. However, the use of the effective mass equation to describe exciton binding assumes that the crystal lattice is static. In practice, localized states couple to the lattice through the electron-phonon interaction, and this can cause local lattice distortion and a strain contribution to the binding energy. As discussed in section 1.1 for the free exciton, when an electron and a hole are created or recombine, this coupling can

also lead to the emission of one or more phonons, giving replicas of the principal bound exciton line displaced by the energies of the relevant phonons. The electron-phonon interaction is often dominated by long wavelength longitudinal optical modes. This is particularly true for compound semiconductors because of the electric field carried with their lattice vibrations. In polar semiconductors like GaAs, there are two ways the optical phonons can interact with an exciton. First, the lattice displacement of the optical phonon produces the usual deformation potential coupling with the exciton. Since the LO phonon also produces a longitudinal electric field, there is an additional interaction due to the Coulomb interaction between this field and the charges in the exciton. This second interaction is usually referred to as the Fröhlich interaction.[1.14] The most important difference between the deformation potential interaction and the Fröhlich interaction is in their dependences on the phonon wave vector q. The deformation potential, being a short-range interaction, is not dependent on q. On the other hand, the Fröhlich interaction is strongly dependent on q.

The principal cause of low energy satellite luminescence structure of purely electronic origin are the transitions to low-lying excited states of the centre to which the exciton is bound. Transitions to the ground electronic state are responsible for the principal BE luminescence lines. The satellite structure described here involves photon energy displacements below the principal BE line equal to the excitation energies of the centre binding the exciton. The processes responsible for these satellites were termed *two-electron* transitions in the case of donor BE (or *two-hole* transitions for acceptor BE) to

acknowledge a conceptual picture in which the BE recombines, simultaneously producing an excitation of the second electron in the BE complex, or a second hole for a neutral acceptor BE.

For some semiconductors having large band gap, the difference between the principal impurity BE energies is sufficiently great and the control of the chemistry sufficiently good that the principal BE transitions of different impurities can be distinguished. The different impurities can also be identified from the more substantial differences in the displacement energies of the two-electron or two-hole satellites. These differences are dominated by central cell corrections in the ground states. This impurity identification from the BE transitions is no longer possible for semiconductors like GaAs, where the large reduction in m_e^* causes a decrease of the binding energies and an increase in the radius of the bound state of the donors. The latter effect greatly reduces the differences in central cell shifts between different donors, to the point where all donors in GaAs have E_D (Donor binding energy) within a range of only ~0.2 meV.[1.15] Therefore, one has to look for chemical shifts which are small compared with the small energy differences between BE states. This has prevented the progress of chemical identification of donors through their BE spectra in GaAs.

The situation is very different for acceptors in direct gap semiconductors where the ionization energies and differential chemical shifts are far less dependent on the band gap because of the influence of the heavy-hole component of the degenerate valence band structure at the centre of the reduced zone. In materials that crystallize in the zinc-blende structure, such as GaAs, the valence band is degenerate at the Γ point, complicating the effective mass theory for treating the

acceptors in these materials. It might be expected that the higher excited states of the acceptors could be explained by the hydrogenic model. Lipari and Baldereschi[1.16] have presented calculations of the energy levels of the effective mass acceptors in narrow gap III-V semiconductors. Because of the core effects giving rise to the central cell corrections or chemical shifts, the ground state, which is relatively highly localized, was found to suffer greater perturbations and to exhibit a greater increase in binding energy than any of the excited states. Such chemical shifts apply particularly to the S states which do not avoid the region of the central cell. As a consequence of this, one would expect different acceptors to have appreciably different ground state binding energies.

The principal acceptor BE luminescence occurs when an exciton bound to the neutral acceptor site recombines and leaves the acceptor in its ground state (1S). Since crystal field effects are small for such shallow states, the parity selection rule allows this transition and indeed transitions to other levels of the acceptor such as 2S, 3S, 4S etc. The spectral shift from the fundamental BE emission to the first of these replicas represents the excitation energy of the 2S level. This energy is an internal transition energy of the acceptor and can be compared with the results of the theoretical calculations.[1.16] Therefore, these experiments not only provide central cell corrections to the ground state, but also for the first S excited state (2S). For true hydrogenic-type wavefunctions, the central cell effect should fall off as $(1/n)^3$, where n is the principal quantum number. Therefore, one would expect the central cell corrections to the 2S level to be about 1/8 of those found for the ground states 1S. For n = 3S and 4S states,

the central cell should not be detectable.

The neutral impurity wavefunction, as well as the FE wavefunction, are very extended. For example, the FE Bohr radius a_x in GaAs is ~100Å and the Bohr radius of an effective mass-like donor and acceptor are ~100Å and ~30Å respectively. Thus the large FE radius a_x leads to a correspondingly large cross-section σ ($\sim a_x^2 \sim 10^{-12}$ cm^2) for capture by an impurity. A free exciton at 2K has a velocity $v \sim 10^6$ cm/s, so for an impurity concentration $N \sim 10^{15}$ cm^{-3}, its lifetime before capture is expected to be $(N\sigma v)^{-1} \sim 10^{-9}$ s. This is comparable to the radiative lifetime in a direct gap semiconductor. Thus the cross-section can be determined optically by measuring the decay rates of the FE and BE, assuming that the density of trapping centres is known.

The large size of the BE was found to have another important consequence. The BE oscillator strength in direct gap semiconductors was found to be surprisingly large compared to the intrinsic FE line, considering the relatively low density of impurity centres. A giant oscillator strength proportional to the volume of space covered by the BE wavefunction was proposed to be at the origin of this effect.[1.17] The shallowest BE have both the largest Bohr radius and the largest oscillator strengths and conversely the shortest lifetimes. This giant oscillator strength justifies the dominance of the BE lines in the photoluminescence (PL) spectrum of direct gap semiconductor at low temperatures even for very high-purity samples like GaAs having impurity concentrations of $\sim 10^{14}$ cm^{-3}. Besides the FE and BE photoluminescence lines observed in semiconductors, other non-excitonic recombinations are occasionally seen in the near band gap region. These transitions will be discussed in the following section.

1.3 Donor-Acceptor Pair Recombination

Donor-acceptor pair (DAP) complexes differ from exciton complexes bound to impurities, but they also retain many similarities. Like the neutral BE complex, the DAP complex consists of four point charges. It differs in that two of them are immobile, the donor ion D^+ and the acceptor ion A^- and the remaining two charges, the electron and the hole, are mobile.

When a donor and an acceptor impurity form a pair, the normal ionization energy E_D (or E_A) of an isolated donor (or acceptor) is reduced due to the Coulombic interaction between the electron and the hole bound to the impurities. The recombination energy of pair-band luminescence is given by the well-known and often quoted formula,[1.18]

$$\hbar\omega(R) = E_g - (E_A + E_D) + e^2/\epsilon R \quad (1.14)$$

This equation is easily understood from simple conservation of energy arguments. Consider a donor which has been compensated by an acceptor so that both are ionized and taking this state as the zero of energy. The energy required to form the complex is the energy E_g required to excite an electron to the conduction band leaving a hole in the valence band, reduced by the energy gained by binding the electron on D^+ in the presence of A^- at a distance R away, $-E_D + e^2/\epsilon R$, and then binding the hole on A^- in the presence of D^o, $-E_A$. In other words, the binding energy of the donor E_D is reduced by the repulsive potential $-e^2/\epsilon R$ arising from the ionized acceptor at a distance R, but the subsequent

process of placing a hole on the acceptor is not altered by the presence of the distant neutral donor and hence involves only the acceptor binding energy E_A. Small energy contributions due to the polarizabilities of the neutral donor and acceptor can also be included as a correction term J(R). This negative correction term (which increases the electron-hole binding energy and so reduces the influence of the dominant $e^2/\epsilon R$ term) is largest for transitions to acceptor and donor excited states, which have larger Bohr radii.

Since the donor and acceptor impurities can only be on well-defined lattice sites, R can assume only certain discrete values. For relatively small R corresponding to, say, 10 to 50 lattice spacings, the change in the energy $e^2/\epsilon R$ between lattice shells can be resolved and the spectrum $\hbar\omega(R) = E_g-(E_A+E_D)+e^2/\epsilon R$ appears as a discrete set of emission lines corresponding to the allowed values of R. As R increases, $e^2/\epsilon R \rightarrow 0$ and the emission lines from neighboring lattice shells become increasingly close together, eventually merging to form a broad band of emission energies with the low energy limit occurring for $\hbar\omega(\infty) = E_g-E_A-E_D$ as R approaches infinity. The intensities of the various lines of the spectrum are determined by the overlap of the donor and acceptor wavefunctions and the number of interacting pairs. Over 300 sharp lines corresponding to discrete DAP separations have been identified in GaP, along with the merging of the discrete lines to form the broad band emission as $R \rightarrow \infty$.[1.19]

However, the conditions required to observe both of these features of pair spectra are not met in all materials. For example, in GaAs the sum of the shallow donor and shallow acceptor binding energies is typically rather small. Emission energies of sharp isolated pair lines

would lie above the band gap energy because $e^2/\epsilon R > E_D+E_A$ for the correseponding values of R. Only the unresolved broad band portion of the pair spectra is expected to be observable. For example, in the low temperature (2K) GaAs photoluminescence spectrum, the emission band observed at 1490 meV was associated with DAP involving Carbon acceptors. At this energy, the mean separation R between the donors and acceptors is ~400Å. In fact, sharp line spectra attributable to the discrete values of R have not yet been identified in any direct gap III-V compound, probably because of the small impurity binding energies associated with the light electron and hole masses.

Further evidence for the donor-acceptor origin of the broad line at 1490 meV was obtained from studies of lifetimes and time-resolved spectroscopy.[1.20] It was found that the luminescence peaks associated with excitons had very rapid exponential decays with lifetimes of less than 5 ns. The 1490 meV line, however, had a longer nonexponential decay which is characteristic of DAP. The nonexponential power law form of the decay was discovered by Thomas and co-workers,[1.19] who also found much longer-lived decays with increasing wavelength of light within the distant pair band. This increase in decay times was associated with the increase of R of the pairs. The radiative lifetime $\tau(R)$ for isolated DAP was calculated by Thomas *et al.*[1.19] and for the case where $a_D > a_A$ (where a_D is the donor Bohr radius and a_A the acceptor Bohr radius), which applies for GaAs, $\tau(R)$ was given by

$$\tau(R) \propto \exp(2R/a_D) \ . \qquad (1.15)$$

Thus the decrease of the electron-hole wavefunction overlap would have

an effect of increasing the DAP lifetimes.

Finally, free-to-bound transitions, such as free-electron to neutral acceptor (e,A^o) or free-hole to neutral donor (h,D^o), are also observed in the near gap photoluminescence spectrum of various semiconductors. The energy of such photons would correspond simply to the difference between the band gap value and the energy of the neutral impurity. These lines are usually characterized by a Boltzmann tail to higher energy, reflecting the initial kinetic energy of the free particle. For example, the 1493 meV luminescence peak observed at T = 2K in GaAs has been attributed to such free-to-bound transitions involving a free electron and a Carbon acceptor.

1.4 Confined Excitons in 2-Dimensions

Quantum effects become increasingly significant as the size of the involved semiconductor material is reduced to a dimension as small as wavelengths of electrons. On the scale of interatomic spacing, quantum mechanics determines the band structure, the fundamental electronic and optical properties of semiconductors. On the other hand, semiconductor devices usually can be treated in a semi-classical manner, since the dimension involved in most cases is still greater than the mean free path of electrons. If, however, the dimension falls into a range from ten to a few hundred angstroms, macroscopic quantum effects are expected to influence the electronic structure of the material and thus alter the transport and optical properties.

Esaki and Tsu[1.21] were the first to propose a two-dimensional (2D) periodic structure, referred to as a semiconductor superlattice

(SL), with the spacing period being in such a quantum regime. With pairs of two semiconductors that closely match in lattice constant, it is possible to grow epitaxially one semiconductor on top of the other, where, at the interface, the potential energy for the electrons and the holes exhibits a sharp change. The recent advance of molecular beam epitaxy (MBE)[1.22] in ultrahigh vacuum provided atomically smooth surfaces and extremely sharp boundaries such that the growth of SL structures of high quality compound semiconductors could be produced in a controlled manner. The most prominent example of such a SL is the combination of GaAs and $Al_xGa_{1-x}As$. In $Al_xGa_{1-x}As$ some of the gallium atoms (~20-30%) have been replaced by aluminium atoms. The band gap increases with increasing aluminium concentration. Further, the very close matching between the GaAs and the $Al_xGa_{1-x}As$ lattice parameters means that dislocations are not produced at the crystal boundary, thus making it possible to grow crystals of high quality.

Let us examine the potential experienced by the carriers, the electrons in the conduction band and the holes in the valence band. In the 2D lattice plane perpendicular to the SL, the carriers encounter the usual periodic lattice. In the direction of crystal growth, however, that is in the direction perpendicular to the planes of the superlattice, they experience another artificially induced potential with a new periodicity, that of the superlattice. The difference in the band gap of the two materials is made up by an offset in the CB and an offset in the VB. The relative sizes of these offsets determine the potential seen by the electrons and holes respectively. In the case of the GaAs-$Al_xGa_{1-x}As$ superlattice shown in Figure 1.1, the offset in the VB is in the opposite direction to the offset in the CB. The

introduction of the SL potential clearly perturbs the band structure of the host materials. Since the SL period is much longer than the original lattice constant, the Brillouin zone is divided into a series of mini-zones, giving rise to narrow sub-bands separated by forbidden regions, analogous to the Kronig-Penney band model for the CB or the VB of the host crystal. The final band structure is therefore a property of the SL and not a property of the constituent elements GaAs or $Al_xGa_{1-x}As$. The minibands and the band gaps, caused by the periodic potential, are easily calculated using quantum mechanics by making the analogy with a particle confined to a two-dimensional rectangular potential well. The energy spacing and breadth of the minibands are changed by modifying the thickness of the two superlattice layers. From elementary quantum mechanics, if a particle is completely confined to a layer of thickness L_z (by an infinite potential well), then the energies of the bound states are

$$E = E_n + \left(\frac{\hbar^2}{2m^*}\right) \left(k_x^2 + k_y^2\right) \qquad (1.16)$$

where

$$E_n = \left(\frac{\hbar^2\pi^2}{2m^*}\right) \left(\frac{n}{L_z}\right)^2 , \quad n = 1,2,3\ldots \qquad (1.17)$$

In reality the potential is finite and the above solutions have to be modified.

Dingle *et al.*[(1.23)] were the first to report on the optical absorption spectrum of GaAs wells of different thickness sandwiched between two $Al_xGa_{1-x}As$ layers. Such structures are referred to as quantum wells (QW). They were able to resolve seven exciton

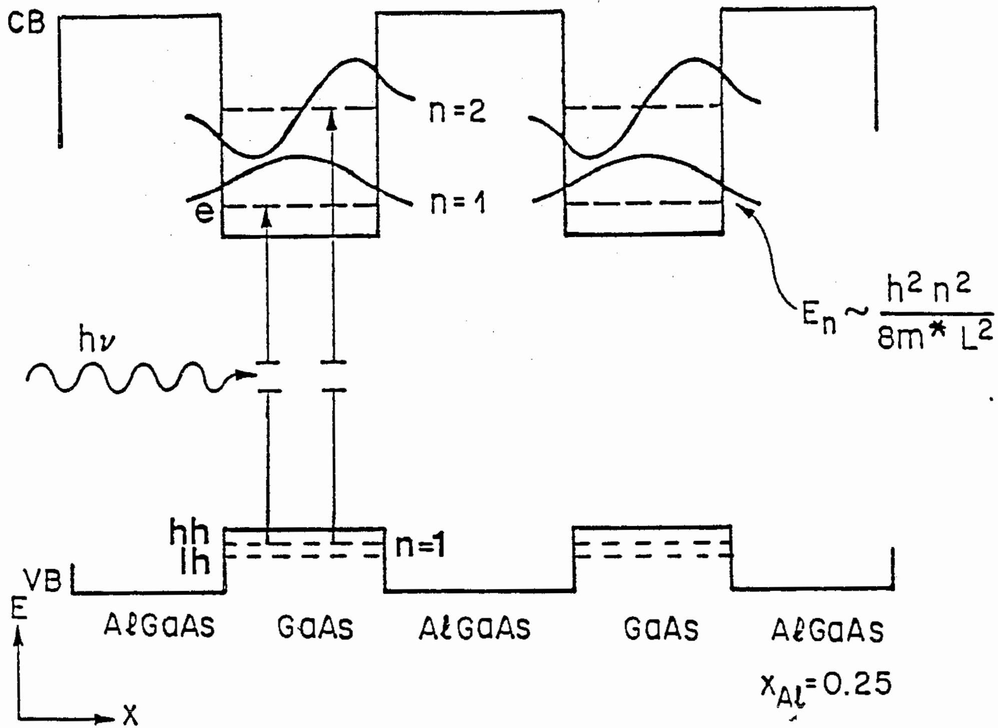

FIG. 1.1 Energy level diagram of a $GaAs/Al_{0.25}Ga_{0.75}As$ superlattice. CB and VB represent the conduction and valence bands of both semiconductors. Both n = 1 and n = 2 of the electron energy levels are represented, while only the n = 1 level of the heavy-hole (hh) and light-hole (lh) are shown.

transitions, associated with different bound electron and bound hole states. Their results showed that the QW behaved as a simple rectangular potential well with a depth of $\sim 0.70 \Delta E_g$ for confining electrons and $\sim 0.30 \Delta E_g$ for confining holes, where ΔE_g is the difference in the semiconductor energy gaps (i.e. $\Delta E_g = 1879 - 1519 = 360$ meV) for $x = 0.25$. Further, they also monitored the exciton binding energy for various well thicknesses ranging from 200 to 4000Å. For $L_z \simeq 200$Å, an exciton binding energy of ~7 meV was estimated, compared with a 4 meV binding energy for bulk GaAs. This increase from 4 to 7 meV in binding energy agrees quite well with that expected for a three-dimensional exciton as it approaches the two-dimensional limit.[1.24]

It was evident from the work by Dingle *et al.*[1.23] that excitons play a much more significant role in these quasi-2D systems than in bulk GaAs. The photoluminescence at low temperatures from a few microns of high-quality MBE-grown undoped GaAs is usually characterized by emissions due to excitons bound to donors and acceptors, as well as free-to-bound and DAP transitions. Small contributions due to free exciton emission are also observed. However, the main point is that for bulk GaAs grown by MBE, the emission at low excitation levels is usually predominantly extrinsic in nature. This is in marked contrast to GaAs QW with purity similar to the bulk GaAs material. Absorption, emission and excitation spectra of high-quality GaAs QW with good interfaces demonstrate that intrinsic free exciton recombination dominates the emission even at very low temperatures where bound exciton and impurity processes dominate for bulk GaAs.[1.25] This difference indicates that confinement of the wavefunctions in the QW plays a major role in the luminescence process. A first effect of confinement is to perturb the

impurity binding energy when the impurity-interface distance becomes of the order of the impurity Bohr radius (in bulk GaAs, $a_B \simeq 100Å$ for donors and ~30Å for acceptors). This leads to a smearing of the luminescence bands. A second effect comes from the symmetry of the impurity ground state wavefunction, which gradually changes from a 1S hydrogenic symmetry in bulk to a 2p symmetry at the interface. Depending on the exact position of impurities, the oscillator strength of the transition is therefore decreased compared to that of bulk materials.

The band structure of bulk GaAs[1.26] shows that the top of the valence band, at k = 0 (Γ-point), is 4-fold degenerate. Away from the Γ-point, the degeneracy is lifted and there are two 2-fold degenerate bands;. the upper termed the heavy-hole (having an effective mass $m^*_{hh} = 0.45\ m_o$) and the lower called the light-hole (effective mass $m^*_{lh} = 0.088\ m_o$).[1.26] Making use of these results for bulk GaAs and applying it to the 2-dimensional limit of QW, one would expect, according to equations (1.16) and (1.17), two series of hole energy levels; one associated with the heavy-hole and the other with the light-hole. The conduction band, however, is nondegenerate at the Γ-point and only one series of electron levels is expected. This splitting of the heavy and light hole bands in GaAs QW has led to the well-resolved heavy- and light-hole exciton transitions in absorption[1.27] and emission.[1.28] Furthermore, a number of GaAs QW samples have shown explicit structure in the excitation spectrum which were identified with excited states of the 2D excitons such as the n = 2 heavy-hole recombining with the n = 2 electron. It was shown by Dingle *et al.*[1.23,1.25] that only transitions involving electrons and holes

having the same quantum number n, where $n = 1,2,3...$, are allowed. Transitions where $\Delta n \neq 0$ were found to be forbidden and not observed in absorption or emission. The only exception to this rule is the parity allowed $\Delta n = 2$ transitions, such as the recombination of a $n = 1$ electron and $n = 3$ heavy-hole, which are sometimes very weakly observed.

From the point of view of material science, synthesized SL may be regarded as a novel class of quasi-2-dimensional materials. The important electronic properties, such as the energy gaps, can be made to order since they are determined by introduced SL potential together with the band structure of the host materials. These SL appear to offer a new degree of freedom in semiconductor research through advanced material engineering and have inspired many ingenious experiments, resulting in observations of not only predicted effects, but also totally unknown phenomena.

CHAPTER 2

EXPERIMENTAL METHODS

2.1 Introduction

The impact of lasers on spectroscopy can hardly be overestimated. Lasers represent intense light sources with energy densities which may exceed those of incoherent sources by many orders of magnitude. Furthermore, because of their extremely small bandwidth, single-mode lasers allow a spectral resolution which far exceeds that of conventional spectrometers. Many experiments which could not be done before because of lack of intensity or insufficient resolution, are readily performed with lasers. Of particular interest are the continuously tunable dye lasers which may in many cases replace wavelength-selecting elements, such as spectrometers or interferometers.

One major trend in the laser field was concerned with the development of techniques for obtaining very short laser pulses. The generation of laser pulses of about 10^{-8} sec duration by means of laser Q-switching was a first significant step towards shorter pulses.[2.1] With the introduction of laser mode-locking, pulses much shorter than a nanosecond became available.[2.2] As a result, the methods of picosecond laser pulse generation and measurement are now sufficiently refined and catalogued for them to be used with confidence for the investigation of the interaction of coherent light with matter. Furthermore, an important aspect of the progress in generation of

ultrashort pulses is the increase in peak power made possible by these developments.

This chapter is concerned with the techniques and instrumentation used in the production, observation, and measurement of photoluminescence. The chapter begins with a basic discussion of the main elements of experimental optical spectroscopy, namely, excitation sources, spectrometers, detectors, and signal recovery techniques, with particular emphasis on the advantages and limitations of the instrumentation described. Techniques used in the measurement of luminescence decay times and in the measurement of time-resolved spectra are then discussed in the last section.

2.2 Lasers as Spectroscopic Light Sources

2.2-1 *Excitation Sources*

Since there are many excellent texts on lasers,[2.3,2.4,2.5] only a short summary of lasers and laser techniques used for the excitation of luminescence will be discussed.

As previously mentioned, lasers offer the prospect of an excitation source of exceedingly high intensity compared with classical light sources. This may significantly reduce noise problems caused by detectors or background radiation. Some lasers are pulsed giving very large intensities for very short times; others can be continuously operated (continuous wave, CW). Some are of fixed frequency; others are, to some extent, tunable. Often the active medium exhibits gain on several transitions and the laser can oscillate simultaneously on many lines. As long as the different gain regions are narrow and do not

overlap, the wavelength of each line is still restricted to its narrow gain range, and the laser is a multi-line fixed wavelength laser. For example, gas lasers, many of which can be continuously excited by an electrical discharge, provide such a fixed frequency CW emission at a variety of wavelengths. In the present study, an Argon ion laser (Spectra Physics Model 171) was used as the above band gap excitation source or used as a pump for a dye laser. The discharge of a CW Argon laser exhibits gain for more than fifteen different transitions. (The two strongest emission lines are at 488 nm and 514.5 nm.) In order to achieve single-line oscillation in laser media which exhibit gain for several transitions, wavelength-selecting elements outside or inside the laser resonator can be used. If the different lines are closely spaced, which is the case for the Ar^+ laser, prisms, gratings, or Lyot filters are commonly used for wavelength selection.

On the other hand, there are several cases where the gain profile extends over a broad spectral range. The most important example of this type is the dye laser,[2.6,2.7] where stimulated emission from the excited state to many vibronic levels of the electronic ground state is possible. Because of the strong interaction of the dye molecules with the solvent, these levels are broadened so that the linewidth exceeds the level separation. The absorption and fluorescence of the dye molecules in liquid solvents therefore exhibits a broad continuous spectral distribution, and the gain profile extends over a large spectral range of several tens of nanometers. With different dyes, the overall spectral range, where CW or pulsed laser operation has been achieved, extends from 300 nm to 1.2 μm. The possibility of continuously tuning the wavelength of such narrow-band lasers has

certainly opened a new area of spectroscopy. A tunable laser represents a device which is a combination of an intense light source and an ultrahigh resolution spectrometer. In a simple cavity, the possible laser wavelengths λ_L are determined by the optical length nd between the resonator mirrors.[2.4]

$$q\lambda_L = 2nd \quad , \quad q = 1,2,3... \tag{2.1}$$

Most lasers, however, need additional wavelength-selecting elements inside the laser resonator since the gain bandwidth is usually vastly larger than the intermode spacing. By introducing such a tuning element inside the laser resonator, laser oscillation is restricted to a narrow spectral interval and the laser wavelength may be continuously tuned across the gain profile by varying the transmission maxima of these elements. In the Spectra Physics 375 dye laser, tuning is accomplished by an element known as a tuning wedge (Fig. 2.1-a). It consists of a mirror coating on a substrate on top of which is added another coating which varies in thickness from one side to the other. A mirror coating is then deposited on top of the wedge coating. The tuning wedge is thus a Fabry-Perot etalon with a large free spectral range (FSR = 100,000 GHz; 110 nm). As the wedge is moved laterally across the optical path, the effective mirror spacing changes, shifting the peak transmission frequencies of the tuning wedge. The effect of introducing a second fine-tuning etalon (FSR = 900 GHz; 0.11 mm) in the cavity is to limit the linewidth of the dye laser output beam by further enhancing mode competition.[2.4] When used with the tuning wedge, the fine-tuning etalon reduces the linewidth by about a factor of 5 (FWHM from 0.2 nm

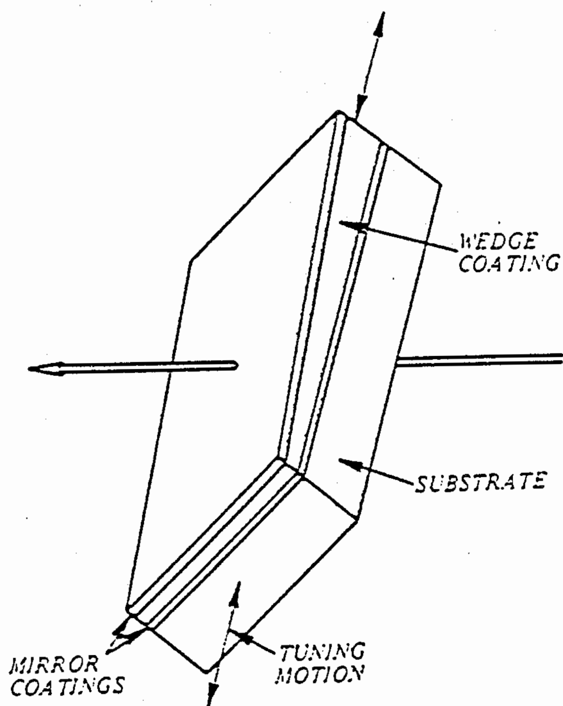

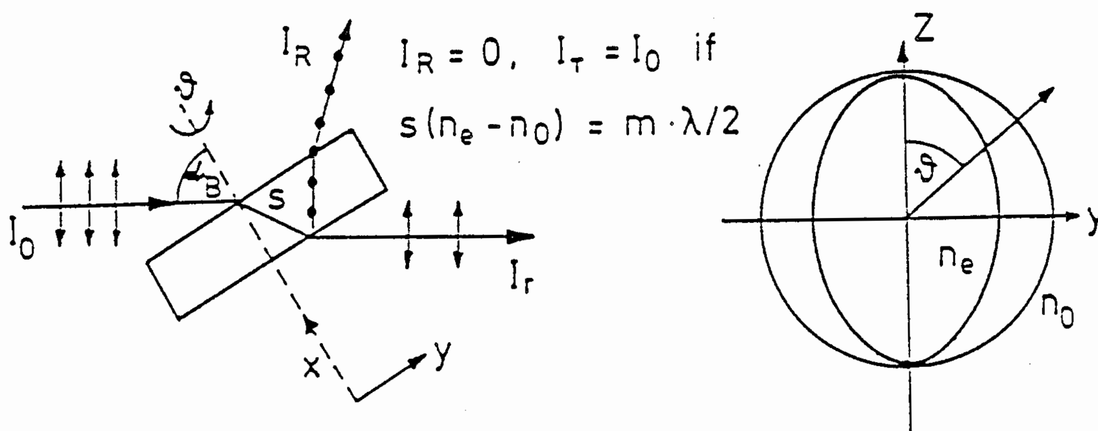

FIG. 2.1 (a) Commercial tuning wedge. (b) Tilted birefringent plate used as a tuning element within a laser resonator and the corresponding index ellipsoid.

down to 0.05 nm). The transmission peak of the etalon (and thus the output wavelength of the dye laser) can be varied continuously by rotating the axis of the etalon in a vertical plane, effectively changing the optical length of the etalon cavity. Most of the nonresonant excitation experiments performed in this work were done using this commercial system.

Unfortunately for some of the very high-resolution experiments, such as photoluminescence excitation spectra (PLE) and resonant excitation done under magnetic field, the laser linewidth obtained using the two etalon combination was found to be too wide. To further improve the spectral width of the laser output, tilted birefringent plates were used as tuning elements.[2.8] A birefringent crystal has two refractive indices. The difference between these two indices, Δn, is the birefringence. If a birefringent crystal is placed between two perfectly parallel polarizers, such that the light is equally split between the two indices, then the transmitted light as a function of wavelength has the form:[2.9]

$$\cos^2\left(\frac{\pi\ \Delta n\ S}{\lambda}\right) \tag{2.2}$$

where S is the length of the crystal and λ is the wavelength. However, if the tilting angle is chosen to be equal to the Brewster angle, the plates act both as retarding and polarizing elements and no polarizers are necessary. When the incoming beam enters the birefringent plate whose optic axis is out of the plane defined by the polarization of the Brewster surfaces, it will split into an ordinary and an extraordinary wave. While the ordinary refractive index n_o in a uniaxial crystal is

the same for all directions θ against the optical axis, the extraordinary beam has a refractive index n_e depending on θ. This is illustrated in Figure 2.1-b, which gives both refractive indices for a given wavelength as a function of θ. The difference $\Delta n = n_o - n_e$ therefore depends on θ. Turning the crystal around the dashed x-axis, which is perpendicular to the YZ plane, results in a continuous change of Δn and since the laser tries to run in the lowest loss condition, it changes the wavelength so that equation (2.2) continues to yield 100% transmission. A single crystal plate would tune the laser but the output linewidth would be wide. A narrower linewidth is obtained by adding additional plates. From equation (2.2), one notes that a crystal exactly twice as long would have twice as many transmission zones. Our birefringent filter was made out of four flat and parallel crystalline quartz plates having a total length of ~14 mm. This tuning element proved to be adequate for the high resolution work generating a laser linewidth better than 0.02 nm at FWHM.

2.2-2 *Mode Locking*

The generation of extremely short and intense laser pulses has opened the way for the study of fast transient phenomena, such as the interaction of light with solids which typically proceed on a picosecond time scale. The technique of mode-locking[2.10-2.13] the axial modes of a laser provides the means of reliably generating picosecond pulses for use in time-resolved spectroscopy. Mode-locking refers to the situation where the cavity modes are made to oscillate with comparable amplitudes and with locked phases. The production of such short optical pulses requires a laser system with an active medium that provides a large

frequency bandwidth for light amplification. To obtain light pulses of duration t_p, a gain bandwidth of at least $\Delta\nu_{gain} = 1/t_p$ is needed. For a discussion of the basic idea of laser mode-locking, let us consider a laser resonator formed by two mirrors and an active material for light amplification. This simple laser has a well-known set of resonant modes with characteristic resonant frequencies.[2.14] Restricting ourselves to the discussion of axial modes only, we are then left with a set of equally spaced resonant frequencies (Fig. 2.2-a). The frequency spacing $\delta\nu$ of the modes is given by

$$\delta\nu = c/2L \tag{2.3}$$

where c is the speed of light and L is the optical path between the two mirrors forming the resonator. In an inhomogeneously broadened laser, many of these axial modes will generally be above threshold and lase simultaneously.[2.15] In the model 171 Ar^+ laser, L ≃ 1.8 m and $\delta\nu \simeq 82$ MHz, and the Doppler- broadened Argon gain profiles have bandwidths of ~5 GHz. The total laser output field resulting from the superposition of the modes having a frequency bandwidth $\Delta\nu$ centered at ν_o can be written for a particular point in the laser resonator as:

$$E(t) = \sum_{\ell=-n}^{n} E_\ell \exp[i(\omega_\ell t + \phi_\ell)] \tag{2.4}$$

where E_ℓ, ϕ_ℓ and $\omega_\ell = 2\pi(\nu_o+\ell\delta\nu)$ are the amplitudes, phases and resonant frequencies of the cavity modes. Furthermore, the total number of modes can be expressed as $2n+1 = \frac{\Delta\nu}{\delta\nu} + 1$. Assuming that the amplitudes of the modes are all equal, $E_\ell = E_o$, and substituting for ω_ℓ, equation (2.4)

(a)

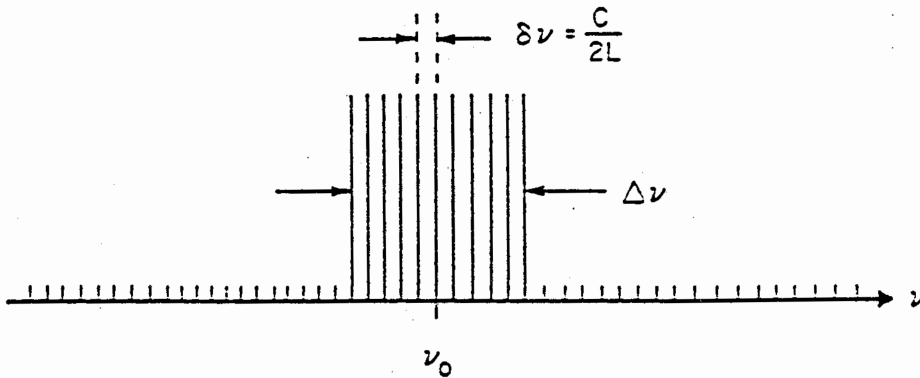

(b)

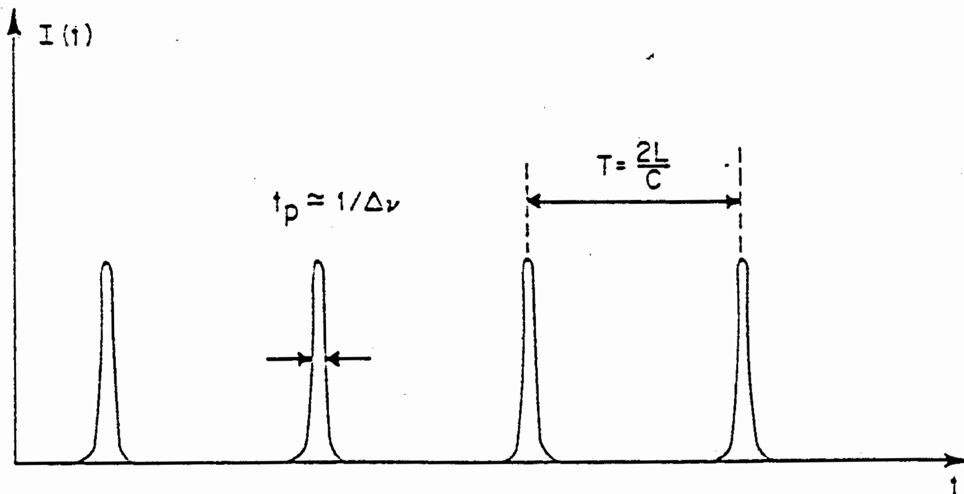

FIG. 2.2 (a) Spectrum of the cavity modes of a laser having a total length L. The frequency spacing of the modes is $\delta\nu$ and the frequency bandwidth is $\Delta\nu$. (b) Multimode laser output for constant phases. The output consists of a regular sequence of pulses. The spacing in time between pulses is T and the pulse duration is t_p.

can be rewritten as

$$E(t) = E_o \exp(i\omega_o t) \sum_{\ell=-n}^{n} \exp[i(\ell\delta\omega t + \phi_\ell)] \, . \tag{2.5}$$

Under normal circumstances, the phases of the modes change randomly, but if the phases can be locked such that[2.10]

$$\phi_\ell - \phi_{\ell-1} = \phi \tag{2.6}$$

where ϕ is a constant and the sum over ϕ_ℓ becomes simply $\ell\phi$. Using this assumption, equation (2.5) can be easily evaluated as

$$E(t) = A(t) \exp(i\omega_o t) \tag{2.7}$$

where

$$A(t) = \frac{E_o \sin[(2n+1)(\delta\omega t+\phi)/2]}{\sin[(\delta\omega t+\phi)/2]} \, . \tag{2.8}$$

The power output, which is proportional to the square of the electric field amplitude, $(A(t))^2$, is shown in Fig. 2.2-b. By choosing the time origin in such a way as to eliminate the constant phase factor ϕ, equation (2.8) can lead to the following properties for the output pulse train:

i) The spacing in time of the pulses is

$$T = 1/\delta\nu = 2L/c \, . \tag{2.9}$$

ii) The peak intensity is the total number of participating modes, (2n+1), times the average intensity[2.16]

$$I_{peak} = (2n+1) \langle I \rangle . \qquad (2.10)$$

iii) The pulse duration t_p is given by

$$t_p = \frac{1}{(2n+1)\delta\nu} = \frac{1}{\Delta\nu} . \qquad (2.11)$$

The situation where the cavity modes of a laser are made to oscillate with locked phases is referred to as mode-locking. The pulse width of a perfectly mode-locked laser is given by the inverse width of the oscillating frequency spectrum, and the peak intensity exceeds the average intensity by a factor of $T/t_p = \Delta\nu/\delta\nu$. For example, mode-locking of the Argon ion laser gives pulses of about 1/5 GHz = 200 ps. With an average power of 1 Watt and a repetition rate of 82 MHz, the peak power is of the order of 60 W for such a laser. In the following, a discussion on the techniques used for locking together the resonator modes will be given.

The most commonly used mode-locking methods belong to one of the following two categories: *1*) mode-locking by means of a suitable nonlinear optical material such as a saturable absorber (passive mode-locking) and, *2*) mode-locking by an active modulator driven by an external signal (active mode-locking). Active mode-locking can be achieved by inserting into a laser resonator a device for periodic modulation of either the loss of or the refractive index of the cavity. There exists a variety of acousto-optic modulation techniques.[2.17]

For the understanding of active mode-locking, let us consider the modulation of a monochromatic light wave, $E_o(t) = \frac{1}{2} A_o \exp(-i\omega_o t) + c.c.$, by a sinusoidally driven *loss modulator*. The time variation of the transmission of the modulator can be expressed as

$$T(t) = 1-\delta_m[1-\cos(\Omega t + \phi)] \tag{2.12}$$

where δ_m is the modulation amplitude, Ω and ϕ are the modulation frequency and phase, respectively. The modulated wave, $E_1(t) = T(t)E_o(t)$ can be written as

$$E_1(t) = \frac{1}{2} A_o \left[\left(1-\delta_m\right) e^{-i\omega_o t} + \frac{\delta_m}{2} \left(e^{-i[(\omega_o-\Omega)t-\phi]} + e^{-i[(\omega_o+\Omega)t+\phi]} \right) \right] + c.c. \tag{2.13}$$

The modulator generates two new frequency components, $\omega_o+\Omega$ and $\omega_o-\Omega$. The phases of the sidebands are related to the phase of the modulator, i.e. $-\phi$ for $\omega_o-\Omega$, and $+\phi$ for $\omega_o+\Omega$. Consider now repeated modulation by an array of identical modulators, and let us assume that the time dependence of the transmission of all these modulators is given by equation (2.12). One requires that the spacing Δz of two subsequent modulators satisfies the relation

$$\Delta z = \frac{2\pi c}{\Omega} m , \quad m = 1,2,3... \tag{2.14}$$

This condition ensures that the light wave stays in phase with the modulation when travelling from one modulator to the other. Each

modulator adds a new pair of sidebands with the proper phase. Thus the light wave, after having travelled through N modulators, can be represented by

$$E_N(t) = \sum_{n=-N}^{N} a_n e^{-i[(\omega_o+n\Omega)t+n\phi]} + c.c. \qquad (2.15)$$

The final field consists of (2N+1) equally spaced frequency components, all oscillating in phase. In other words, the output field is mode-locked and one ends up with an output intensity in the form of train of pulses similar to the pulse train shown in Fig. 2.2-a. In an actual laser the light travels back and forth between the cavity mirrors and interacts with the same modulator many times. The light stays in phase with the modulation, if the modulation frequency is an integral multiple of the inverse round-trip time

$$\frac{\Omega}{2\pi} = m\delta\nu = m\frac{c}{2L}\ ; \quad m = 1,2,3... \qquad (2.16)$$

The final number of oscillating modes, which is equal to the number of sidebands, is determined by the spectral range over which sufficient laser gain is available. For the Argon ion laser used in this work, mode-locking was achieved with an acousto-optic modulator driven at half of the cavity mode spacing frequency. This establishes an acoustic standing wave in the crystal which can be temperature tuned to exactly half of the mode spacing frequency.[2.18] A method of locking the crystal resonance to the drive frequency by actively varying the RF power supplied to the crystal was presented elsewhere.[2.19] Whenever the acoustic wave amplitude goes through zero, the transmission through

the cell is at a maximum; at other times, some of the light is diffracted out of the cavity by the acoustically induced change of the refractive index, thus producing some loss. Due to the narrow bandwidth of the Ar^+ laser, the pulse width is limited to about 200 ps. By using the mode-locked Ar laser to synchronously pump a dye laser, even shorter (and wavelength tunable) pulses can be created. This will be the topic discussed in the next section.

2.2-3 *Synchronous Pumping and Cavity Dumping of Dye Lasers*

Dye lasers are very suitable for the generation of ultrashort light pulses because organic dyes provide efficient laser gain over a wide frequency range. This large bandwidth allows significant frequency tuning even for relatively wide band ultrashort pulses.

A very convenient method for mode-locking of dye lasers is direct modulation of the laser gain.[2.20] In this scheme the output of another mode-locked laser serves to pump the active dye solution which is placed in a separate optical resonator. The pump pulses produce a rapidly varying gain in the dye laser, because the gain is substantial only for a very short time after the absorption of a picosecond pump pulse. To obtain mode-locking, the round-trip time in the dye laser cavity has to match the repetition time of the pump pulse train. This is done by setting the cavity length of the dye laser equal to, or a submultiple (multiple) of, that of the pumping laser.[2.21] Frequency tuning of the dye laser output can be achieved by introducing frequency selective elements such as the one mentioned in section 2.2-1. For example, using the tuning wedge as the frequency selective element, a spectral width of 0.2 nm can be achieved, which corresponds to ~90 GHz

resulting in a transform limited pulse width of ~10 ps.[2.21] A typical synchronously pumped dye laser system is thus capable of delivering a continuous train of tunable, mode-locked pulses, of spectral linewidth ~0.2 nm, time duration ~10 ps at a repetition rate of 82 MHz. These short and narrow linewidth pulses of light can be used successfully in the study of the dynamics of excitons in semiconductors.

The mode-locked Argon laser used here has an intrinsic repetition rate of 82 MHz corresponding to a period of ~12 ns between pulses. Consider the case of a *luminescent system* having a lifetime in the nanosecond range. This repetition rate would be too fast for a complete relaxation of the system, since the next laser pulse would arrive before the total decay of the system. A method of lowering the repetition rate is thus essential. A convenient way to produce mode-locked pulses with variable repetition frequency uses a cavity dumping system. Inside a folded laser resonator with highly reflecting mirrors, a quartz cube is inserted within which ultrasonic pulses with controllable repetition rate generate a periodic modulation of the refractive index. During the ultrasonic pulse, a phase grating is produced in the quartz cube which causes Bragg diffraction[2.22] of the laser wave. Choosing the optimum ultrasonic wave amplitude, nearly all of the intracavity laser intensity is diffracted into the first order and coupled out of the resonator. By this method, pulses can be ejected from the laser cavity at a rate corresponding to an arbitrary submultiple of the intrinsic, mode-locked repetition rate. Furthermore, the cavity dumper allows larger output peak powers because it releases nearly all of the intracavity power P_i, while in other systems only the fraction TP_i is transmitted through the output mirror with transmission T. The commercial Spectra-Physics

(Model 344S) cavity dumper used in the present work had a trailing pulse rejection of 500:1 and a variable repetition rate from a single shot up to 4 MHz.

2.3 Spectroscopic Instrumentation

This section is devoted to a brief discussion of instruments which are of fundamental importance for measurements of wavelengths and line profiles or for sensitive detection of radiation. The optimum selection of proper equipment or the application of a new technique is often decisive for the success of an experimental investigation. At first the various spectrometers used in the dispersion of the luminescent signal are discussed. Additionally, great progress has also been achieved in the field of low-level signal detection. Apart from new photomultipliers (PM) with an extended spectral sensitivity range and large quantum efficiencies, new detection instruments have been developed such as the imaging PM tubes. The second part of this section will deal with the detectors and signal recovery used in the present work.

2.3-1 *Spectrometers*

For most of the nonresonant photoluminescence experiments performed, where a standard PM-tube was used as detector, a double 0.75 m Czerny-Turner spectrometer was employed as the dispersive element. The 600 grooves/mm gratings (blazed at 1.0 μm) yield a reciprocal linear dispersion of 1.1 nm/mm when operated in first order. Thus, using 50 μm slits width, a spectral resolution of 0.06 nm (0.1 meV

at 820 nm) could be achieved. This system was particularly useful when extremely low stray light levels were necessary. However, for very weak PL signals, where the imaging PM-tube (section 2.3-2) was required, a single stage 0.75 m spectrometer with 1200 grooves/mm grating, blazed at 750 nm, was used. Finally, when very high dispersion was needed, such as in the Zeeman experiment, a 5 m single stage spectrometer (having f/50) was built. A reciprocal linear dispersion of 0.17 nm/mm was obtained from a 1200 grooves/mm grating.

2.3-2 *Detectors and Signal Recovery*

In most circumstances the detector is the key factor in luminescence measurements. Depending on the measurement, the detector's wavelength or time response or its signal-to-noise ratio will be the limiting factor. Though there are a number of different types of photodetectors, the photomultiplier is almost universally used in luminescence work because of its outstanding performance in most respects. For example, the higher gain and quantum efficiency of PM-tubes are important factors when weak signals are encountered, also allowing for the detection of individual photons. This means that the output signal can be measured in two ways: either counting the individual pulses or integrating them into an average current. The latter is considerably simpler and in many cases quite satisfactory, but pulse counting has an advantage if the data are to be digitally processed since it is directly available in digital form. One other important aspect of detectors is their time response when measuring lifetimes, time-dependent spectra or when using pulse counting. Photomuliplier tubes are very well suited for fast transient work as the

limiting factor is the width of the output pulse originating from a single photoelectron leaving the photocathode.[2.23] In this study, two PM-tubes (VPM-159A3 and ITT-F4128F) were used concurrently as detectors. The choice of one PM over the other was determined by two criteria; *1*) the spectral location of the photons to be detected and, *2*) the transient behaviour of the recombination process to be studied. Table 2.1 summarizes some important characteristics of each detector.

In recent years a variety of optical multichannel detectors have been considerably improved for their application to the field of optical spectroscopy. The parallel collection advantage inherent to these devices can be used to greatly decrease data acquisition times or can be applied to the detection of extremely weak optical signals. Of these multichannel detectors, only the microchannel-plate (MCP) electron multipliers with resistive anode (RA) can be considered true photon counting imaging detectors in that every photon-generated charge pulse is individually sensed.[2.24] The MCP-RA detector derives its extreme sensitivity not only from its multichannel detection advantage but also from a very low dark count (1 count/hr/channel). This imaging photomultiplier tube was used extensively for the detection of weak PL signals. Its characteristics are reported in Table 2.1.

The outstanding performance of photomultipliers makes it possible for single photons to produce output pulses large enough to be counted individually. This approach has been found to provide a means of improving the signal-to-noise ratio by about an order of magnitude relative to other detection techniques such as lock-in amplification. The next section will look in more detail at the most important application of single photon counting technique.

TABLE 2.1 Detector Response

	Quantum Efficiency At 800 nm	Wavelengh* Range (nm)	Rise-Time** 10-90% of Max (ps)	FWHM** (ps)	Exponential** Fit of Decay Time (ps)
Varian PM Tube VPM-159A3	2%	400-1220	~730	500	240
ITT-PM Tube F4128F	1.5%	400-875	~430	200	70
ITT-Imaging MCP-RA F4146M (Mepsicron)	1.5%	400-875	~480	500	190

*Wavelength range for which the quantum efficiency (QE) is larger than 1% of maximum QE.

**Instrumental response of the detector to a ~10 ps wide laser pulse generated by a synchronously pumped, cavity-dumped, mode-locked dye laser. The laser was set to 800 nm.

2.4 Time-Resolved Spectroscopy

2.4-1 *Delayed Coincidence Technique*

The advantage of photon counting over other methods arises from the form of the pulse-height distribution of the output pulses and the digital measurement. Noise pulses arising from electrons not originating from the photocathode will probably be smaller than those that do, while pulses due to high energy sources will probably be larger. Thus by using a discriminator at the output, a large number of these noise pulses can be eliminated from the count. The mid-range pulses that are accepted will still be subject to variation in height owing to statistical variations in gain, but provided the variation does not go outside the discrimination levels, they are counted as one count irrespective of height. Although photon counting is particularly advantageous at low light levels, it can also be used at higher intensities. However, for good linearity there is an upper limit of about 10^6 Hz set by the resolving time of discriminators and counters since the random arrival time of the photons must be allowed for. If two pulses arrive too close together, the counter will see them as one so counts will be lost.[2.25-2.26] Thus the luminescence count rate must be kept low enough that the probability of detecting two photons per laser pulse is very low.

The most popular technique using a pulsed source for lifetime determinations in luminescence has taken its origin from nuclear physics research which has led to the development of fast detectors, discriminators, and time-to-amplitude converters. Single photon counting techniques were used to measure the time distribution of the

probability that a fluorescence photon is emitted within a certain time interval after the excitation pulse. A general layout of the single photon counting experiment used here is shown in Fig. 2.3. The method depends on the use of very fast pulse discriminators,[2.27] together with a time-to-amplitude converter (TAC)[2.28] which delivers an output pulse to the pulse-height analyzer (PHA), the amplitude of the pulse being accurately proportional to the time difference between the start and stop pulses at the TAC. The pulse-height analyzer is then connected to an IBM-PC. The computer thus receives a number corresponding to the time difference between the start and stop pulses for each pair of pulses. After the collection of many such pairs, a histogram of the luminescence decay is obtained. The start pulse is generated by the detection of a photon (luminescence from the sample) by the photomultiplier tube which then triggers the constant fraction discriminator (CFD). The stop pulses are obtained from a second discriminator which is triggered by a fast Si-avalanche photodiode which samples a small portion of the exciting laser beam. The overall time resolution of the above system was limited by the response time of the various PM used and are shown in Table 2.1.

Time-resolved spectra could also be collected using a combination of the above techniques.[2.29] The output of the fast PM was fed into the TAC and then to the PHA as before, but upon completion of the collection period at a given wavelength the microcomputer would sum the counts in all the channels corresponding to eight separate time windows after the excitation pulse and store the eight sums separately. The computer would then increment the spectrometer location, set all channels to zero and collect the next data points. In this way eight

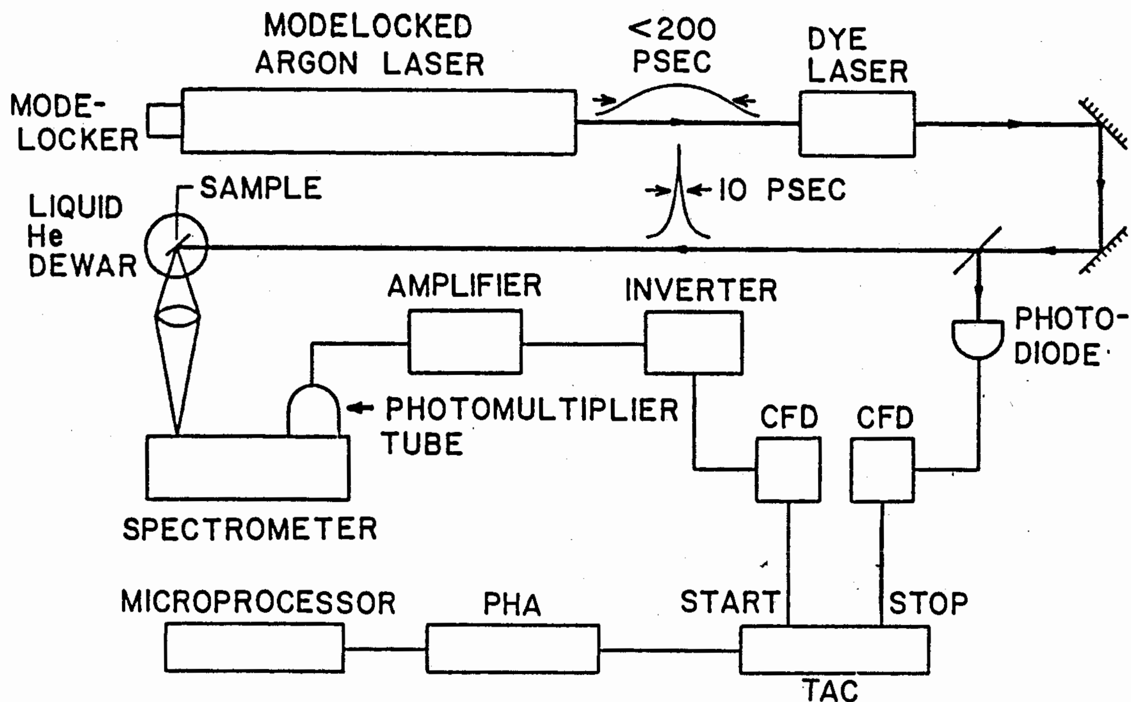

FIG. 2.3 Schematic diagram of the experimental setup for performing time-resolved photoluminescence measurements using a delayed coincidence photon counting system. PHA: Pulse-height analyzer, TAC: Time-to-amplitude converter, CFD: Constant Fraction Discriminator.

spectra corresponding to various time windows could be collected simultaneously.

2.4-2 *Timing Information from Imaging PM Tubes*

As discussed in section 2.3-2, in addition to its sensitivity, the MCP-RA detector, due to both its photon counting nature and physical construction, should, in principle, be capable of providing very accurate timing information when used in conjunction with standard time-correlated single photon counting techniques. We reported previously[2.24] that with a simple addition to the standard biasing network of a commercial MCP-RA detector, timing signals could be generated which were comparable to those available from conventional fast single channel PM tubes. By combining this with standard delayed coincidence time correlation circuitry, a very versatile data-acquisition system was developed allowing us to utilize the powerful parallel collection capabilities of the imaging tube while simultaneously resolving the spectral information into two adjustable time windows.[2.30]

The experimental system is shown schematically in Fig. 2.4. The timing signal is obtained from the 0.008 μF capacitor and 48 Ω resistor connected between the plate output biasing lead and ground. A transient positive voltage pulse is developed across the resistor as the photon-initiated electron shower emerges from the MCP. This pulse is amplified by two Comlinear CLC100 amplifiers, inverted and fed to a CFD which generates the start pulse for the TAC. The TAC stop pulse is provided by the same avalanche photodiode which samples a small fraction

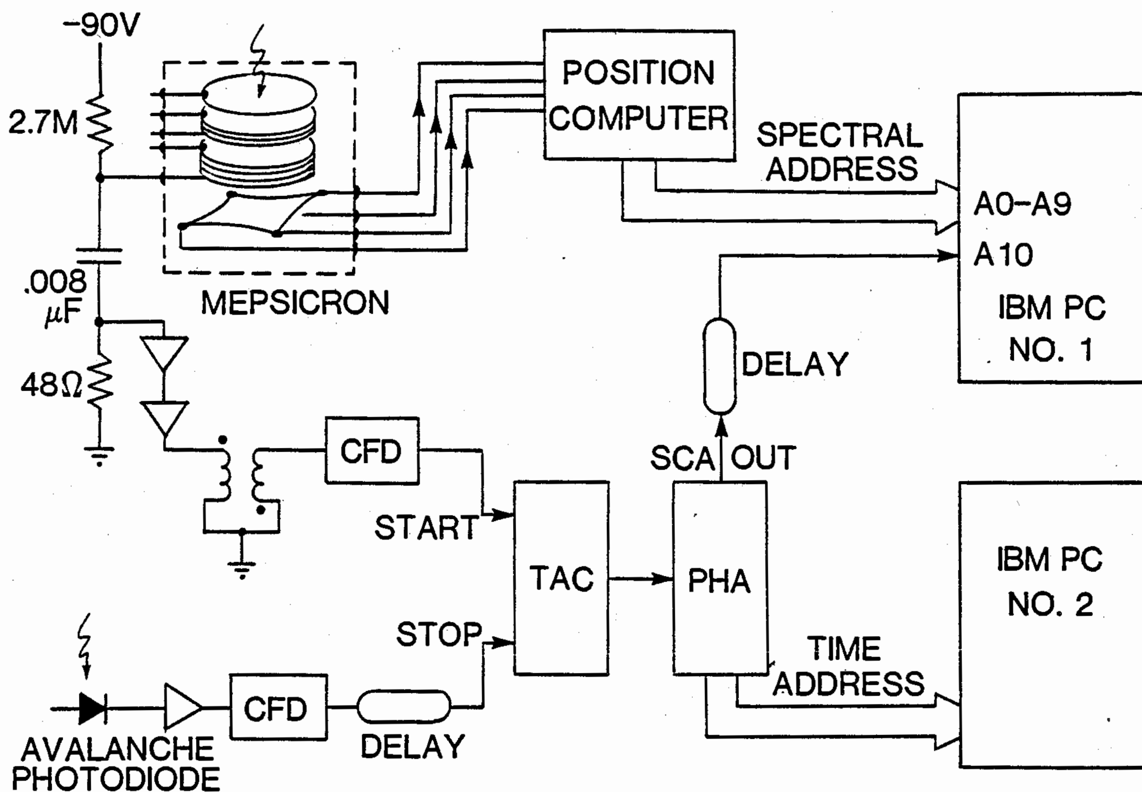

FIG. 2.4 Experimental system depicting the imaging detector and its associated electronics together with the time correlation circuitry.

of each laser pulse used for sample excitation. The TAC output is digitized by a PHA, and these data are passed as a temporal address to a histogramming board within a second IBM-PC used for conventional single channel time-resolved spectroscopy. By combining the single channel analyzer (SCA) output of the PHA with the spectral address of the position computer (No. 1), spectral data were collected in parallel while simultaneously resolving it into two time windows. The SCA output constitutes the time information (A10) of the address word while the lower 10 bits (A0-A9) comprise the spectral information. Two separate blocks of 1024 spectral channels were simultaneously acquired in the memory of the first IBM-PC; the spectral data were automatically routed to the appropriate block depending on whether or not the data correspond to an event within the PHA time window. The instrumental response of this system is recorded in Table 2.1. Thus, without loss of temporal resolution, the sensitivity of the MCP-RA detector can be used to extend time-resolved spectroscopy to the study of very low light level systems. This new technique played a major role in the investigation of the defect-induced bound exciton lines in MBE-grown GaAs, which is the subject of the next chapter.

CHAPTER 3

DEFECT-INDUCED BOUND EXCITONS IN MBE GaAs

3.1 Introduction

Epitaxial layers of GaAs are of considerable technical and commercial interest for many new applications. These thin single crystal layers must have well-controlled electrical transport and carrier recombination properties, usually derived from the addition of particular dopants. It is important that the distribution of these donor and acceptor impurities and the compensating acceptors and donors present be well characterized. It is usually impossible to identify the compensating species from electrical measurements. It is thus natural to turn to optical techniques to complement information provided by traditional electrical analysis. It happens that the optical techniques, particularly photoluminescence, are suited to the simultaneous recognition of electrically active shallow donors and acceptors in a single specimen. PL data have been presented for many years as a means of identification and classification of impurities in semiconductors, particularly those which give spectral emissions within a few hundred meV below the band gap. This has included simple acceptor and donor impurities and also a variety of bound exciton effects. In GaAs the small differences of energy levels for many different donor impurities prevents the use of free-hole to bound electron (D^o,h) emission or bound exciton emission (D^o,X) for differentiating between such impurities. For acceptors, the situation is quite different, since

substitutional species have chemical shifts ranging from a few meV to several tenths of an eV. Such shifts give rise to distinguishable features in both the free-electron to bound hole (e,A^{o}) and bound exciton spectra (A^{o},X). Table 3.1 summarizes the binding energies of a number of donors and acceptors in GaAs.

TABLE 3.1 Shallow donor and acceptor binding energies in GaAs (T=4.2 K)[3.2]

Donors	Binding Energies* (meV)	Acceptors	Binding Energies** (meV)
Theory (donor effective mass calculation)	5.715	Theory (acceptor effective mass calculation)	27.0
Se	5.789	Be	28.0
Si	5.839	Mg	28.8
S	5.87	Zn	30.7
Ge	5.882	Cd	34.7
C	5.913	C	26.4
		Si	34.8
		Ge	40.4
		Sn	167
		Mn	113

*Binding energies were calculated from the energetic positions of the 1S-2P transitions as observed in photoconductivity plus the binding energy of the 2P state of 1.429 meV.

**The ground state binding energy of the impurity is calculated by adding the theoretical binding energy of the excited state to the observed ground state to excited state transition energy.

The most versatile technique for growing these high-purity epitaxial layers of GaAs with precisely controlled doping profiles is without any doubt molecular beam epitaxy. The residual dopants found in nominally undoped GaAs grown by MBE are usually quite different from those in material grown by other techniques such as metal-organic chemical vapour deposition (MOCVD). The difference is especially marked for the residual p-type dopants found in MBE material. Figure 3.1 shows a comparison in the PL spectra for high-purity epitaxial GaAs grown by two different techniques. The MOCVD sample was grown in a low pressure horizontal reactor using trimethyl gallium (TMG) and arsine (AsH_3) diluted (5%) in hydrogen.(3.1) The 3.2 μm thick layer was n-type with $n = 2.5 \times 10^{14}$ cm^{-3}. The MBE epitaxial layer (6 μm thick) was grown at 630°C in a Varian GEN 2 machine where As_4 beams were employed. The nominally undoped sample is p-type with a residual acceptor concentration of ~10^{14} cm^{3}. The PL spectrum of both samples show the characteristic free exciton emission, X, along with the usual impurity related emissions; i.e. the donor bound exciton (D°,X), the free–hole to neutral donor transition (D°,h) and the acceptor bound exciton (A°,X). Table 3.2 summarizes the different recombination processes observed in high-purity GaAs.(3.2) The emission lines observed on the high-energy side of (D°,X) in the MBE sample has previously been attributed to various rotational excited states of the donors.(3.3) These rotational states correspond to the p-like distributions of the hole around the donor. Finally, the doublet observed at ~1512.4 meV in the MBE sample, which is unresolved in the MOCVD epitaxial layer, has been universally attributed to the effects of J-J coupling between the two holes and one electron involved in the acceptor bound exciton.(3.4-3.5) Such a

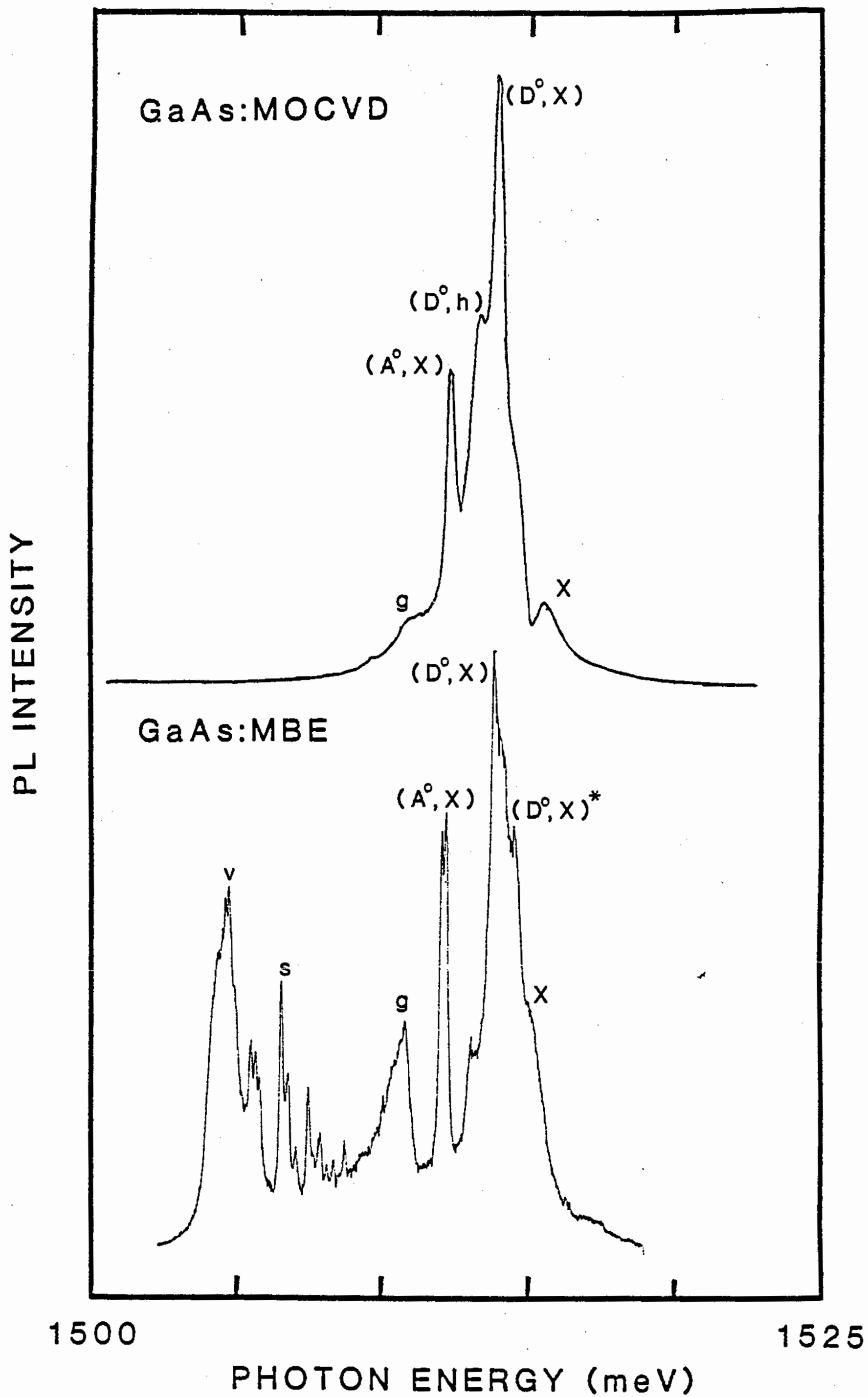

FIG. 3.1 Comparison between the low temperature (2K) photoluminescence emission spectra of a MOCVD (top) and MBE (bottom) GaAs sample.

TABLE 3.2 Recombination Processes in GaAs at 4.2 K[3.2]

	Symbol	Energy (meV)
Band gap energy	Eg	1519.2
n=2 state of free exciton	$X_{n=2}$	1518.1
n=1 state of free exciton-upper polariton branch	X	1515.3
free exciton-lower polariton branch	X	1515
rotational excited states of donor bound exciton	$(D^o,X)^*$	1514.9
exciton bound to neutral donor	(D^o,X)	1514.1
valence band to neutral donor transition	(D^o,h)	1513.3
exciton bound to ionized donor	(D^+,X)	1513.3
exciton bound to neutral acceptor; J = 1/2	$(A^o,X)_{J=1/2}$	1512.8
exciton bound to neutral acceptor; J = 3/2	$(A^o,X)_{J=3/2}$	1512.4
exciton bound to neutral acceptor; J = 5/2	$(A^o,X)_{J=5/2}$	1512.2

splitting in the (A^o,X) emission can be explained as follows: when two holes of angular momentum j = 3/2 occur in the bound exciton state, the Coulomb repulsion splits the two-hole state into the states of different total angular momentum which are allowed by the Pauli principle. Thus, the two holes can couple to give a total angular momentum of J = 0 or 2. The other possibilities allowed from coupling of angular momenta, i.e. J = 1 or 3, are excluded by the requirement that the resultant state must be totally antisymmetric. Each of these states is then coupled to the j = 1/2 electron to give the three possible states J = 1/2, 3/2 and 5/2. It was found[3.4-3.5] that the characteristic narrow doublet in the luminescence is produced by the decay of excitons bound to neutral

acceptors from the J = 5/2 and J = 3/2 exciton states, with the former lying lowest in energy. The further J = 1/2 bound exciton state is removed to a considerably higher energy and is very weak in luminescence emission due to depopulation of the level at these temperatures.

The most apparent difference between the two PL spectra of Fig. 3.1 is found at energies lower than (A^o,X), where up to 50 lines are observed in the MBE sample. Künzel and Ploog(3.6) first reported this series of *defect-related* PL lines in the 1504-1511 meV spectral region in nominally undoped p-type GaAs layers grown by MBE in which the arsenic source was As_4. They attributed these lines to optical transitions resulting from excitons bound to point defects with the simultaneous incorporation of an impurity inherent to the MBE growth process, probably carbon.(3.7,3.8) The point defects were believed to result from the complex interaction mechanism of As_4 molecules and Ga atoms during the growth process. They also noted that these additional PL transitions disappeared totally when As_2 instead of As_4 species were used. This behaviour was explained in terms of the growth mechanism. By using As_2, the arsenic concentration at the growing surface was much higher, reducing the number of vacancies available for native defect formation. This result is, however, by no means firmly established and no adequate microscopic model of the origin of these *defect-induced bound exciton (DIBE)* lines has been suggested.

3.2 Proposed Models for the DIBE

Since the discovery of the DIBE located in the 1504-1511 meV spectral region in high-purity MBE-grown GaAs, many models have been

proposed to account for both the large number of lines observed in the PL spectra, as well as the spectral range over which these lines occur. Various groups have studied these DIBE lines (also called the KP lines), taking into consideration the MBE growth conditions such as substrate temperature, arsenic species and doping level.[3.9-3.12] Lines in the same spectral region have also been reported once in material grown by the MOCVD technique, using TMG and AsH_3 as starting materials.[3.13] This series of lines was observed in films deposited under conditions that favor a high concentration of defects (i.e. low $[AsH_3]/[TMG]$ ratio).

Following the introductory work of Künzel and Ploog, more highly resolved DIBE PL spectra have been observed by other groups who have tried to introduce new models to explain the details of the structure, without as yet any satisfactory conclusion being reached as to their origin. Reynolds *et al.*,[3.14] who observed up to sixty subcomponents in the 1504-1511 meV region, interpreted these lines as discrete donor-acceptor pair transitions resulting from preferential pairing. They attributed the donor to a Si atom on a Ga sublattice, and the acceptor to a C atom on the As sublattice. In another investigation, Eaves *et al.*[3.15,3.16] fit the KP photoluminescence emission spectrum with a model of excitons bound to acceptor pairs of varying separation. In this case the mean distance between two acceptors becomes comparable to the free exciton radius, and the influence of other neighbouring neutral acceptors on the localization energy of the bound exciton must be considered. In their original model, the high energy line observed at 1511.19 meV (henceforth called g-line or line 47) was attributed to an isolated unidentified acceptor BE,[3.17-3.20] and the line lowest in

energy (1505.0 meV, also called v-line or line 1) was assigned to the nearest- neighbour acceptor pair BE. However, it was not before the work of Skolnick *et al.*,[3.21] who reported that most of the PL in this region was strongly polarized parallel to one of the <110> directions, that Eaves and co-workers came up with a *modified model*.[3.22] In this revised model they indicated that the acceptor pairs were preferentially oriented rather than randomly distributed, as was previously assumed in their original model. Further, they assigned the line at 1507 meV (line 14), which was found to be the most intense and strongly polarized of the series, to the nearest-neighbour pairs. The lines at lower energies (lines 1 to 13), found to be polarized in a different direction than the higher energy components, were assigned to transitions in which the defect pairs were left in an excited state following the exciton recombination. The preferential defect pair incorporation along the [110] direction rather than along [$\bar{1}$10] was proposed to be at the origin of the strong polarization of these lines. Finally, from their selectively excited PL and excitation experiments, Beye and co-workers[3.23] concluded that there were at least two distinct recombination processes involved in this exciton-like luminescence band. The anisotropy reflected by the polarization supported the fact that these groups were due to exciton recombination at axially oriented complex defects. Such centres were suggested to be complex defects acting as isoelectronic centres. In a more recent paper,[3.24] the same authors claimed to distinguish at least four sets of BE complexes related to distinct defect centres. The splitting patterns of the various BE systems were analyzed and an isoelectronic-like defect model

was again proposed to be most consistent with their experimental results.

Briones and Collins[3.10] were the first to report another series of lower energy transitions (d_n lines) which were present in the PL spectra of samples showing strong KP emission. These lines, observed in the energy region 1470-1490 meV, were attributed to free-to-bound and DAP transitions involving a series of *defect complex* acceptors.[3.25,3.26] They also correlated these d_n transitions with the KP lines suggesting that the luminescence in these two spectral regions be due to different transitions involving the same defects. This possible connection between the two series of lines was further supported by the polarized PL measurements of Skolnick *et al.*[3.27]

Recently, Zeeman spectroscopic investigations of the KP lines[3.18,3.28] revealed that, while the BE ground states (initial state in PL) were magnetically split, the binding centre ground states (final state in PL) involved in the KP transitions were not. This result implied a total angular momentum of $J = 0$ in the final state of the PL transition. Out of the various possibilities for the recombination mechanisms giving rise to the KP lines, relatively few fulfill the requirement of having a $J = 0$ final state. Certainly a model involving simple, single-acceptor BE is ruled out. All of the models discussed in this section (i.e. the DAP model of Reynolds,[3.14] the acceptor pair BE of Eaves[3.15,3.16] and the isoelectronic BE of Beye[3.23,3.24]) share the common restriction on the angular momentum having a $J = 0$ final state. Furthermore, another model which could explain both the Zeeman spectra and the d_n lines was the axial double-acceptor BE model proposed by Skolnick,[3.28] which encompassed

both the earlier proposal that the binding centres consisted of pairs of single-acceptors,[3.15,3.16] along with the new possibility of an isoelectronic defect paired with a double acceptor. Skolnick *et al.*[3.27] supported this model by detecting satellites of some of the KP lines which they interpreted as the 2S two-hole transitions of the double-acceptor bound excitons, but in the absence of other transitions in the two-hole series, this assignment was not definitive.

It is clear that many models have been proposed to explain the multi-line spectra; none of these, however, can yet completely describe the experimentally observed results. The model proposed by Eaves *et al.*[3.15,3.16] cannot account for the density of lines in the 7 meV energy range. However, lifetime and thermalization data[3.16,3.20,3.21] confirm that the BE model is to be preferred over the DAP model. Furthermore, the DAP model is difficult to reconcile with the fact that the KP lines are quite strong in samples which have virtually no donor BE or free-hole to donor luminescence. In addition, the lack of a natural place for the g-line (line 47) in the spectra[3.17,3.18] and the measured activation energies which vary from 4 meV at the high energy end to 7 meV at the low energy end of the spectrum go against the DAP model. Finally, both the DAP and isoelectronic BE model cannot explain the apparent existence of a bound hole in the final state of the transition, deduced from the observation of two-hole satellite of the KP lines.

The aim of the present chapter is to present additional information on the nature of these bound excitons. More detailed transient results for the KP lines are reported. Resonant and nonresonant excitation, coupled with time-resolved techniques, provide results which support the

model that the KP series consist of excitons bound to a series of acceptors. New details of the properties of the BE and acceptors will be revealed, and the direct connection between this acceptor series and the d_n lines is also established. We also demonstrate that the V-band region (lines 1-4) can be entirely accounted for in terms of replicas of the higher KP lines due to an acceptor ground state splitting, and determine the size of this splitting for a number of the KP lines. Finally, we will conclude by presenting Zeeman results which show conclusively that the axial defects responsible for this excitonic series result from two nearby single-acceptors or from a double-acceptor coupled with an isoelectronic defect in good agreement with the results obtained by Skolnick.[3.28]

3.3 Nonresonant Excitation

The MBE GaAs sample used in the present study (C03160) was grown at AT&T Bell Laboratories and is known to be one of the best wafers for the study of the DIBE lines.[3.27] This 6 μm thick epitaxial layer was grown at 630°C on a (001) oriented semi-insulating GaAs substrate. The nominally undoped sample is p-type with a residual acceptor concentration of ~10^{14} cm^3. In Figure 3.2, a high-resolution PL spectrum of the defect bound exciton lines is shown. The spectrum is excited with the dye laser tuned to the free exciton energy at 1515 meV and was found to produce maximum PL intensity. The numbering scheme used for the identification of the KP lines is the same as the one introduced by Skolnick.[3.21] Spectra are shown for two polarizations: $\vec{E}$ parallel to the [$\bar{1}$10] direction (curve a), and $\vec{E}$ parallel to the [110] direction (curve b). The high energy doublet observed at ~1512.4 meV is

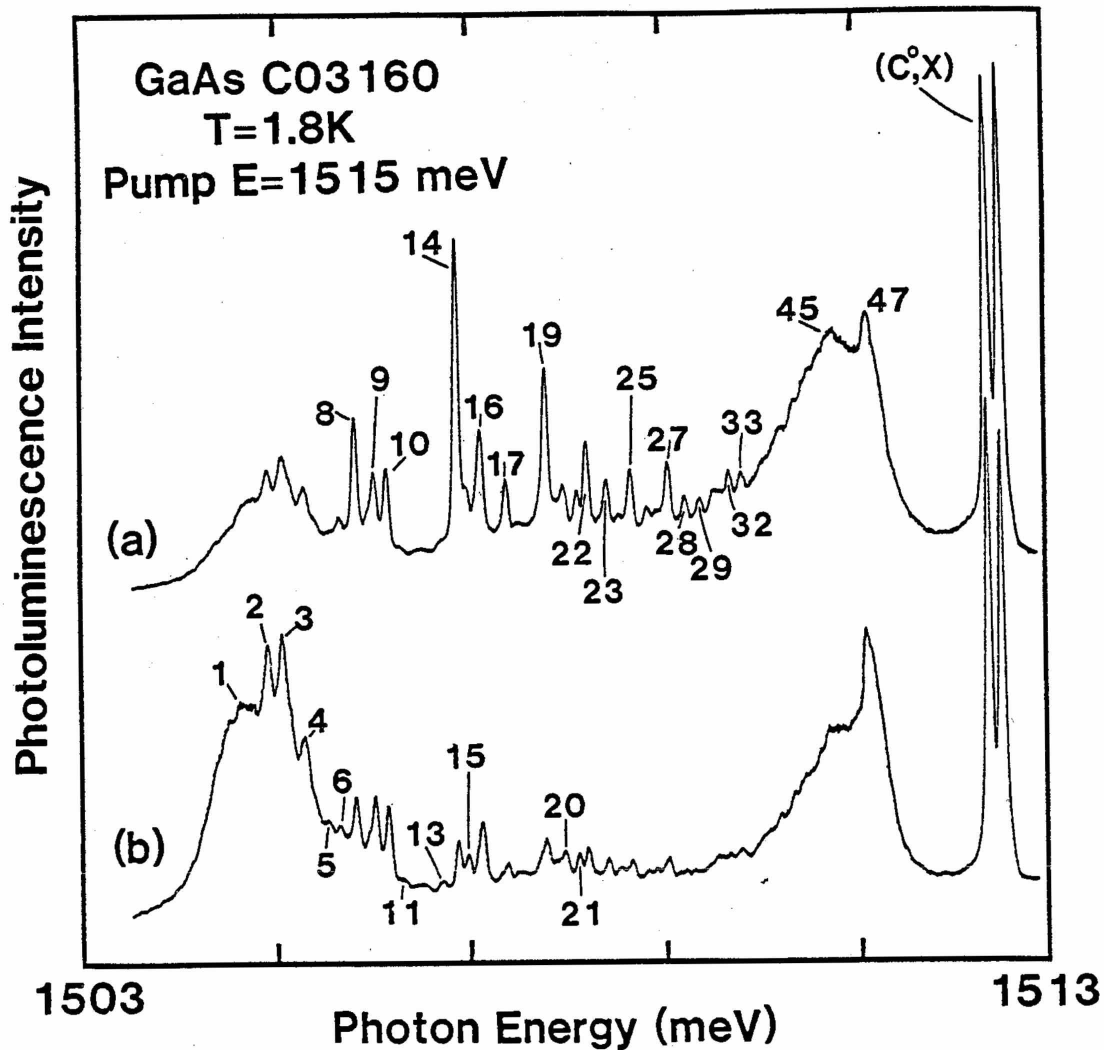

FIG. 3.2 High-resolution PL spectrum of the KP series using the numbering scheme of Skolnick *et al.*[3.21] (a) shows PL with $\vec{E}$ polarized parallel to [$\bar{1}$10], while in (b) $\vec{E}$ is parallel to [110], the sample surface being normal to [001]. (C°,X) is the Carbon acceptor bound exciton doublet.

due to the Carbon acceptor bound exciton (C°,X) and was found to have equal intensity in the two polarizations, as expected for a point defect. However, the polarization dependence of the KP lines is easily detected and can be divided into two groups: the sharp lines 14, 16, 17, 19, 22, 23, 25, 27...etc are predominantly polarized with $\vec{E}$ parallel to [$\bar{1}$10] and are labeled as the A group; whereas the B group of lines (1-4) are predominantly polarized with $\vec{E}$ parallel to [110]. As discussed by Skolnick,(3.21) the A group of lines was attributed to σ dipole transitions resulting from bound exciton recombination at defect pairs of varying separation oriented along [110], with the strongest line, 14, suggested to arise from the nearest-neighbour pairs. The polarization of the group B lines is consistent with σ oscillators with axes oriented in the [$\bar{1}$10] direction. As mentioned in section 3.2, the g-line region is observed with a greater or lesser intensity in all epilayer growth techniques. This luminescence emission is broadened to lower energy and superimposed on this low energy shoulder are a number of discrete lines (lines 34 to 46). Line 47, contrary to the components superimposed on the low energy shoulder, was found to be unpolarized. There exists some controversy as to the origin of this line, and two models have been proposed as the source of this emission. The first one consists of an acceptor bound exciton(3.19,3.20) and the other involves an exciton bound to a two-acceptor-one-donor complex.(3.18) In the latter process, the initial state is postulated to consist of two excitons, each bound to neutral acceptors in the presence of a neutral donor. One of the excitons decays, giving up part of its energy to transfer the other exciton to the neutral donor in either its ground state or its first rotational state. For such a model to be

valid, one would expect this emission line to be very sensitive to the exciton density and thus vanish at low excitation intensity due to the very low probability of such a two-exciton process. In Figure 3.3, the PL emission spectra is shown for two excitation powers in the 1475-1525 meV energy region. The above band gap excitation was provided by the 632.8 nm line of a He-Ne laser and the luminescent photons were collected using the imaging photomultiplier tube. In contradiction to what is expected from the two acceptor BE-one donor model, line 47 does not disappear when the intensity of excitation is reduced by four orders of magnitude. Furthermore, the relative intensity of line 47 has in fact increased with respect to the single Carbon acceptor bound exciton which is next to line 47 at higher energy. Thus the complicated model proposed by Reynolds[3.14] is very unlikely to be valid. Using resonant excitation along with lifetime measurements, it will be shown in section 3.5 that the g-line can be assigned to an acceptor bound exciton, and that it has a different origin than the lower energy KP lines (lines 1 to 46).

Another interesting feature related to Figure 3.3 is the luminescence band located between 1485 and 1495 meV. These luminescent transitions have been extensively studied in the past[3.26,3.29] and were attributed to free-electron to acceptor (e,A^{o}) and DAP transitions. As is always the case in MBE material, the dominant residual acceptor is Carbon. The peaks observed at ~1489 meV and ~1493 meV in the low intensity spectrum are attributed to DAP, (D^{o},C^{o}), and free-to-bound, (e,C^{o}), transitions involving Carbon acceptor. The high energy shoulder, (e,A^{o}), located at 1494 meV has recently been observed[3.30] in a number of vapour phase epitaxial and MOCVD GaAs samples. This

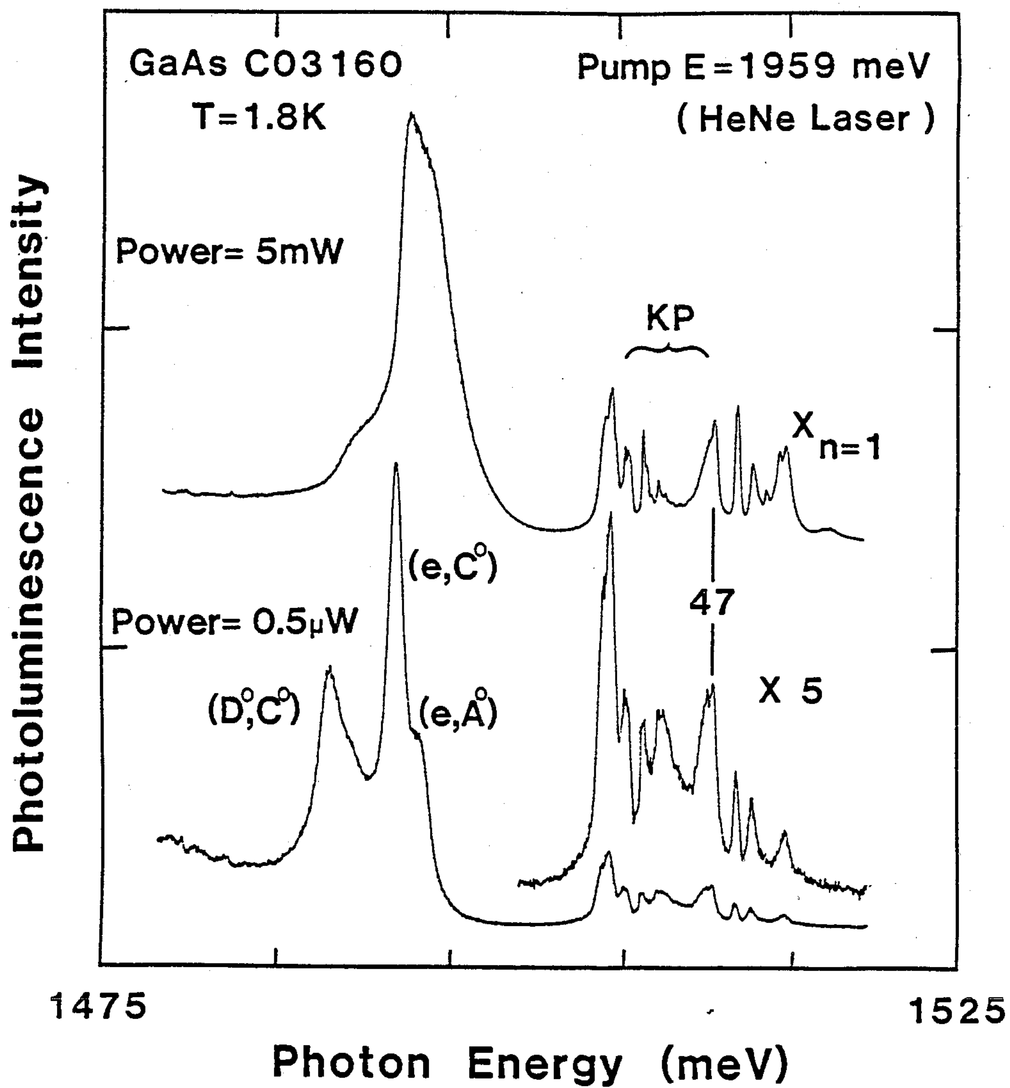

FIG. 3.3 Low temperature PL spectra taken at different excitation power. The 632.8 nm line of a He-Ne laser was used as excitation source. The laser spot size was ~12.5 mm^2.

transition has been assigned to a free-to-bound transition involving an unknown acceptor having a binding energy of 25.2±0.1 meV, in agreement with our data. A further characteristic of these luminescent bands is the fact that the peak ratio $(e,C^o)/(D^o,C^o)$ changes for the different excitation level used. This can be explained from the saturation of the (D^o,C^o) recombination process under high pumping conditions, where most of the donors which would otherwise have been ionized due to compensation are photoneutralized, and further increases in the (D^o,C^o) intensity can result only from further photoneutralization of the acceptors, which is also a saturable process. The (e,C^o) intensity, however, is proportional to the free-electron concentration and does not saturate for the excitation levels used here. Finally, as the excitation intensity is increased by 4 orders of magnitude at a constant sample temperature of 1.8 K, the (D^o,C^o) peak shifts to higher energy. This effect is due to a shift of the predominant recombination pathway to one involving closer (D^o,C^o) pairs, which have shorter lifetimes and therefore are not saturated as quickly as the more distant pairs. As was previously mentioned in Chapter 1, closely spaced pair recombination produces higher energy photons due to the Coulomb interaction of the pair in the final state.

It has recently been suggested[3.28] that the KP series might originate from an exciton bound to double-acceptor-isoelectronic centre pair of varying separation. Assuming that such a double-acceptor is present in a GaAs epitaxial layer, some free-to-bound or DAP recombination involving the first ionized state of this double-acceptor should be observed at lower energy. Figure 3.4 shows a low temperature PL emission spectrum from 1280 to 1520 meV. The sharp luminescence

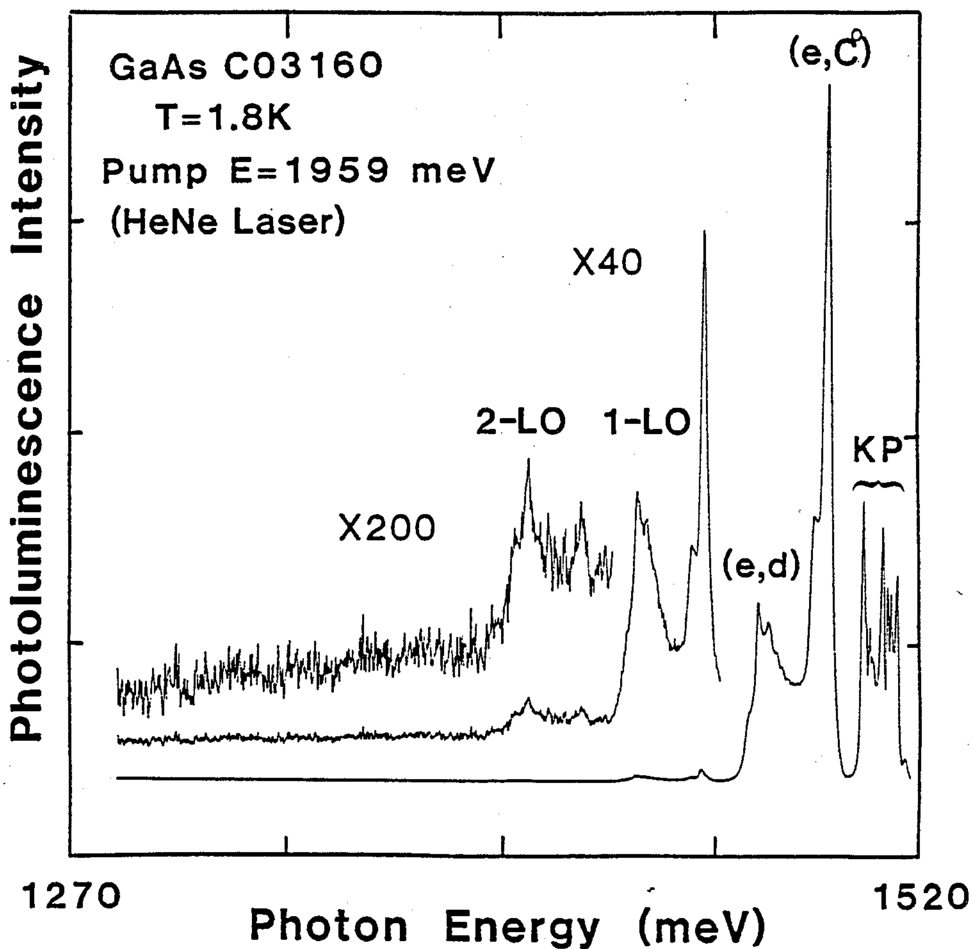

FIG.3.4 PL emission spectrum using above band gap excitation (632.8 nm). The first series of peaks (1505-1515 meV) correspond to the near band gap emission (free and bound exciton along with the KP lines). The series of peaksobserved between 1470-1500 meV consist of free-electron to neutral acceptor transition and Donor-Acceptor pairs involving Carbon and *defect complex* acceptors.

features observed between 1504 and 1520 meV are due to excitonic recombination. The next series of peaks between 1460 and 1500 meV are attributed to free-electron and donor to acceptor involving Carbon and the deeper d_n acceptors as first reported by Briones and Collins.[3.10] Only the free-to-bound transitions, (e,C^o) and (e,d), are indicated on the figure as they are much more intense than the DAP recombination, reflecting the intensity of excitation used for this spectrum. The luminescence band label (e,d) (also known as the d_n transitions), represent recombination involving free-electrons and deep acceptors. These same acceptors are believed to be at the origin of the higher energy KP lines and will be discussed in detail in section 3.6. Finally, besides the one and two longitudinal optical phonon replicas of the (e,C^o) and (e,d) peaks, no other luminescence band was observed at lower energy. However, note the increase in the intensity ratio $I(e,d)/I(e,C^o)$ in going from the no-phonon to the 2-LO replica. This effect can be explained as follows. As the binding energy of the hole bound to a single substitutional impurity (acceptor) increases, it becomes more localized and the interaction of the hole with the lattice vibrations or the hole-phonon coupling gets stronger.

In conclusion, from the above observations, it seems somewhat strange that no luminescence peak involving the first ionized state of the double-acceptor was detected, as would be expected if one accepts the model involving the double-acceptor-isoelectronic centre pairs to be at the origin of the KP lines. However, other competing mechanisms could explain the lack of radiative structure.

3.4 Time-Resolved PL Spectra

A series of time-resolved spectra of sample C03160 using above band gap excitation are shown in Figure 3.5. The sample was immersed in superfluid helium and the luminescence was excited using the mode-locked, cavity-dumped dye laser system described in Chapter 2 with a repetition rate of 4 MHz. The luminescence was dispersed by a double 3/4 m spectrometer and detected by the time-correlated photon counting system described in section 2.4-1. The time window used for the acquisition of the spectra varied from 2.5 ns (for the first four spectra) to 10.8 ns (for the last spectrum). This series of spectra clearly shows that the acceptor bound exciton (C^o,X) and line 47, with its low-energy wing, decay much more quickly than the lower energy lines. The luminescence decay curves for some of these individual lines were recorded using above band gap excitation and are shown in Figure 3.6. The lifetimes of the different luminescent transitions were obtained by fitting an exponential decay over the first decade of intensity. The Carbon acceptor bound exciton (C^o,X) (not shown in Fig. 3.6) and line 47 were found to have identical lifetimes of 1.3±0.1 ns. As for the lower energy components, the lifetimes were found to be almost constant in going from line 27 to 3, as shown by the constant intensity ratios of the lines in the different time windows of Figure 3.5. An initial exponential decay time constant of 2.7±0.1 ns was found for line 3. However, an important change in the shape of the decay curve is observed in going from line 47 to line 27. A second, long-lived component, having a lifetime of about 24±3 ns, began to appear at line 27 and became relatively stronger for the lower energy

FIG. 3.5 Series of time-resolved spectra taken at 1.8 K. The time windows are as indicated on the figure. The sample was excited by 814 nm radiation at a repetition rate of 4 MHz with an average excitation density of 50 mW/cm^2. After the initial fast decay of the acceptor bound exciton (C°,X) and the g-line (47), the shape of the spectra remains unchanged during later time windows out to 100 ns after the laser pulse.

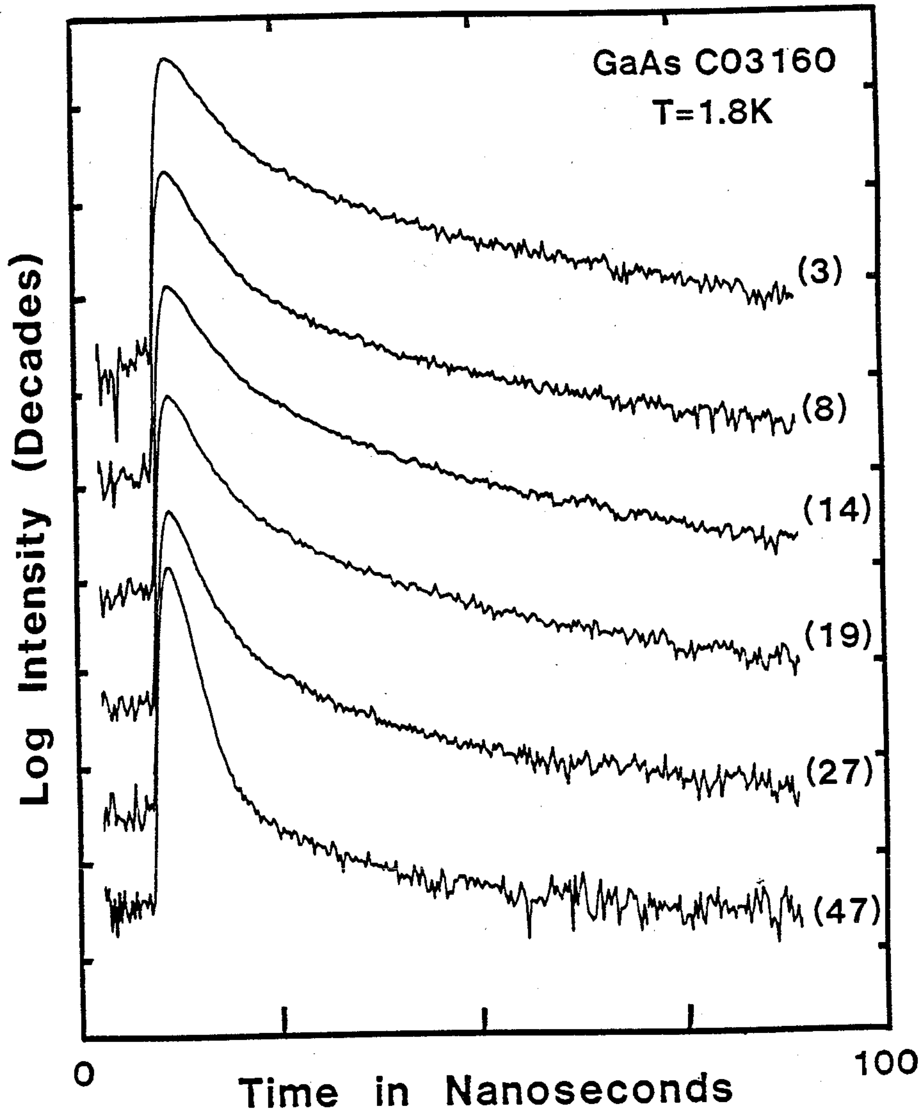

FIG. 3.6 Luminescence decay measurement of selected lines shown in Fig. 3.5 under identical experimental conditions. At this excitation density the lifetimes of the lines are the following: 2.7, 2.5, 2.4, 2.0, 1.75 and 1.3 ns (±0.1 ns) corresponding to lines 3 to 47 respectively. The long-lived component had a decay of 24 ns (±3 ns).

components. It is believed that the fast components of all these decays, which are more characteristic of direct gap impurity bound excitons, are the true radiative lifetime, while the long components are due to the transfer of excitation from some unidentified long-lived source, possibly from a nonradiative excited state of the BE. As we shall see in section 3.8, the initial state of the PL transition is composed of a degenerate $J = 1$ and $J = 2$ states whereas the final state has $J = 0$. The long-lived component observed in the exciton decay could originate from the dipole forbidden $J = 2$ to $J = 0$ transition. A second origin for this long-lived component might come from the capture time of the exciton by the binding center. These results will be contrasted with the resonant pumping experiments reported in section 3.6.

3.5 Photoluminescence Excitation Spectra

The lower energy defect-complex acceptor peaks (d_n lines), first reported by Briones and Collins, were recently studied by Skromme *et al.*[3.30] who confirmed the nature of these transitions as arising from free-electron-to-acceptor (e,d) and DAP recombination. By increasing the sample temperature from 1.8 K to 20.9 K they were able to observe the change from the dominant DAP peak at low temperature to the free-to-bound transition at high temperature due to thermal ionization of the shallow donors. But more importantly, the PL from these d_n transitions also showed marked polarization, with $\vec{E}$ predominantly parallel to [110],[3.27] providing even stronger support for a correlation between the polarized defect bound excition lines (KP lines) and these broader, lower energy, d_n lines.

High-resolution photoluminescence excitation spectra with the dye laser scanned through the 1503-1511 bound exciton region are shown in Figure 3.7. The spectrometer detection for the bottom spectrum (a) was set to 1470 meV (the low energy edge of the d_n transition), with wide slits being employed to give a detection bandpass of ~2 meV. This spectrum was acquired for [$\bar{1}$10] laser polarization. The most important result of this figure is that all the sharp PL lines from 8 up to at least 35 are observed in PLE. The lines from 14 to 35 have very similar relative intensities to those found in PL (Figure 3.2). Taken together with the result that no thermalization between the sharp lines was observed in PL spectra from 2 to 20 K,[3.27] nor in PLE from 2 to 4.2 K (section 3.7), it can be deduced that all the bound exciton lines (at least from line 8 to 47), are transitions from the lowest state of the bound exciton to the ground state of the defect, and that each line observed arises from a transition at an independent centre. Line 47, which is strong in the PL spectra of Figure 3.2, is very weak and noisy in PLE, even when the spectrometer was shifted to higher energy, possibly implying that line 47 has a separate origin from the rest of the KP series.

The complete absence in PLE of the broad feature underlying lines 1-4 observed in PL indicates that this structure arises from a final state splitting in the PL experiment (initial state in PLE), the upper levels giving rise to this feature not being populated at the low temperature employed for Fig. 3.7. It may be that each strong line in the higher-lying KP series (lines 8 to 45) has a broad low energy satellite in the 1-4 region. This conclusion is supported by the PLE spectra of Figure 3.7 (b) and (c) where the spectrometer detection was

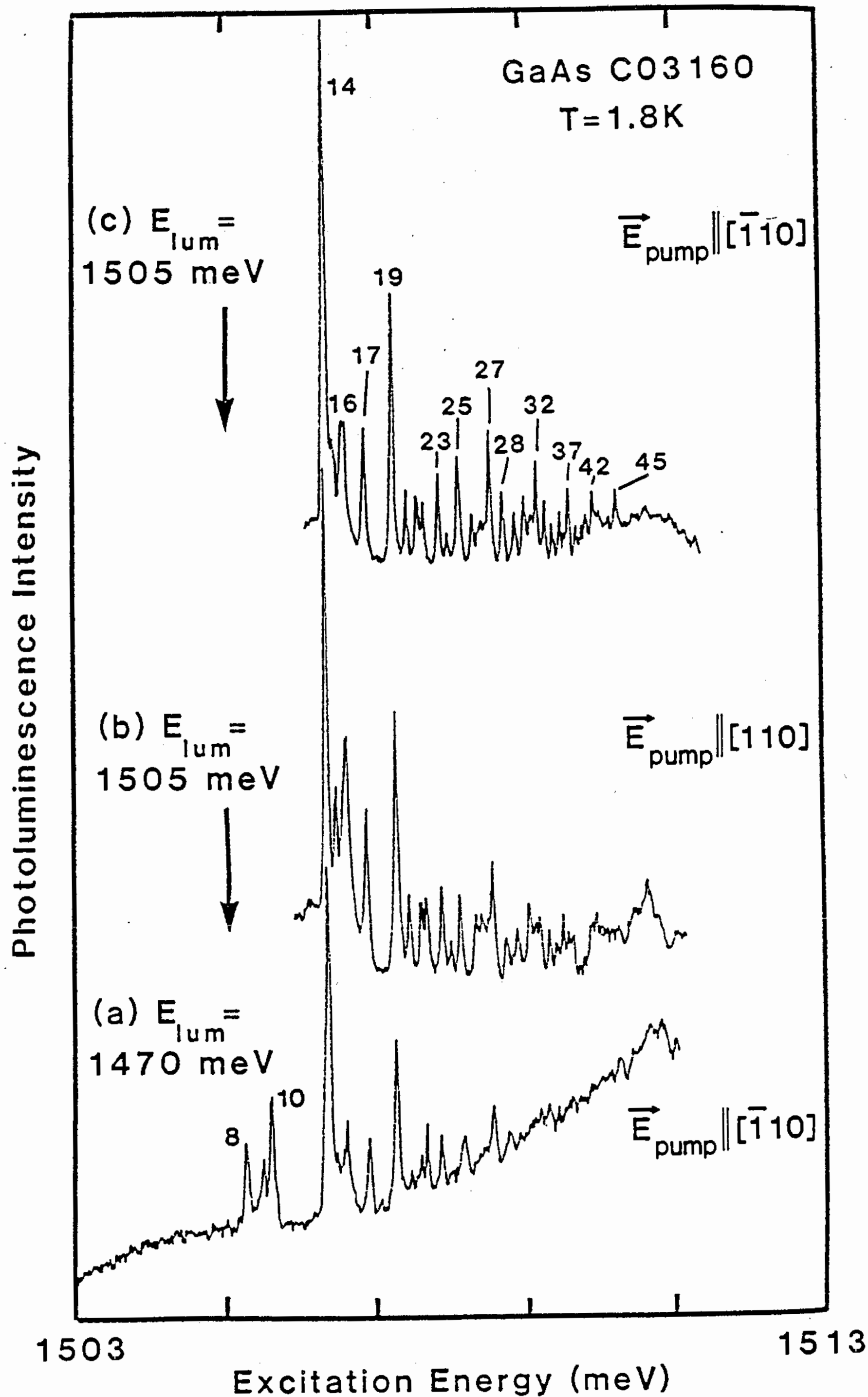

FIG. 3.7 PL excitation spectra, at 1.8 K, recorded through the defect-bound exciton region from 1504 to 1511 meV. The spectrometer detection is set at 1470 meV for (a) and at 1505 meV for (b) and (c) (2 meV bandpass). The spectra are shown for $[\bar{1}10]$, curves (a) and (c), and [110], curve (b), laser polarization.

set in the middle of the V-band at 1505 meV. Spectra are shown for both [110] and [1̄10] laser polarization. Again, all the features characteristic to the KP series observed in the PL spectra are present in the PLE experiment. Lines 8, 9 and 10 also had a replica in the V-band region but because of the very small separation between the collection wavelength and the laser wavelength, they had to be obtained using another optical technique (section 3.6). Here again, line 47 was found to be very weak in either polarization, suggesting once more a separate origin for this line.

The PLE spectrum of Figure 3.7(a) was obtained with the spectrometer set at 1470 meV. It is clear that spectral features related to the defect bound exciton lines are being detected in this region. It is the goal of the next section to look at these low energy satellites in more detail.

3.6 Resonant Excitation of the DIBE Lines

The principal recombination paths of excitons bound to neutral acceptors leave the acceptors in their ground electronic state. Simultaneously, other processes exist where the holes remaining trapped on the acceptors are left in an excited state. They are responsible for the low energy two-hole satellites. The acceptor two-hole replicas are, in general, difficult to observe in GaAs since they occur in the same spectral region as the DAP and free-electron-to-acceptor transitions. Time-resolved spectroscopy should be of utility since the decay of the two-hole transitions must follow that of the acceptor bound exciton, whereas the free-to-bound and DAP transitions in this region have a

decay time of hundreds of nanoseconds. By setting short time windows, it should be possible to discriminate against the unwanted long-lived luminescence. Using the Mepsicron imaging photomultiplier tube and the fast time windowing technique mentioned in section 2.4-2, each individual line of the KP spectrum was resonantly excited. To ensure that the laser was in resonance with each line, the energy of the pumping laser was varied from 1512 to 1504 meV in increments of 0.05 meV. Without both the parallel collection capabilities of the Mepsicron detector and the temporal resolution necessary to reduce dark count and to discriminate against the obscuring longer-lived DAP luminescence, an experiment of this nature would have been very time-consuming, if not impossible. A typical spectrum collected with this system is shown in Figure 3.8. The sample was excited with ~5 mW of 1508.70 meV laser radiation (resonant with line 25 of the KP series), and pulsed at 4 MHz. The luminescence was dispersed by means of a 3/4 m spectrometer equipped with 1200 grooves/mm grating operating in first order resulting in an overall system resolution of ~0.10 meV. The short time window was set at 5 ns. The features of interest in this figure are the many sharp lines seen in curve (a), which are lost against the strong, but long-lived, DAP luminescence. A spectrum acquired without time resolution would be similar to Figure 3.8(b) and any identification of the various emission peaks would have been impossible.

Let us start with the controversial high energy component of the KP series, i.e. line 47. As discussed in section 3.4, the observed similarity of the decays of the lines 47 and (C^{o},X) suggests that the line 47 is due to an acceptor bound exciton. This also has been suggested by Contour *et al.*[3.19] on the basis of resonant (continuous

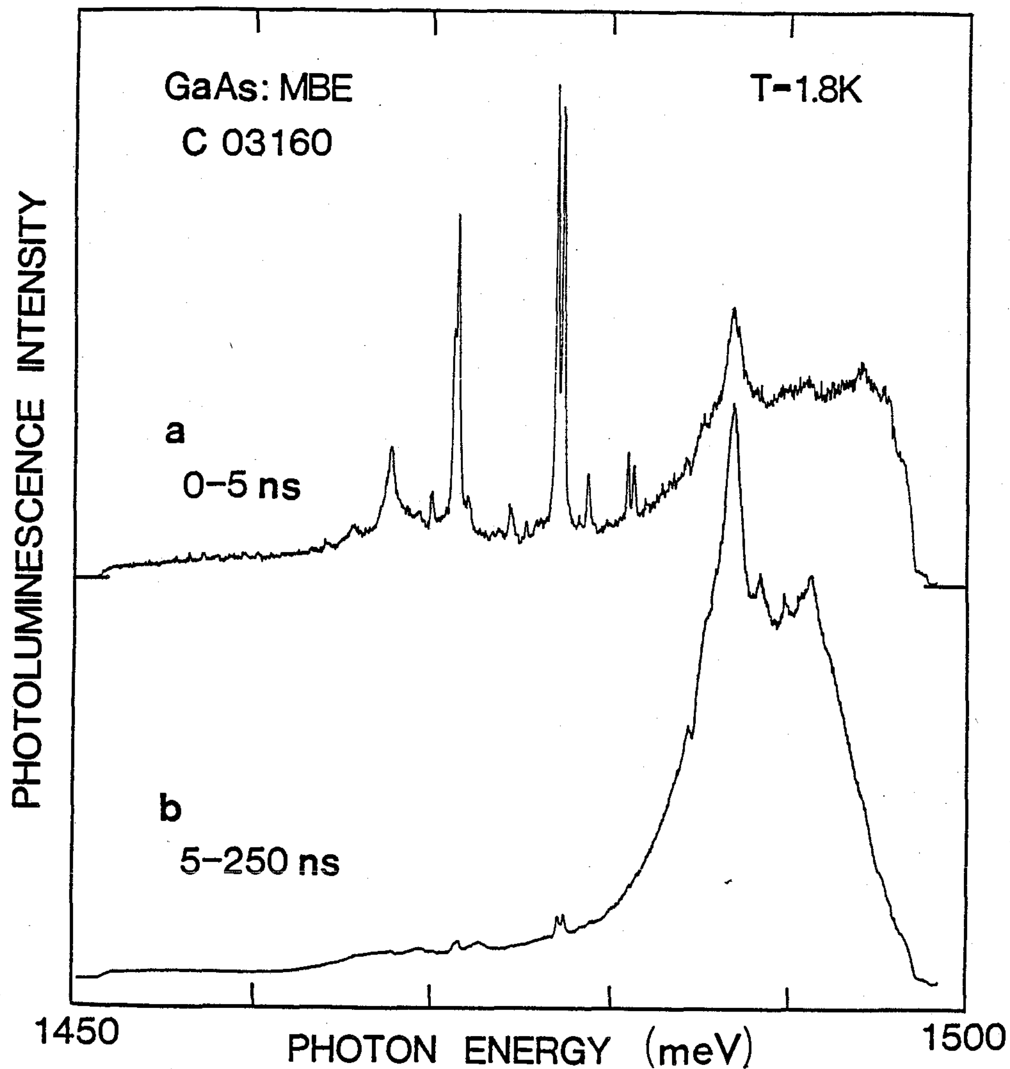

FIG. 3.8 Time-resolved selective excitation PL spectra obtained using the parallel collection system of Fig. 2.4. The scale of the slow time window (b) is 20 times greater than the fast window (a). The sample was excited with ~5 mW of 1508.70 meV (line 19) laser radiation, pulsed at 4 MHz. The acquisition time was 15 min. The features of interest are the many sharp lines seen in (a), which are lost against the strong, but long-lived, DAP luminescence which dominates (b). A spectrum acquired without time resolution would be almost identical to spectrum (b).

wave) excitation with the observation of a two-hole replica of line 47. Their results were somewhat hard to interpret since no time rejection technique was used to discriminate against longer-lived luminescence. Figure 3.9 shows the luminescence spectra when line 47 is pumped resonantly at 1511.20 meV (curve (c)). The laser energy was also set to pump the polariton resonantly at 1515 meV (curve (a)). Each spectrum shown in the figure was collected for the first 5 nanoseconds following the laser pulse. When the laser energy was resonant with the polariton, a peak at 1497.0 meV was observed. This peak was also detected, with somewhat lower intensity, when the laser energy was in resonance with line 47 at 1511.20 meV and disappeared when the laser was detuned 0.1 meV away from line 47 at 1511.10 and 1511.30 meV. On the basis of the transient behaviour of this luminescence peak and on the resonant excitation, the line observed at 1497.0 meV has been interpreted as the 1S-2S two-hole replica of line 47, in good agreement with the result obtained by Steiner *et al.*[3.20] on a different sample. The salient result of this work is to show that line 47 (g-line) is due to the recombination of a shallow acceptor bound exciton. Our assignment of this replica puts the 1S-2S energy difference of the g-acceptor at 14.2±0.1 meV. Comparing this value with the well-known Carbon acceptor 1S-2S splitting, one obtains a g-acceptor binding energy of 21.7±0.2 meV in good agreement with Contour and co-workers.[3.19] The emission peaks observed in the 1485-1492 meV region in curves (b), (c) and (d) are associated with the selectively excited DAP involving excited states of the Carbon acceptor and are independent of the KP emission lines. (These lines will be discussed in detail later in this section.) The peak observed at 1493.9 meV, labeled (C^o,X) 2S, when pumped at 1515 meV,

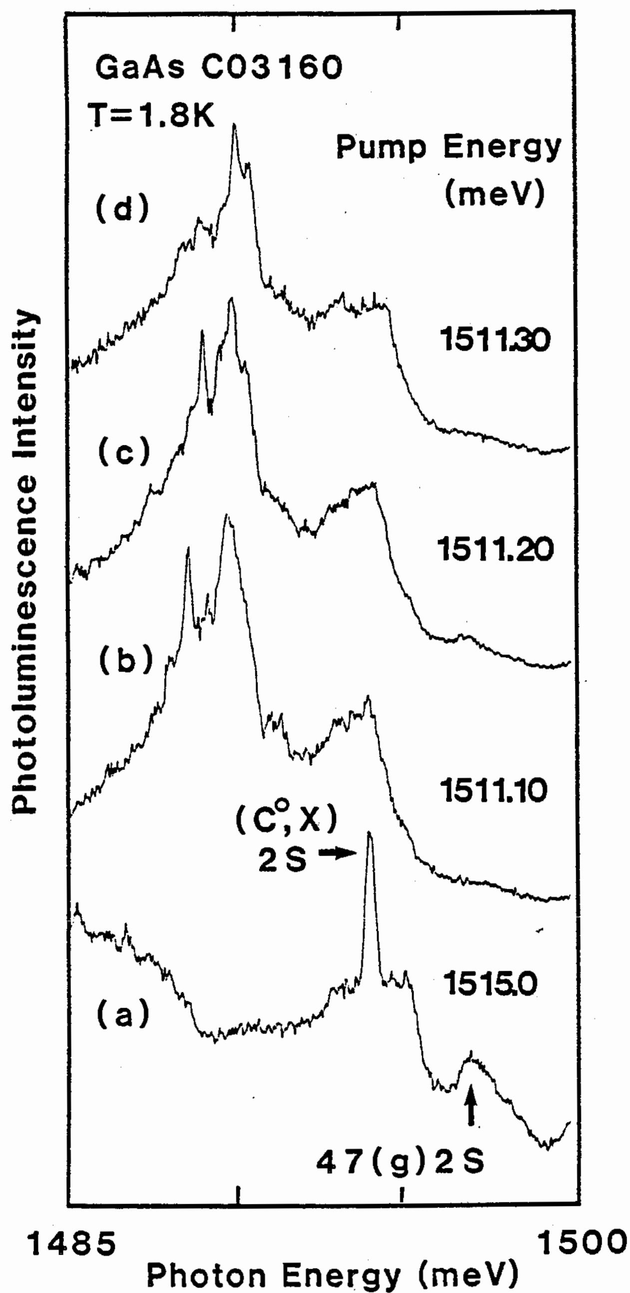

FIG. 3.9 PL spectra in the 1485-1500 meV region with the dye laser energy tuned to be in resonance with the polariton (curve (a)) and line 47(g) (curve (c)). Curves (b) and (d) were obtained when the laser energy was tuned 0.1 meV away from line 47. The spectra correspond to photon emitted in the first 5 nanoseconds following the laser pulses.

is due to the Carbon two-hole transition and is also independent of the KP series[3.4,3.5]

Let us now concentrate on the lower energy lines of the KP series. The PL spectra in the 1460-1490 meV region for a number of different excitation energies are shown in Figures 3.10 and 3.11. Here again, all the curves shown represent only the photons which were emitted in the first 5 nanoseconds after the laser pulse. As the dye laser position is tuned to lower energy to be resonant with the various peaks of the KP series, a number of sharp satellites are observed. None of these lines, however, were observed when the laser energy was not in resonance with the KP lines. In their paper, Skolnick and co-workers[3.27] resonantly excited some of the peaks in the 1504-1512 meV region. They also observed low energy satellites when the laser was in resonance with one of the defect bound excition lines but could not explain the origin of most of the lines as the satellite structure became more and more complicated with decreasing laser energy. However, they followed the evolution of one strong line when pumping resonantly lines 32 to 22. This low energy satellite was assigned to the 2S two-hole transitions of each of the individual defect bound excitons. Figure 3.10 shows some luminescence spectra when lines 42 to 32 are pumped resonantly. The sharp peaks at high energies are attributed to the 2S two-hole satellites. In the figure, the luminescence photon energy scale corresponds to the resonant spectrum of line 42. The other spectra, obtained when pumping lines 32, 27, 25 and 22 resonantly, have been shifted from lower energies such that the 3S excited state of the two-hole satellite transitions would line up. As one can see, there exist some discrepancies in the position of the 2S states. This

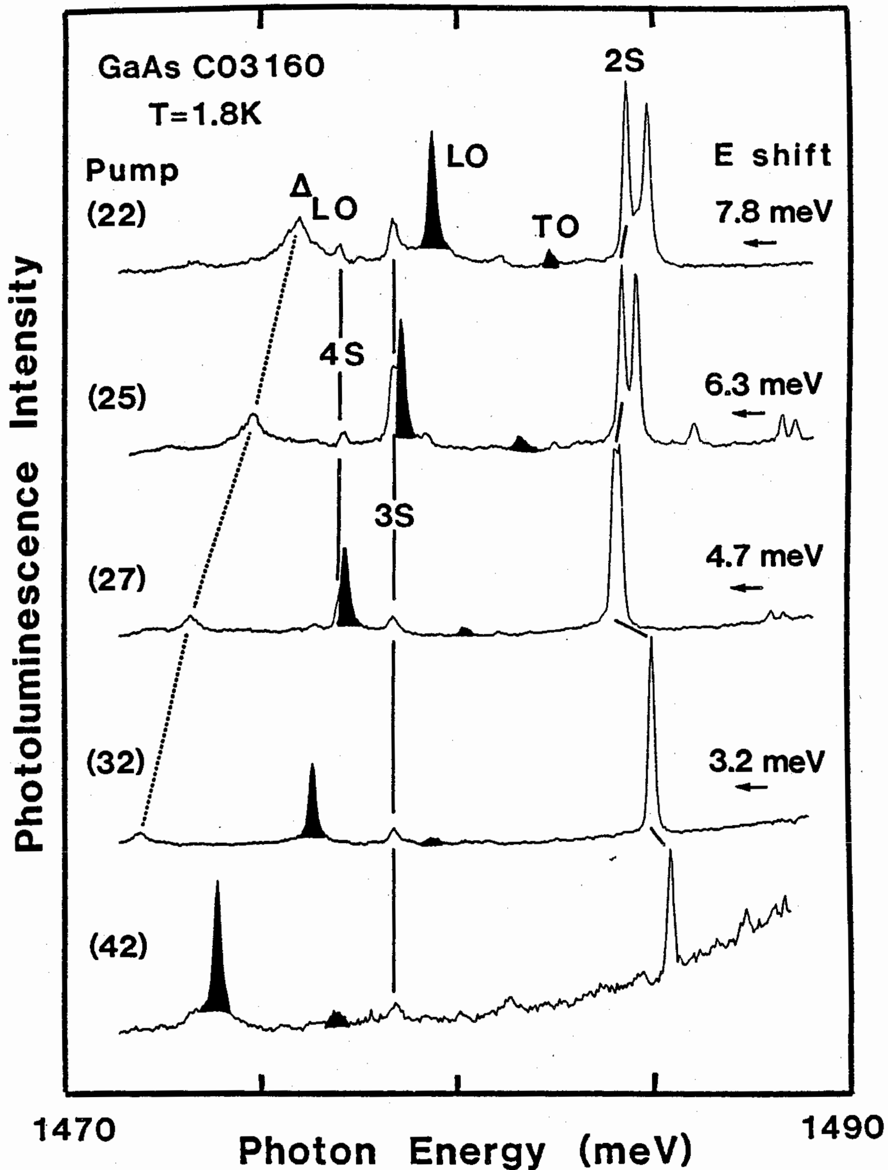

FIG. 3.10 Selectively excited PL spectra with the laser tuned successively to resonance with different lines of the KP series. The spectra, taken at 1.8 K, correspond to the first 5 nanoseconds after the laser pulse. The energy scale corresponds to the resonant spectrum of line 42. The other spectra, when pumped line 32-22 have been shifted to lower energies by the amount indicated on the figure such that the 3S excited state of the two-hole satellites would line up. The shaded peaks correspond to the TO and LO Raman lines.

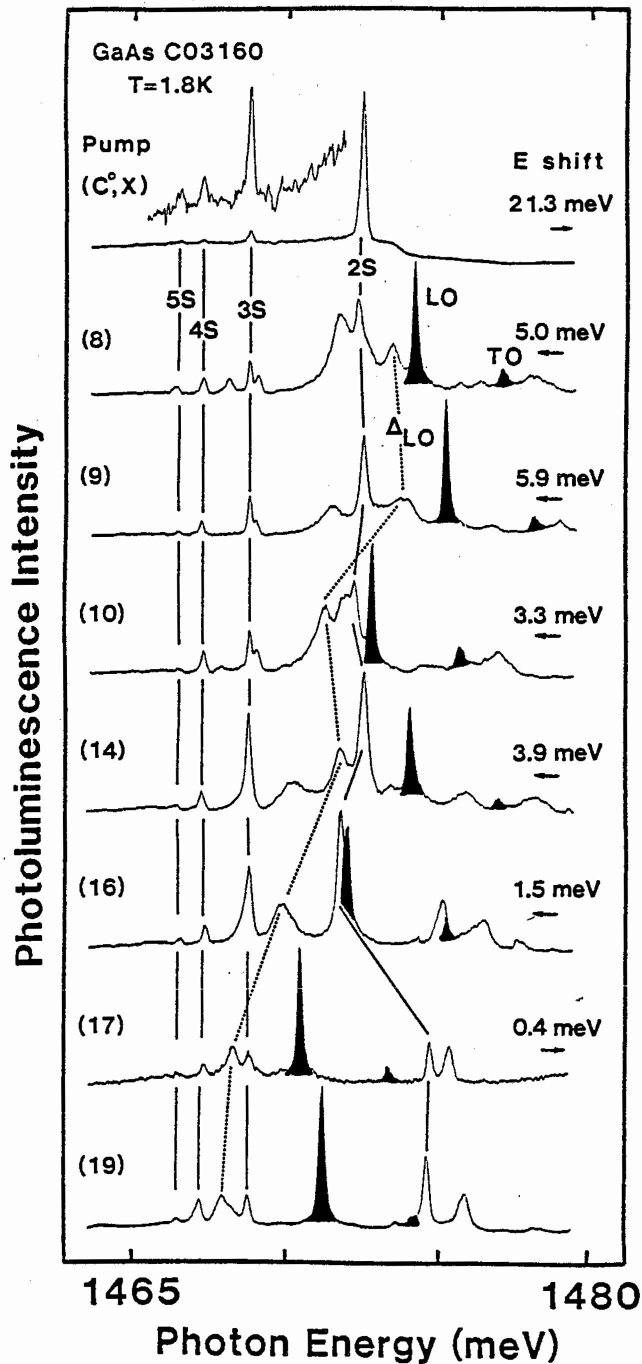

FIG. 3.11 Resonantly excited two-hole replica spectra of some of the KP lines (numbererd on the left) are compared with that of the Carbon acceptor BE (top). The 3S, 4S and 5S transitions have all been aligned - the energy scale applies to the bottom (line 19) spectrum, while the energy shifts required to align the other spectra are shown on the right. The shaded lines are the LO and TO phonon Raman lines, while Δ-LO is the LO phonon replica of the selectively excited Δ transition.

behaviour can be explained by the different acceptors having different central cell correction (chemical shift). The shaded lines are the LO and TO Raman transitions. The weak Δ_{LO} peak observed at lower energy is due to the LO-phonon replica of the satellite observed in the broad structure underlying peaks 1-4 and will be discussed later.

For excitation below line 22, the satellite structure became more complicated. Figure 3.11 shows some resonant spectra for lines 19 to 8. To help in the identification of the different peaks, a comparison between the acceptor excited state spectrum of Carbon, as obtained from the resonantly excited Carbon acceptor BE (C^o,X) two-hole spectrum,[3.31] and some typical resonant PL spectra obtained by pumping seven of the lower KP lines are shown. As in Figure 3.10, the luminescence photon energy scale corresponds to the resonant spectrum of line 19 (bottom spectrum). The other spectra have been shifted in energy so as to line up the 3S, 4S and 5S excited states of the two-hole replicas. An excellent match is obtained for the 3S, 4S and 5S excited states of the various KP lines and Carbon acceptor, proving conclusively the acceptor BE nature of these lines, and the need of at least one hole in the final state of the luminescence transitions. Here again, the discrepancies, as in the position of the 2S excited state, can be explained by the different central cell corrections of the different acceptors, and to the interaction of the 2S states with the optical phonons. This attribution implies that the defect-induced bound exciton lines, first reported by Künzel and Ploog, correspond to exciton recombination at neutral acceptor centres where the acceptor is left in its 1S ground state after recombination. The two-hole satellites correspond to recombination where the acceptor is left in a 2S or higher

excited state. The two-hole transitions are always much weaker than the principal BE line, since the holes in the BE have much greater overlap with the acceptor ground-state wave function than with the excited states. This is also true for the higher excited state two-hole transition (eg. n = 3S) compared with the lower excited states (eg. n = 2S). For the (C^o,X), the intensity ratio of the 3S/2S transitions is consistent with Carbon being a point defect.[3.4,3.5] However, this ratio was found to vary for the KP series. This difference can probably be explained by the fact that the binding centers responsible for the KP lines are axial defects extending over more than one lattice site in contradiction to the Carbon center.

Figure 3.12 summarizes these results, with the luminescence energy of the satellites being plotted as a function of the pump energy. Note that all the experimental points are included on this figure. The TO and LO Raman lines occur at a constant separation of 33.8 and 36.8 meV from the laser line. The 5 lines at the top of the figures labeled $2P_{3/2}$, $2S_{3/2}$, $2P_{5/2}(\Gamma_8)$, $2P_{5/2}(\Gamma_7)$ and $3S_{3/2}$ can be ascribed to selectively excited pair luminescence (SPL) of Carbon acceptor-donor pairs. This SPL process consists of exciting an electron on a donor and a hole on an acceptor, with the hole in an excited state. The holes very quickly relax to the ground state, then recombine with the electron. The energy difference between the laser and the emitted light is approximately given by $\Delta E = E_A - E_A*$.[3.32] The assignment of these transitions to SPL is verified by the constant energy separation with respect to the laser line and also their transient behaviour, which is much slower than the features associated with the exciton lines. Many of the 2S and 3S DIBE two-hole transitions were observed to be split

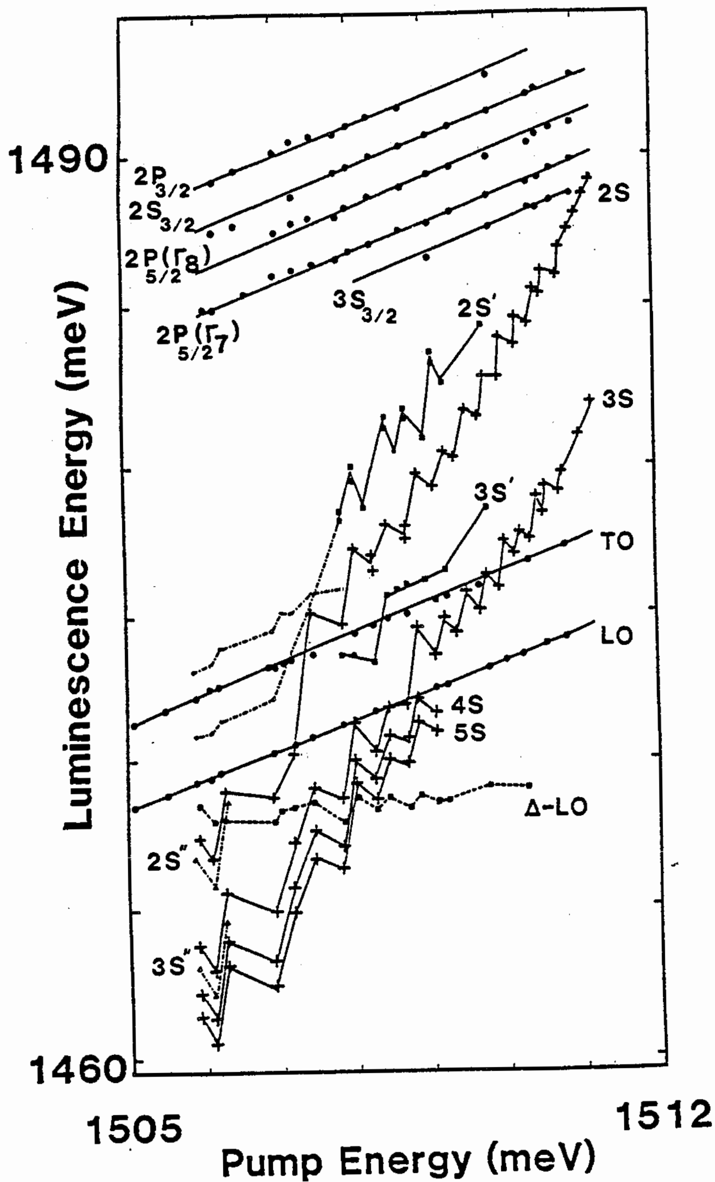

FIG. 3.12 Summary of the resonant PL measurements in the two-hole replica region. The 5 straight lines at the top of the figure correspond to selectively excited Carbon acceptor-donor pair luminescence. The TO and LO are the phonon Raman lines, which follow the energy of the pump laser. The series 2S, 3S, 4S and 5S are identified as the resonantly excited two-hole satellite of the various defect BE. Δ-LO is the LO replica of the selectively excited Δ-transition.

into doublets (eg: 2S-2S'), as can also be seen in some of the Fig. 3.10 and 3.11 spectra, but no pattern could be ascertained with regard to the magnitude of this splitting. One should keep in mind, however, the hole-hole interaction originating from the two acceptor model of Eaves *et al.*[3.15] and the different p-excited states of the acceptors as being responsible for this emission. Finally, when the laser was tuned to energy lower than line 8, no structure beside the LO and TO Raman lines was observed. This confirms that the broad feature underlying lines 1-4 observed in PL arises from a final state splitting in the PL experiment. This was also confirmed by means of photoluminescence excitation spectra.

From the observed 1S-2S energy separation, the binding energies of the different acceptors responsible for the KP lines can be estimated. However, it is expected that the central cell effects observed in the higher excited S states would become negligibly small as the higher quantum number states are reached. The central cell effect should fall off as $(1/n)^3$ where n is the principal quantum number. For $n = 3$ and $n = 4$ S-states, the central cell effects should not be detectable. The binding energy of the different centres was calculated by plotting the energy *vs* $1/n^2$ for different lines of the KP series where excited states up to $n = 5$ were observed. Carbon and Zinc acceptors were also included in the analysis. From such a plot, the ionization energy of the different impurities was extrapolated. As mentioned earlier, the central cell shifts should not be detectable for high excited states and this was indeed observed by a constant energy separation between the different excited states (E_n) and the extrapolated ionization energy (E_{ION}) for the different binding centres. The following results were

obtained by averaging over nine acceptors:

$$E_{3S} - E_{ION} = 3.7 \pm 0.2 \text{ meV}$$

$$E_{4S} - E_{ION} = 2.1 \pm 0.1 \text{ meV}$$

$$E_{5S} - E_{ION} = 1.30 \pm 0.07 \text{ meV}$$

These extrapolated excited state binding energies agree well with EM calculations, which give binding energies of 3.5, 2.0 and 1.3 meV for 3S, 4S and 5S, respectively.(1.16) The binding energies given in Table 3.3 were calculated using the following expression:

$$E_A = E_{1S-3S}^{obs} + 3.7 \text{ meV}$$

where E_{1S-3S}^{obs} is the observed 1S-3S energy separation. The results are presented in Table 3.3 for some of the lines.

TABLE 3.3 Binding Energies of the KP Lines

Line Number	Line Energy ±0.05 (meV)	1S-3S Satellite Energy ±0.1 (meV)	Acceptor Binding Energy ±0.3 (meV)
45	1510.78	31.0	34.7
42	1510.51	32.1	35.8
37	1510.18	32.9	36.5
35	1510.00	32.5	36.2
32	1507.73	34.6	38.2
28	1509.22	34.3	38.0
27	1509.08	35.4	39.0
25	1508.72	36.6	40.3
22	1508.27	38.0	41.6
19	1507.84	39.0	42.7
17	1507.45	38.3	41.9
16	1507.15	39.9	43.5
14	1506.92	42.0	45.7
10	1506.26	40.7	44.4
9	1506.12	43.2	46.9
8	1505.93	42.1	45.8

There exists an empirical relationship between the exciton localization energy E_{BX} and the impurity binding energy E_A known as Haynes' rule.[3.33] The exciton localization energy is the energy difference between the free exciton and the bound exciton energy. Such dependence has already been observed by Skolnick *et al.*[3.27] for only five acceptors of the KP series, all at the high energy end of the spectrum (lines 32-42). Figure 3.13 shows the relation of E_{BX} on E_A for more than 30 lines belonging to the KP spectrum. A linear variation of the exciton binding energy with increasing acceptor binding energy is found and a value for $\Delta E_{BX}/\Delta E_A$ of 0.40±0.02 is obtained. This linear dependence likely results from the close similarity within this family of defect acceptors.

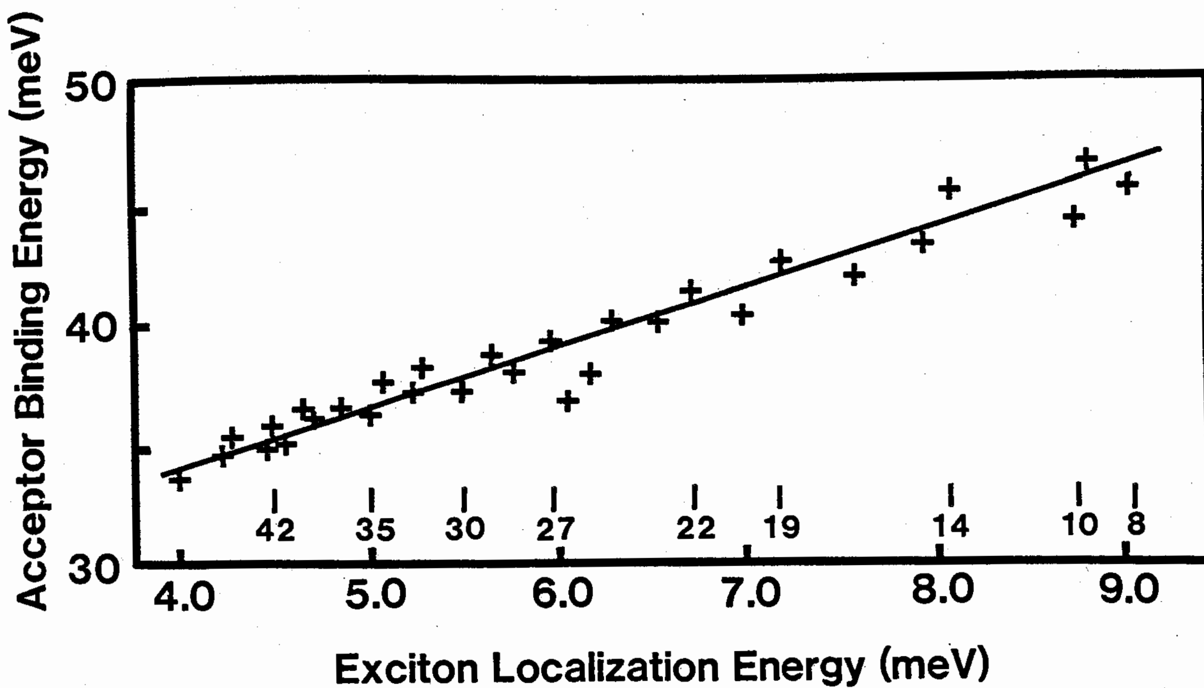

FIG. 3.13 A comparison of the BE localization energy for the KP lines (numbered at the bottom) *vs* the acceptor binding energies as determined from the 3S two-hole replicas.

The accurate defect acceptor binding energies determined here can also be used to conclusively demonstrate that the d_n lines originate from the same family of acceptor defects as the KP lines. Skromme and co-workers[3.26] used temperature and excitation intensity-dependent PL measurements to demonstrate that these low energy d_n lines are DAP and free-to-bound in nature, involving normal shallow donors and at least four different acceptor levels. Here, time-resolved spectroscopy was used to discriminate between the two different kinds of radiative processes. The decay time of the free-to-bound transition is known to be much faster than the DAP emission,[3.34] so by setting different collection time windows, it was possible to discriminate the longer-lived DAP from the shorter-lived (e,A^o) transitions. In Figure 3.14(a), a typical d_n spectrum is shown along with the higher-lying Carbon free-to-bound (e,C^o) and DAP (D^o,C^o) transitions. In Figure 3.14(b), the faster free-to-bound transitions are enhanced by using a short time window, while in (c) the longer-lived DAP transitions are enhanced with a delayed time window. In Figure 3.14(a) and (c), the d_n PL is simulated by convolving the observed Carbon-related PL with the distribution of defect acceptor binding energies and concentrations as determined from the KP line spectroscopy. This fit, which involves no adjustable parameters, is seen to be in excellent agreement with the observed d_n spectra in both cases, proving that indeed the series of peaks at 1470-1485 meV can be correlated with the KP lines, both involving the same acceptor defects.

Excitation spectra of the V-band underlying lines 1-4 were first reported by Beye and co-workers.[3.23] They observed a major energy transfer process from the upper exciton series to the V-band. They also

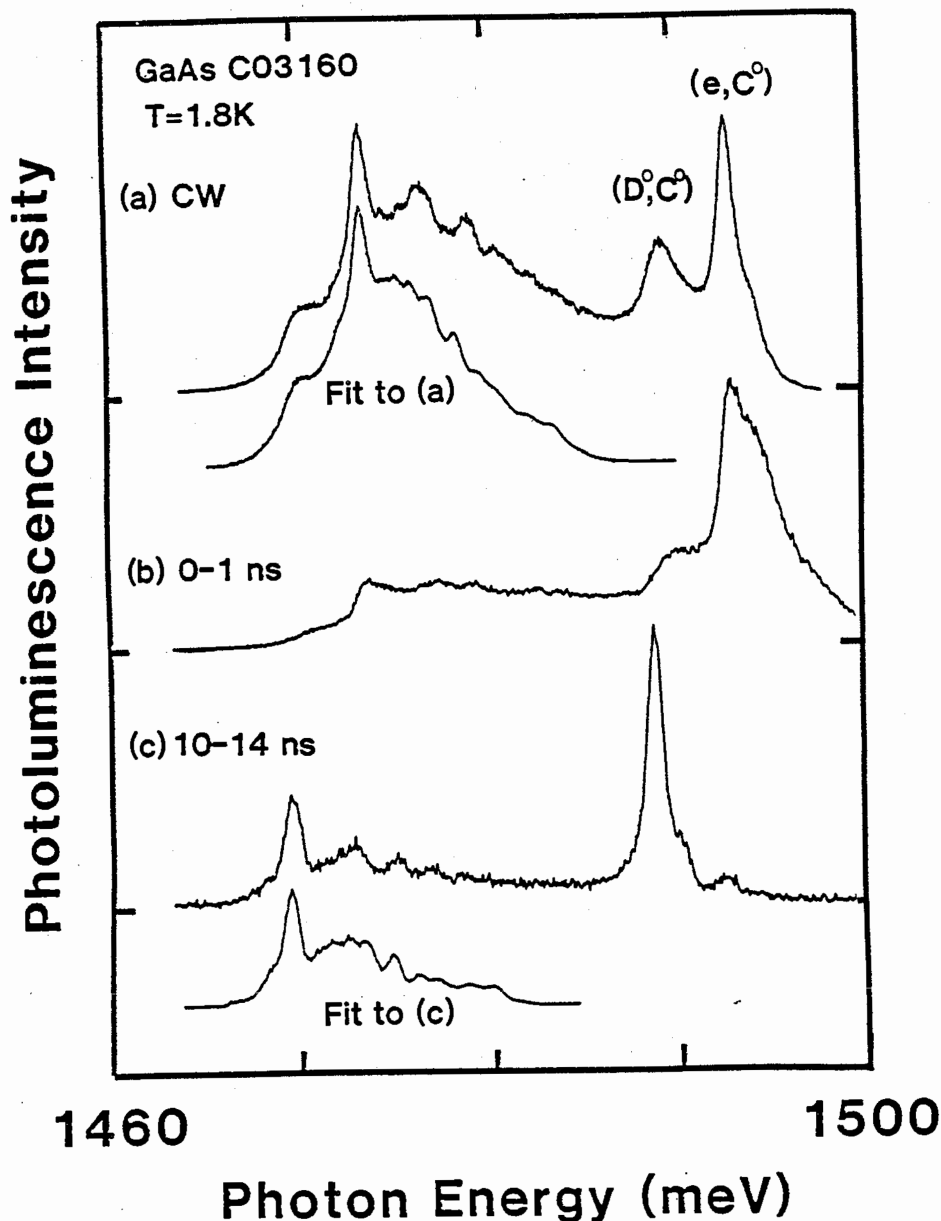

FIG. 3.14 (a) shows a typical PL spectrum for CW above-band gap pumping, revealing the d_n lines lying below the Carbon donor-acceptor (D^o,C^o) and free-to-bound (e,C^o) bands. The fast (e,A^o) processes are enhanced in (b) by using pulsed excitation together with a short time window immediately following excitation, while in (c) the long-lived (D^o,A^o) lines are enhanced by using a delayed time window. The d_n spectra in (a) and (c) are seen to be in excellent agreement with simulated spectra (involving no adjustable parameters) generated by convolving the observed Carbon spectrum with the distribution of defect acceptors as determined from the KP line spectroscopy.

reported that there was no energy transfer between the states which compose the V-group. As mentioned previously, the complete absence in PLE of the broad feature underlying lines 1-4 observed in the two-hole replica energy region is believed to indicate that this region could be strictly due to replicas of the higher-lying KP lines resulting from a ground state splitting of the defect acceptor. By selectively exciting the 8-45 KP lines, Δ replicas of many of these lines were observed, some of which are shown in Fig. 3.15(c-e). Most of these broad Δ replicas were detected in the V-band region of 1505 meV and also weaker emission were noticed at higher energies. Strong phonon-induced relaxation from the excited states to the ground states could be at the origin of this broadening. Curve (b) of Fig. 3.15 is the sum of these discrete Δ replicas obtained from selective excitation of the higher KP lines, which is indeed seen to be in excellent agreement with the shape of the Δ PL band (lines 1-4) observed in the non-selective PL spectrum. Furthermore, a small part of the background underlying lines 8-10 also takes its origin from the higher-lying KP lines. Finally, each of these broad satellites coupled very strongly to optical phonons and were always observed in the resonant excitation spectra (Δ_{LO} in Figures 3.10, 3.11, 3.12). Figure 3.16 shows the variation of this acceptor ground state splitting E_{Δ} for the different lines of the spectrum. On the same energy scale, the binding energy of each individual acceptor is represented. Surprisingly, the ground state splitting is seen to decrease with increasing total binding energy. In the model of excitons bound to acceptor pairs of varying separation, first proposed by Eaves[3.15] and later modified by Skolnick,[3.27] to explain the polarization dependence of the components, the final state splitting

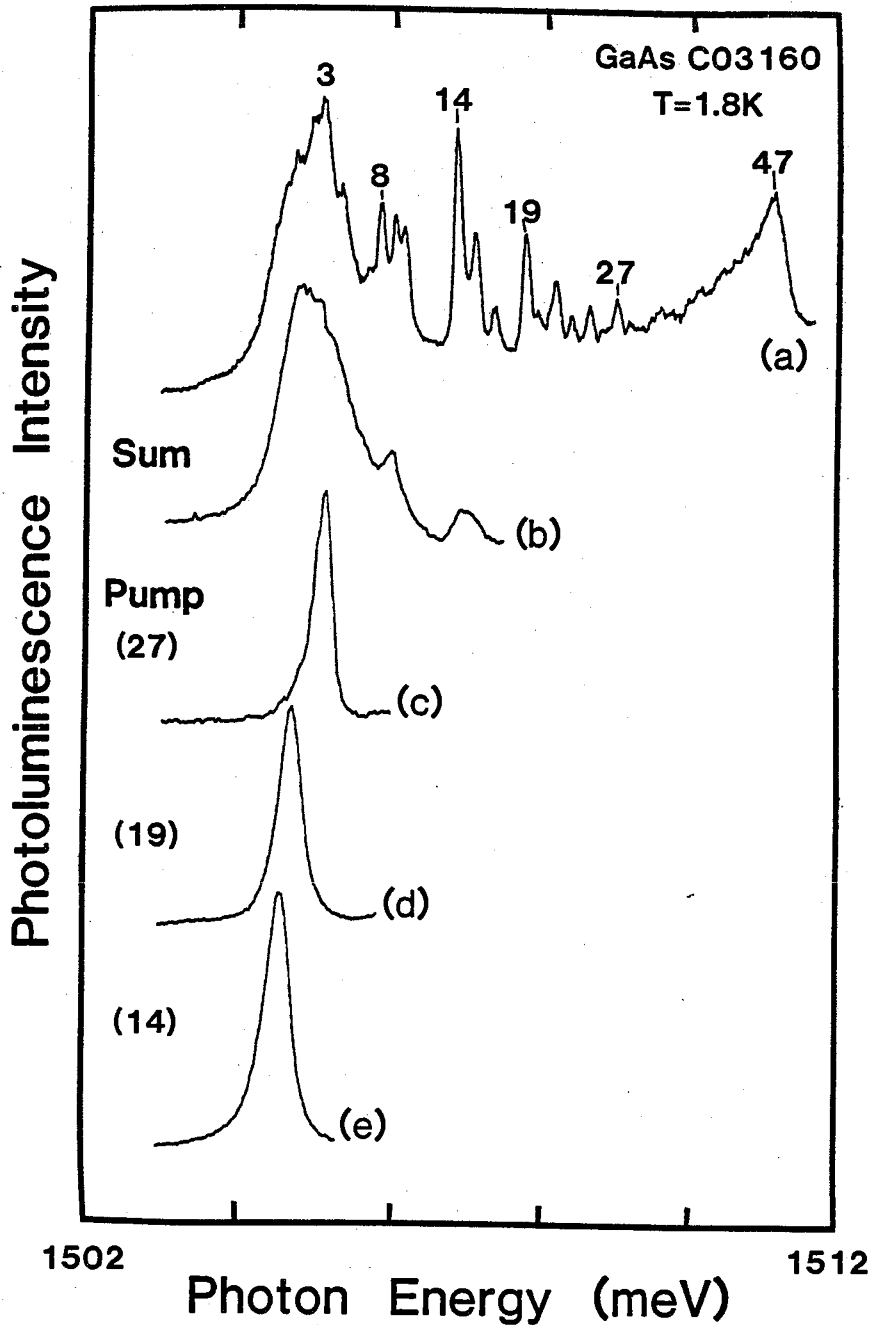

FIG. 3.15 (a) shows a nonresonantly excited KP line spectrum, while (c)-(e) show typical Δ replicas obtained by resonantly exciting lines 27, 19 and 14. In (b) the sum of all the selectively excited Δ replicas is seen to match the observed PL in the 1-4 region quite well.

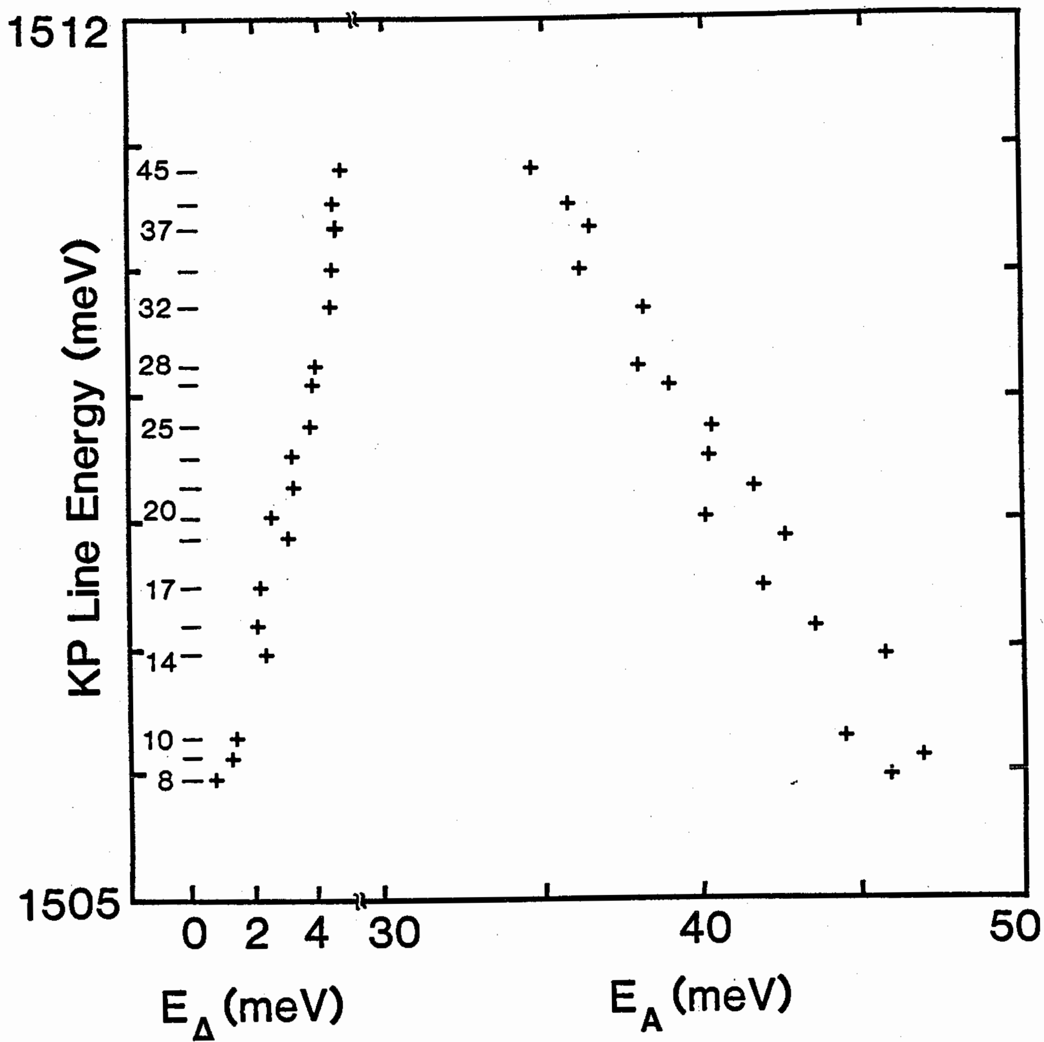

FIG. 3.16 The defect acceptor binding energy E_A and ground state splitting E_Δ are plotted *vs* KP line energy.

corresponds to the excited state of the axial acceptor pair. For such a model to be valid, one would expect to see an increase in the final state splitting for decreasing separation, but the opposite effect was observed. Furthermore, in their model, the sharp lines below 14 (i.e. 8-9-10) remained unexplained. Our resonant excitation spectra (Fig. 3.11), however, showed that these lines were in fact of the same origin as the other high energy lines of the spectrum, i.e. were acceptor-like bound excitons.

Finally, individual lifetime measurements of the resonantly excited two-hole 2S transitions were measured for some of the KP lines. Four of these decay curves are represented in Figure 3.17. The exponential decays vary from 1.3 ns for the high energy line 27 to 1.8 ns for the lower line 8. Figure 3.17 is to be compared with Figure 3.6, where the decay curves of the individual lines are shown for nonresonant excitation conditions. One major difference exists between the two sets of data: the long-lived component observed for the low energy lines of the KP series under nonresonant excitation condition is absent in its 2S replica. Thus, the lifetimes obtained from the 2S two-hole transitions are the true radiative lifetimes of the bound excitons, independent of the capture time required for the exciton to get trapped by the binding centres, or the relaxation from higher-lying BE excited states. The lifetimes of the 2S two-hole transitions were found to increase in going from line 27 to 8, as expected from the general considerations of lifetime versus binding energy (localization energy) of the BE discussed in Chapter 1.

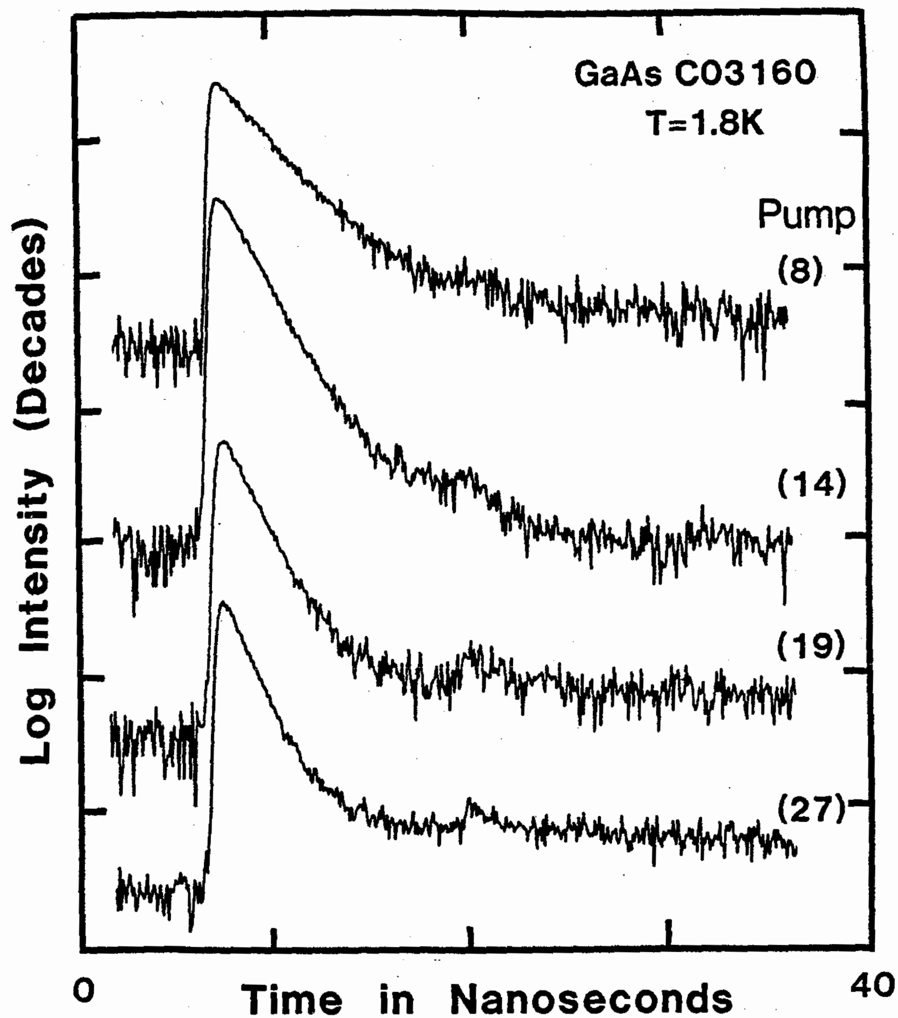

FIG. 3.17 Luminescence decay measurement of the 2S two-hole excited states of lines 8, 14, 19 and 27. Experimental lifetimes of 1.8, 1.6, 1.4 and 1.3 ns (±0.1 ns) were obtained for the various lines. No *long-lived* component was detected in this emission.

In spite of these experiments, no direct information on the total number of electronic particles in the initial and final states in the KP transitions is available. Such information is necessary in order to formulate a reliable model for the recombination processes involved. Zeeman spectroscopy is a direct method to study the electronic nature of the states involved in the transitions, and is the subject of the next section.

3.7 Zeeman Spectroscopy

Bound excitons involving holes from a degenerate valence band edge can have considerable degeneracy. By studying the way in which these degeneracies are split with external fields, much useful information about the electronic structure of the BE levels can be obtained.

In the present study, Zeeman spectra were acquired for both $\vec{E} \parallel [\bar{1}10]$ and $\vec{E} \parallel [110]$ polarizations. The clearest results were observed for $\vec{E} \parallel [\bar{1}10]$, the polarization of the strong, sharp KP lines, as reported in section 3.3 (Figure 3.2). The polarization direction $\vec{E} \parallel [110]$ was much more difficult to analyze, mainly due to problems of weak luminescence signals and the overlapping of the spectral features from different centres. Results were analyzed for most of the lines in the range 14 to 32, beyond which the lines became too weak for detailed study. Because of the proximity of the lines and their similar relative intensities, lines 8 to 10 could not be studied and the lines to lower energies (1-4) were too broad to obtain any useful information.

Zeeman measurements were carried out in a custom-built split-pair superconducting magnet cryostat, where fields of up to 8 Tesla could be

reached. The sample, immersed in either liquid helium at 4.2 K or superfluid helium, was excited with ~20 mW of tunable CW radiation from a pumped dye laser. The excitation was usually tuned to be in resonance with either the free exciton energy or the band gap energy. The PLE spectra were taken with the use of a computer controlled stepping motor to tune a birefringent filter located in the dye laser cavity. The linewidth of the dye laser was 0.03 meV (FWHM) and the resolution of the PLE spectra was determined by this and the minimum step interval of 0.02 meV. Luminescence was observed along a direction perpendicular to the magnetic field (H) in all cases and was dispersed by either a 5 meter spectrometer and detected by an imaging PM tube, or by a double 3/4 meter spectrometer using the VPM-159A3 PM tube as detector. For observations of the luminescence perpendicular to the magnetic field, the luminescence could be either unpolarized or linearly polarized parallel or perpendicular to the field. The luminescence polarized with $\vec{E} \parallel [\bar{1}10]$ will be referred to as σ polarized and the luminescence polarized with $\vec{E} \parallel [110]$ will be referred to as π polarized. By using appropriate light polarizing elements, such as a quartz half-wave plate and linear polarizers, the various polarizations of the laser and the luminescence could be selected. Angular Zeeman measurements were obtained by mounting the sample on a rotating holder which could be rotated from outside by a simple gear arrangement. The sample was mounted with a [001] axis parallel to the rotation axis and to the observation axis. This geometry assured that the principal crystal axis, [110] and $[\bar{1}10]$, could be aligned parallel to the field.

Figure 3.18 shows representative PL spectra taken with the magnetic field $\vec{H} \parallel [\bar{1}10]$ under two polarizations. All the sharp lines (from

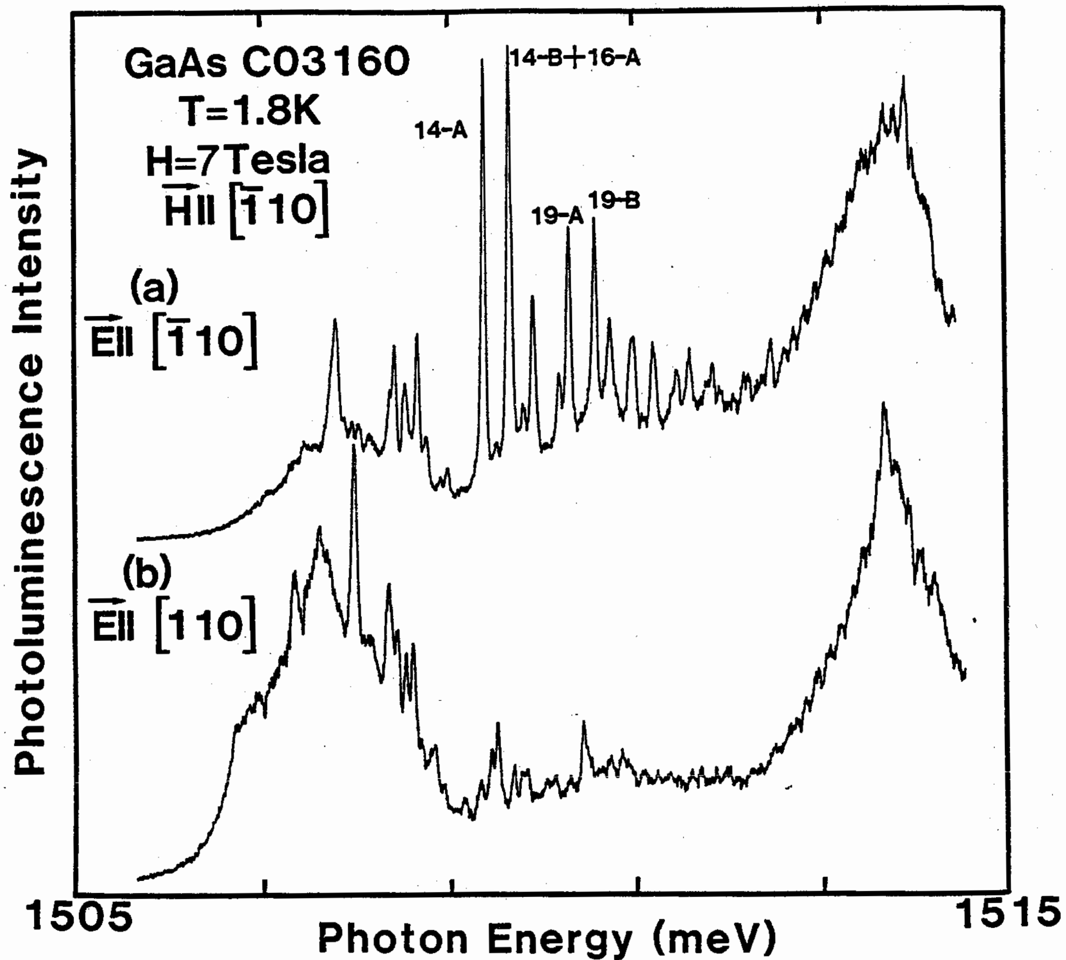

FIG. 3.18 A representative nonselective excitation Zeeman PL spectrum. The principal KP lines show a doublet (A-B) splitting, two of which have been labeled. Curves (a) and (b) represent two polarization directions.

14-32) revealed primarily doublet splittings which were found to vary linearly with magnetic field up to 7 Tesla. Also, a strong diamagnetic shift to higher energy was observed. Figure 3.19 represents the splitting of the doublets of line 14 as a function of field for $\vec{H} \parallel [110]$ and $\vec{H} \parallel [\bar{1}10]$. Note that a constant shift to higher energy has been subtracted from the lines such that the *centre of gravity* of the doublet remained constant. This shift to higher energy was 3.1 meV at 8 Tesla and is close to that expected for shallow donor electrons in GaAs. Schairer *et al.*[3.35] reported a shift of 2.8 meV at 8 Tesla for excitons bound to the deep Sn acceptor in GaAs. These Sn BE's (Sn^{o},X) were shown to obey a *pseudodonor* model in which two tightly bound holes and a weakly bound electron in a Coulomb potential formed the initial state. Thus, the similarity in the diamagnetic shift observed for the KP lines and the (Sn^{o},X) suggest that there is a weakly bound electron in the initial state of the luminescence transition. As seen in Figure 3.19, the Zeeman splittings are strongly anisotropic, with maximum splitting being found for $\vec{H} \parallel [110]$.

So far, no evidence has been presented as to whether the doublet splittings arise in the initial or final state of the PL transitions, or in a combination of the two. PL and PLE measurements were performed for various orientations as a function of magnetic field and temperature in order to resolve this question. A very careful search for thermalization in both PL and PLE verified that, while the BE ground states (initial state in PL) were magnetically split, the acceptor ground states (final state in PL) involved in the main KP transitions were not, implying $J = 0$ for the acceptor ground state. This conclusion

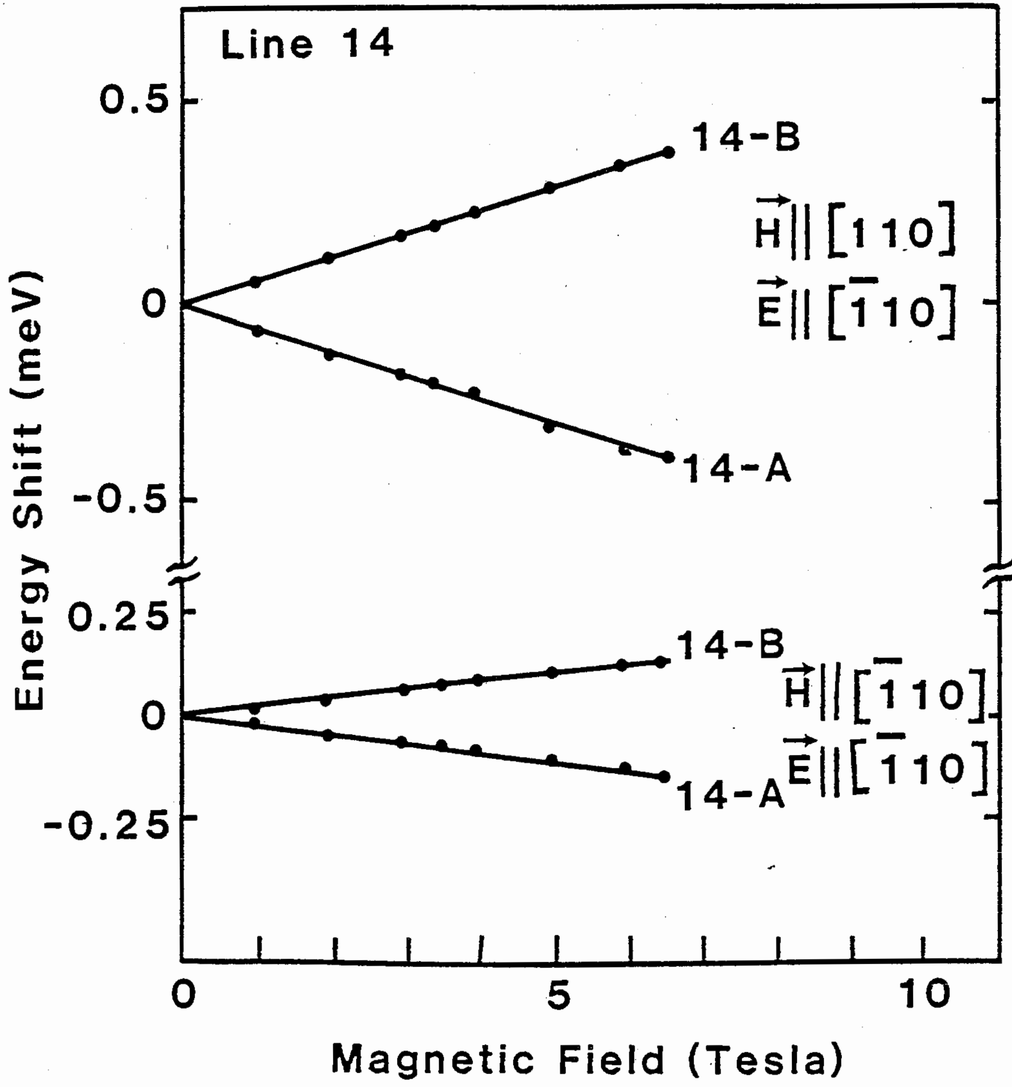

FIG. 3.19 Zeeman splitting pattern of line 14 for $\vec{H} \parallel [110]$ and $\vec{H} \parallel [\bar{1}10]$ for the $\vec{E} \parallel [\bar{1}10]$ polarization. The strong diamagnetic shift has been subtracted from the line. Each line of the KP series is found to split into a doublet.

was reached from the observation of strong thermalization between the doublet components in PL as the field was increased, whereas in PLE, observation of the same transitions showed very little change in the relative intensities of the components with magnetic field or even temperature. We can conclude with confidence that the doublet splittings occur in the initial state of the PL transition.

3.8 Model for the Transitions

In the formulation of the model to explain the origin of the KP series, one has to take into consideration four important electronic properties as obtained from the resonant excitation experiments (section 3.6) and the Zeeman spectroscopy results (section 3.7):

i) The observation of *two-hole* satellites of the lines which implies that there is at least one hole in the final state of the transitions;

ii) The final state of the PL transition has a total angular momentum of zero;

iii) The observation of a strong diamagnetic shift suggests that there is a weakly bound electron in the initial state of the transition;

iv) The observation of a final state splitting of the acceptor ground-state as observed from the resonant Δ-band luminescence.

It is clear that an exciton bound to a neutral single donor or acceptor can be excluded since there would be an unpaired spin in the final state of the PL transition, giving rise to a Zeeman splitting. The DAP model of Reynolds[3.14] cannot explain the observation of

two-hole satellites. The only models which explain all four properties described above is that of the exciton bound to neutral acceptor pairs originally proposed by Eaves *et al.*,[3.15,3.16] or a double-acceptor-isoelectronic centre pair proposed by Skolnick.[3.28] In both models, the final state of the PL transition has two holes, as is needed to explain the observed two-hole transition and the $J = 0$ final state. Furthermore, the low symmetry of the defects involved here could account for the strong polarization effect observed. (Say, for example, that the two acceptors involved in the model are preferentially aligned along the [110] direction, one would then expect strong polarization of the luminescence along [$\bar{1}$10].) In both models, the initial state of the PL transition is composed of three holes and one electron, and the final state of two holes. The $J = 3/2$ degneracy of the valence band will be lifted into $m_j = \pm\frac{3}{2}$, $\pm\frac{1}{2}$ states in the low symmetry field of the centre. In order to explain the polarization of the KP series along [$\bar{1}$10] and the fact that each individual line splits into a doublet under magnetic field, it is required that the local strain of the centres be compressive with the $m_j = \pm\frac{1}{2}$ states lying to lower hole energy.[3.28] Thus, the final state of the neutral acceptor pair has two holes with $m_j = \pm\frac{1}{2}$, which combine to produce a $J = 0$ level. In the initial BE state, two of the three holes pair off into the $m_j = \pm\frac{1}{2}$ shell, leaving the third hole in an $m_j = \pm\frac{3}{2}$ state, and one electron. The resulting energy level diagram is shown in Figure 3.20(a). The only allowed transition from the $m_j = \pm\frac{3}{2}$ (hole), $m_j = \pm\frac{1}{2}$ (electron) initial state is the σ polarized ($\Delta m_j = \pm 1$), while the $\Delta m_j = \pm 2$ transition are forbidden. This is in agreement with the earlier deduction of section 3.3, that σ oscillators, observed in a

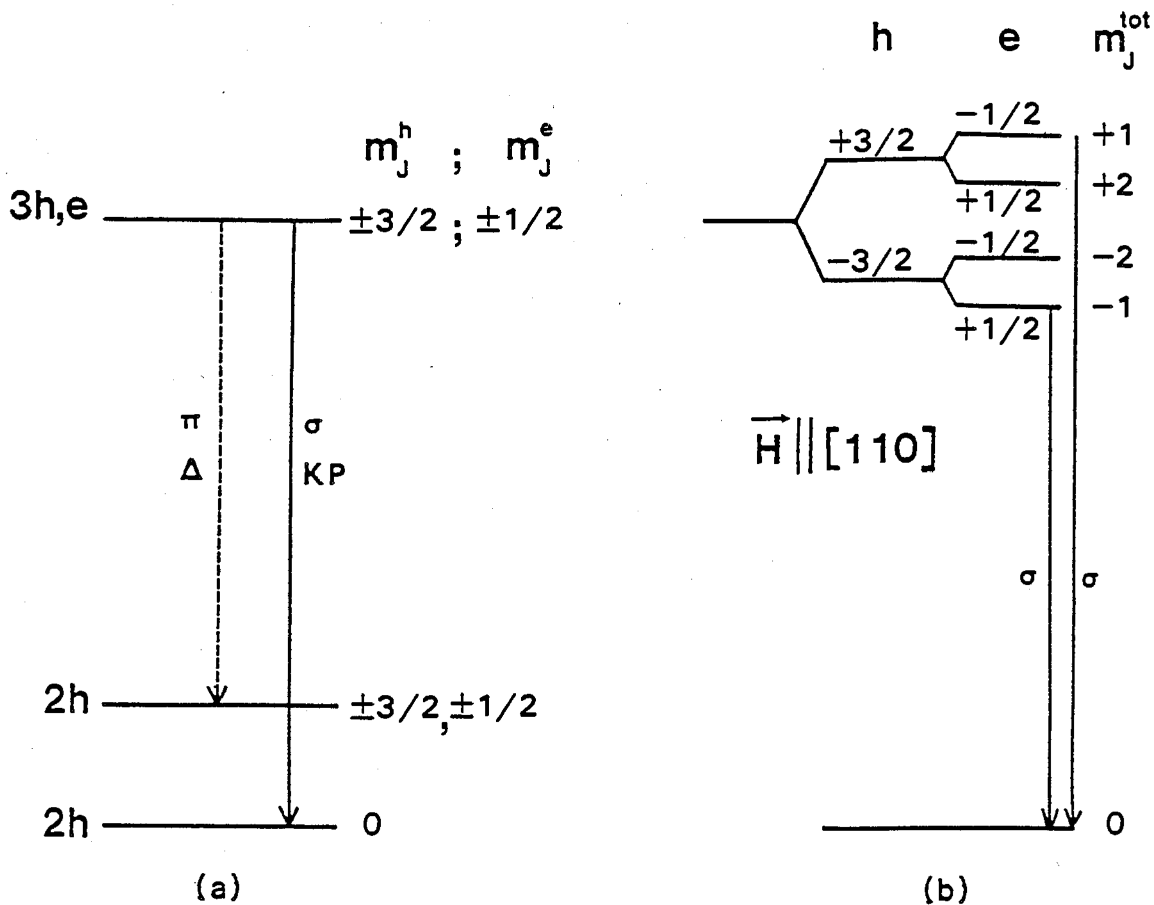

FIG. 3.20 Energy level diagram for individual centres of the KP series at zero and finite magnetic field $\vec{H}$ || [110] in (a) and (b). The initial state of the transition (an exciton bound to a single acceptor pair, or a double-acceptor-isoelectronic centre pair) contains three holes and one electron, and the final state contains two holes. The J = 3/2 valence band degeneracy is lifted in the compressive axial field, such that the $m_J = \pm 1/2$ state be to lower hole energy. In the initial state, the first two holes pair off with $m_J = \pm 1/2$, leaving a $m_J = \pm 3/2$ hole and a $m_J = \pm 1/2$ electron, which split in magnetic field according to (b). The ground state of the final state (double acceptor) contains two $m_J = \pm 1/2$ holes with a toal $m_J = 0$. The KP transition from the exciton ground state to the acceptor ground state is σ polarized. The final state splitting in (a) is the local crystal field valence band splitting. The transition labeled Δ is predominantly π polarized and gives rise to the Δ-band underlying lines 1-4. Curve (b) represents the splitting of the intial state of the PL transition for a magnetic field $\vec{H}$ || [110]. The two allowed transitions which lead to the observed doublet splitting for $\vec{E}$ || [$\bar{1}$10] are indicated.

direction transverse to [110], and so polarized $\vec{E} \parallel [\bar{1}10]$ give rise to the sharp KP lines.

The ground state splitting of the acceptor (Δ-band), as referred to in section 3.6, can be explained from the excited level in the ground state of the acceptor corresponding to the promotion of one of the $m_j = \pm \frac{1}{2}$ holes to a $m_j = \pm \frac{3}{2}$ state. The PL transition to such an excited state, labeled Δ and represented by the dashed line on Figure 3.20(a), will be π to σ polarized in the ratio 4 to 1.[3.5] This was observed experimentally from the polarization dependence of the Δ-band underlying lines 1-4 which was found to be polarized with $\vec{E}$ parallel to [110], as opposed to $[\bar{1}10]$ for the sharp BE line, which are pure σ transitions. The expected splitting in magnetic field is shown in Figure 3.20(b) for $\vec{H} \parallel [110]$. From the observation of the large diamagnetic shifts, attributed to a weakly bound electron, the electron g-value is taken as -0.46.[3.35] There are only two allowed transitions in magnetic field for the KP series corresponding to $\Delta m_j = \pm 1$ (σ polarized transition), in agreement with the observed doublet splitting. Taking the hole g-value as positive, the two allowed σ transitions are separated by $3g_h + |g_e|$, and hole g-values of 0.08±0.01 and 0.48±0.03 were obtained (for line 14) for $\vec{H} \parallel [\bar{1}10]$ and $\vec{H} \parallel [110]$ respectively. The g-values for some of the higher energy lines (15-32) were also calculated and found to be similar to line 14.

In an effort to verify the proposed models, the Zeeman splittings of the resonantly excited Δ-line replicas were studied. This was achieved by resonantly exciting each of the components of the principal doublet and looking in the Δ-band region. The two field directions $\vec{H} \parallel [110]$ and $\vec{H} \parallel [\bar{1}10]$ were again analyzed and various field strengths

used. Figure 3.21 shows the data obtained for resonant excitation of lines 14-A and 14-B for both polarizations ($\vec{E} \parallel [110]$ and $\vec{E} \parallel [\bar{1}10]$) in a magnetic field of 6.9 Tesla oriented along [110]. From the energies and polarizations of the Δ replicas, an energy level diagram was constructed and is represented in Figure 3.22. In this representation, σ transitions represent photons emitted with $\vec{E}$ parallel to $[\bar{1}10]$ ($\Delta m_j = \pm 1$) while π transitions correspond to photons emitted with $\vec{E}$ parallel to [110] ($\Delta m_j = 0$). As discussed previously, the final state of the Δ transition consists of two holes, one having $m_j = \pm \frac{3}{2}$ and the other having $m_j = \pm \frac{1}{2}$, where the energy levels were found to split under field according to Figure 3.22. From this splitting, new g-values are calculated for the 1/2-hole and the 3/2-hole and are compared in Table 3.4 to the previous g-values obtained from the main KP transition. The similarity of the hole $g_{3/2}$-values obtained from the two different KP and Δ splittings is worth mentioning, as it provides clear evidence of the validity of the models. Furthermore, the low symmetry of the defect responsible for this series of lines must be the origin of the large anisotropy observed for the Zeeman splittings. This would explain the large differences in the g-values along the [110] and $[\bar{1}10]$ directions.

FIG. 3.21 Δ-replicas obtained by resonantly exciting the doublet 14-A and 14-B for a field of 6.9 Tesla oriented along [110]. The two polarization $\vec{E} \parallel [110]$ and $\vec{E} \parallel [\bar{1}10]$ are indicated.

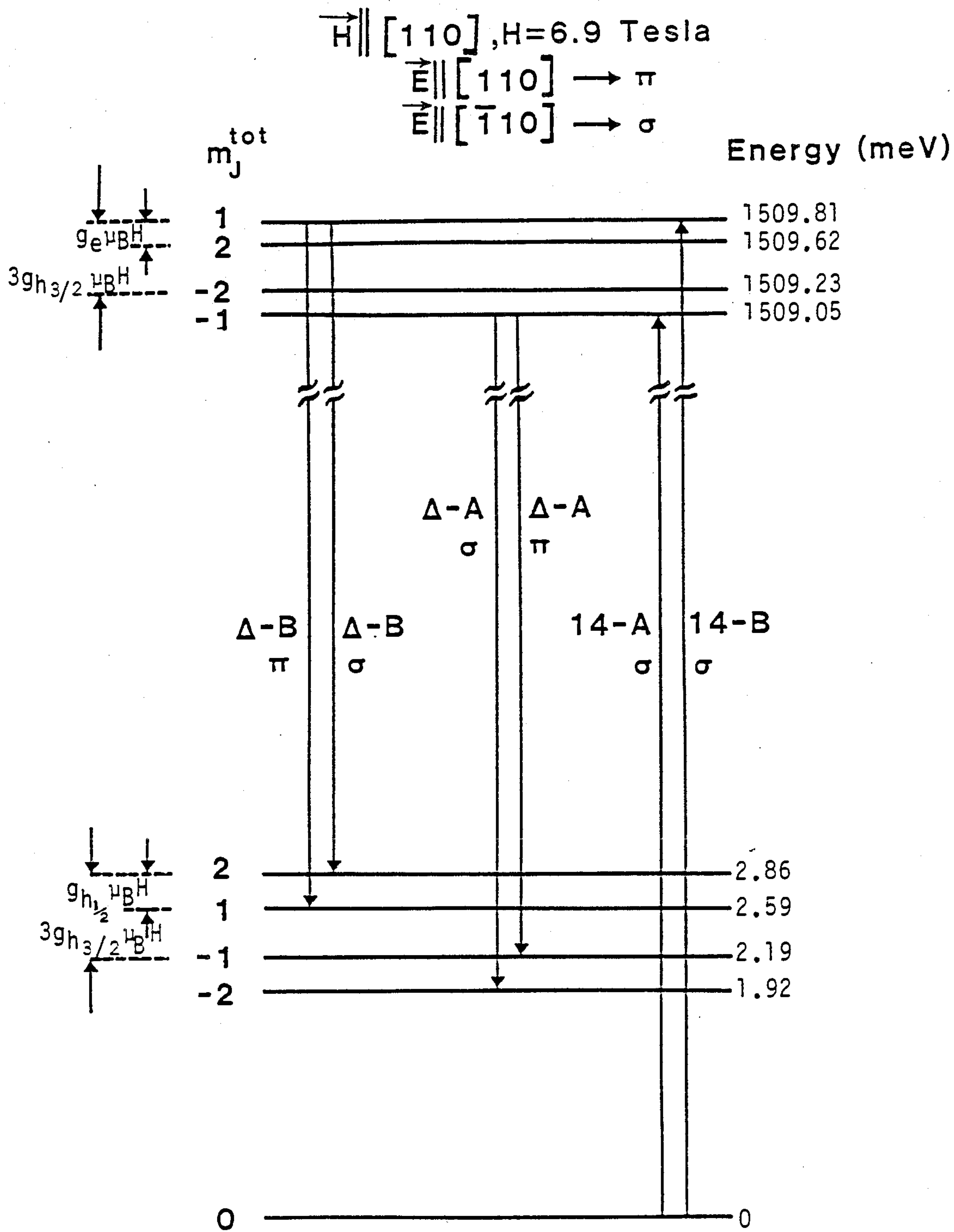

FIG. 3.22 Energy level scheme for the resonant excitation of line 14 (A and B) at a field of 6.9 Tesla oriented along [110]. The lines 14-A and 14-B were resonantly excited and the luminescence detected in the Δ-band region for the two σ and π polarizations. The energies of the transitions are indicated on the right and the splitting of the various levels is as shown on the left-hand side.

TABLE 3.4 Hole g-values for Line 14*

$\vec{H} \parallel [\bar{1}10]$		$\vec{H} \parallel [110]$	
KP:	$g_{3/2} = 0.08 \pm 0.01$**	KP:	$g_{3/2} = 0.48 \pm 0.03$
Δ:	$g_{3/2} = 0.09 \pm 0.05$	Δ:	$g_{3/2} = 0.56 \pm 0.05$
	$g_{1/2} = 1.67 \pm 0.04$		$g_{1/2} = 0.68 \pm 0.20$

*Calculation made with $g_e = -0.46$.[3.35]

**The uncertainty in the g-values has been estimated over all the different magnetic fields studied.

3.9 Conclusion

Low-temperature PL, PLE transient measurements and Zeeman spectroscopy have been performed on a very high quality MBE grown GaAs layer. It is believed that the results obtained represent significant progress in the understanding of the centres responsible for the defect BE emissions. The following important observations were made in the course of this study. The highest energy line 47, found to have a different origin than the sharp KP lines, was confirmed to be due to the recombination of excitons on neutral acceptors. The measured radiative decay times of the KP series is fully consistent with them being excitonic in origin. From the resonant excitation data, the low energy

satellites of the BE lines have been attributed to two-hole transitions. Excited states up to n = 5 were observed and permitted the calculation of the acceptor binding energies. Evidence was presented supporting the existence of correlations between the 1504-1511 meV and 1470-1490 meV sets of peaks, and leads to the conclusion that the defect BE lines arise from recombination of excitons at a series of neutral acceptors while the 1470-1490 peaks involve free-to-bound and DAP transitions of the same series of acceptors. The latent anisotropy reflected by the polarization of the lines supports the fact that these groups are due to exciton recombination at axially oriented complex defects preferentially aligned along [110]. The symmetry of the defects giving rise to the most prominent KP lines, and the quantum number of the initial and final states of the recombination process have been derived from Zeeman spectroscopic investigations. A model for the PL transition has been deduced which involves exciton recombination at single acceptor pairs or double-acceptor-isoelectronic pairs.

The origin of these acceptor complexes is still not yet clear. There have been two recent suggestions for the involvement of different chemical species in the KP series. Leroux and co-workers[3.36] have observed PL spectra in MBE GaAs under hydrostatic pressure which they attributed to exciton recombination at N_{As} isoelectronic centres. They suggested that the nitrogen contamination could originate from the decomposition of the BN effusion cells. If B-N molecules were also transported together, such defects would have some of the required properties of the sharp KP lines when incorporated into GaAs. For example, B_{As}-N_{As} defects have <110> symmetry,[3.36] B_{As} is a double acceptor having a binding energy of 78 meV and 203 meV in its two

ionization states.[3.37] Pairing with the N_{As} isoelectronic centre could lead to a reduction of binding energy into the 30-45 meV range of the defect acceptors. On the other hand, Makita and co-workers[3.38-3.39] ion-implanted C^+ into very pure GaAs samples and showed that the g-line, along with six other components of the KP series, was related to the introduction of C impurities alone. The other members of the KP series were not produced solely by the incorporation of the C atom, but rather by the formation of a complex between C and some other atoms, presumably oxygen, which could be introduced in the form of CO gas molecules remaining in the growth chamber. In soley O^+-implanted samples, no emission lines were formed in the KP region, but in samples which were simultaneously implanted with C^+ and O^+, a very large enhancement of KP fine structures was observed. They concluded from their ion implantation of C^+ and O^+, and the thermally unstable nature of the sharp defect-induced BE upon growth, that a complex between a C atom at a host As site and an O atom (situated not at a host As or Ga, but off-site) was at the origin of the KP series.

In spite of the new results presented here, a number of unresolved problems still remain in the analysis of these lines and further progress will likely require the conclusive identification of the chemical species involved in these complex defects.

CHAPTER 4

EXCITONS AT HIGH DENSITY

4.1 Introduction

At low temperatures, free electrons and holes, regardless of how they are created in a semiconductor, can be bound into excitons by Coulomb forces. In the limit of low nonequilibrium density, the exciton gas may be considered as a weakly interacting Boltzmann gas. Lampert[4.1] first suggested that in a nonequilibrium electron-hole gas, free multiparticle complexes more complicated than the exciton can exist, namely, neutral excitonic molecules (bound states of two excitons, often called biexcitons). The stability of such free complexes was later confirmed by reliable variational calculations.[4.2,4.3] Since the introductory work by Lampert, many attempts have been made to discover these free multiparticle complexes, in particular the biexcitons, by spectroscopic means. The progress in experimental investigation of these excitonic molecules is most evident during the last few years both in direct and indirect gap semiconductors.

In contrast to ordinary gases, the electron-hole gas in a semiconductor is in principle a nonequilibrium system due to recombination processes. For example, in direct gap semiconductors, the electron-hole recombination times are very short, usually of the order of nanoseconds. As a result, the formation and decay of complexes takes place under highly nonequilibrium conditions which means the absence of

equilibrium both with respect to lattice temperature and sometimes between electron-hole system itself. The most convincing evidence for the radiative decay of biexcitons was found in CuCl and CuBr, where, according to variational calculations, the excitonic molecules have large binding energies.[4.3] One should, however, keep in mind that compound semiconductors, in contrast to atomic semiconductors such as Si and Ge, contain relatively high concentrations of residual shallow electrically active impurity centres. At low temperatures, excitons are easily bound forming bound exciton complexes. Such BE in direct gap semiconductors typically have extremely large oscillator strengths for optical transitions and at low temperatures they provide the most effective radiative channel. Since the spectral positions of the emission lines of free and bound exciton lines are very close, it is difficult to identify free complexes, such as biexcitons, in the spectra of radiative recombination in direct gap semiconductors. Furthermore, when high densities of quasiparticles are achieved, via high power pulsed excitation, the collisions between them become numerous. The broadening of the emission line due to radiative decay of biexcitons is due to elastic collisions between excitons and biexcitons. Inelastic collisions between excitons and biexcitons, and between electrons and excitons, also become very important as radiative recombination processes of these quasiparticles at higher densities. At these concentrations, multiparticle interaction effects have also to be taken into account.

This chapter deals with the interaction between excitons at high concentration. Further details of experimental results of time-resolved

luminescence spectra of very pure ZnSe, GaAs and GaAs/$Al_xGa_{1-x}As$ quantum wells over a wide range of excitation intensities is reported.

4.2 Radiative Recombination in Highly-Excited ZnSe

Zinc selenide has long been recognized as one of the most promising II-VI semiconductors for optoelectronic device applications. In particular, as a light emitter it has several nearly optimum properties, including a direct band gap near 2.7 eV, just large enough to provide blue as well as longer wavelength recombination luminescence.[4.4-4.8] It is well known that ZnSe can be made n-type through conventional vapour transport or bulk growth and subsequent anneal in Zn-excess conditions.[4.9,4.10] However, the production of p-type ZnSe is known to be very difficult. One of the main reasons is the lack of suitably well-behaved acceptor species. Few successful techniques have been developed for growing low-resistivity p-type crystals. Very recently, such high-purity p-type ZnSe single crystals have been grown using highly purified Zinc as the starting material.[4.9,4.10]

In the present section, two new luminescence bands which appeared a few meV lower than the free exciton energy under laser excitation of moderate power in very pure single crystals at liquid helium temperature were detected. The spectral position of these new bands, their appearance under conditions of excitation favouring high exciton densities and their transient behaviour, suggest that these emission bands are due to excitonic molecules (biexcitons) and to radiative biexciton-biexciton collisions.

The single crystals used in the present work were grown by the

vapor-phase transport method, using commercial grade high-purity selenium (99.999%) and zinc purified by vacuum distillation and overlap zone-melting, at the Department of Materials Science at Tohoku University in Japan. The complete growth process has already been described in detail elsewhere.[4.9,4.11] Samples for the PL measurements were cleaved from the grown crystals and etched at 363K, using a solution consisting of 3 parts saturated aqueous solution of $K_2Cr_2O_7$ and two parts concentrated H_2SO_4.

The excitation source used in the following experiments consists of an actively mode-locked Ar-ion laser synchronously pumping a dye laser using Rh-6G dye. A cavity dumper is used to lower the pulse repetition rate and increase the peak power. The laser pulse width was ~10 ps at 590 nm with a repetition rate of 4 MHz. To create the necessary above band gap photons, a KDP frequency doubling crystal was used. The resultant 295 nm beam was then focussed onto the samples, which for these experiments, were immersed in superfluid helium at 1.8 K. The maximum average power density of excitation at the sample was ~115 mW/cm^2, corresponding to a maximum peak power density of 3 kW/cm^2. The luminescence was dispersed by means of a double 3/4 m spectrometer and detected by a Varian VPM-159A3 photomultiplier operated in the photon counting mode. The luminescence decay curves were obtained with the usual time-to-amplitude converter/pulse-height analyzer combination. The instrumental response of the system was 210±30 ps, which proved to be sufficiently fast for the present work.

In Figure 4.1, the luminescence spectra of two ZnSe crystals measured at 1.8 K under 295 nm light excitation at various intensity levels are shown. In Figures 4.1(a) and 4.1(b) the emission spectrum of

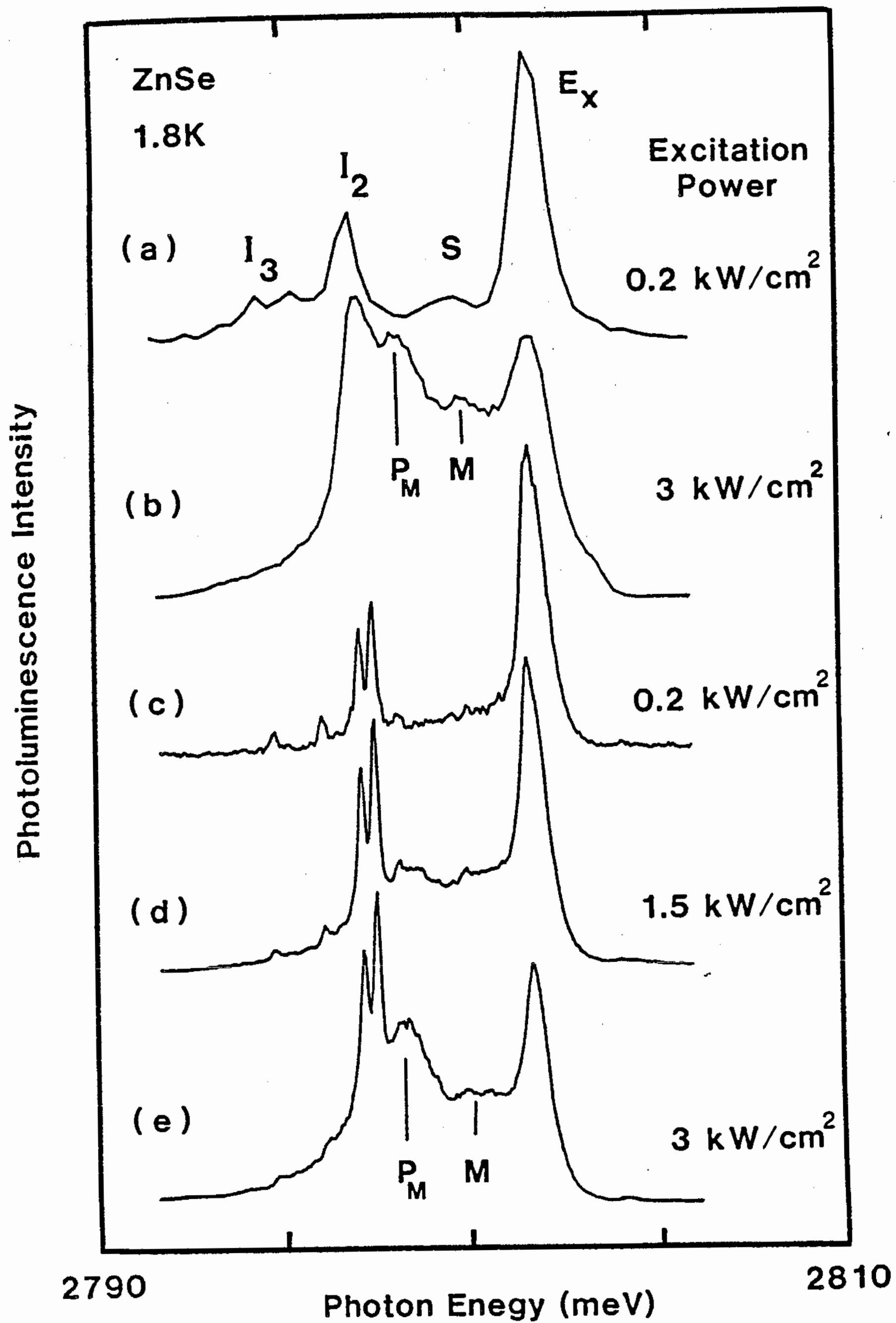

FIG. 4.1. Photoluminescence spectra taken at 1.8 K using different excitation powers. The pumping wavelength was 295 nm. Curves (a) and (b) represent the emission spectra of sample No. 1. Curves (c)-(e) are the emission spectra of sample No. 5.

sample No. 1 is compared for two excitation intensities. The free exciton emission E_x, the donor bound exciton I_2 and the ionized donor bound exciton I_3 are clearly observed. The emission band S, detected at 2800.2 meV, was previously observed by Isshiki and co-workers[4.10,4.11] and attributed to the scattering of excitons by other free particles at a structural defect with slightly lower potential for free particles and free excitons. The peak intensity of this band relative to the other emission lines was found to depend strongly on where the laser beam was hitting the crystal surface. When higher excitation intensity is used, such as in Figure 4.1(b), two new emission bands labeled M and P_M are observed at 2800 and 2798.5 meV. While the M band is indistinguishable from S on the basis of photon energy alone, further evidence will demonstrate that they are in fact due to different processes. The curves (c)-(e) show the luminescence spectra of sample No. 5 at different excitation powers. Again, the emission spectra for the low excitation power shows the same general features as sample No. 1 with the exception of the S-band, which is much weaker and appears only as a low energy shoulder of the free exciton line. Finally, at higher intensities the M and P_M emission bands appear.

Before assigning the emission peaks to different radiative processes, a short summary on high exciton density effects will be given. When the concentration of excitons becomes very high, a number of new processes can be observed; for example, biexcitons can be formed. The usual procedure for forming biexcitons consists of exciting the crystal with intense laser light, creating a very large number of hot free carriers. As shown by Toyozawa,[4.12] after thermalization, most of them combine at low temperatures to form excitons. As the

concentration of these excitons is very high, they may associate to form biexcitons. The most probable process of recombination of these excitonic molecules involves the emission of a photon $h\nu_M$ leaving a free exciton (biex)→(ex)+$h\nu_M$. The energy conservation of this decay process gives[4.13]:

$$2(E_g - E_X) - E_M + E_M^K = h\nu_M + (E_g - E_X) + E_X^K \qquad (4.1)$$

which gives,

$$h\nu_M = E_g - E_X - E_M + E_M^K - E_X^K \qquad (4.2)$$

where E_g is the energy gap, E_X the binding energy of the exciton, E_M the binding energy of the biexciton (with respect to two free excitons) and E_M^K and E_X^K are, respectively, the kinetic energies of the initial biexciton and of the resulting exciton. E_M^K can be considered as negligible at very low temperature and E_X^K should then also be small due to momentum conservation. Both terms account for the lineshape of the biexciton transition. In the absence of an experimental lineshape detailed enough to allow an accurate theoretical fit, the peak of the line is, however, obtained in first approximation by neglecting both, thus

$$h\nu_M(\max) \simeq E_g - E_X - E_M . \qquad (4.3)$$

In general, for direct band gap semiconductors, high concentrations of free carriers and excitons are created by intense laser light excitation. When such high densities of quasiparticles are achieved, the collisions between them become numerous and radiative multiple-

particle interaction effects have to be taken into account. Let us consider three of these inelastic collision mechanisms.

(a) Exciton-Exciton Collision (P)

In this process a new luminescent emission band called the P-line appears. One of the excitons scatters into an excited electronic state or dissociated state while the other scatters into a photon-like state. The energy balance for the dissociated process is[4.14]:

$$(ex) + (ex) \rightarrow e,h + h\nu_P$$

$$h\nu_P = E_g - 2E_X - E^K_{e,h} \qquad (4.4)$$

where $E^K_{e,h}$ is the kinetic energy of the unbound pair electron-hole created during the collision.

(b) Biexciton-Biexciton Collision (P_M)

This process is an inelastic collision of two excitonic molecules; one of the four excitons involved in the process is radiatively annihilated, leaving the other three as free excitons. If the different kinetic energies of the excitons is neglected, the energy balance of the process yields[3.15]:

$$(biex) + (biex) \rightarrow 3(ex) + h\nu_{P_M}$$

$$h\nu_{P_M} = E_g - E_X - 2E_M . \qquad (4.5)$$

(c) Electron-Exciton Collision (S)

In this recombination process, first introduced by Benoît à la Guillaume,[4.14] the exciton is radiatively dissociated, giving its

kinetic energy to the electron. The momentum conservation of such a process gives the following relation:

$$K + k_i = k_f + q \tag{4.6}$$

where K is the exciton momentum, k_i and k_f the momenta of the electron in its initial and final states and q, the photon momentum being negligible. Therefore, in the collision process, the exciton momentum is given to the electron. The energy balance is[4.14]:

$$(ex) + e^- \rightarrow e^- + h\nu_S$$

$$E_g - E_X + \frac{\hbar^2 K^2}{2M_X} + E_g + \frac{\hbar^2 k_i^{\,2}}{2m_e^{\,*}} = h\nu_S + E_g + \frac{\hbar^2 k_f^{\,2}}{2m_e^{\,*}} \tag{4.7}$$

Assuming that the electron mass (m_e^*) is much smaller than the hole mass (m_h^*), then the electron mass is negligible compared to the exciton mass M_X and, at thermal equilibrium, the exciton initial momentum K is much larger than the electron momentum k_i. The emitted photon energy $h\nu_S$ can simply be written as:

$$h\nu_S = E_g - E_X - \left[\frac{\hbar^2 K^2}{2M_X}\right] \left[M_X/m_e^*\right] \tag{4.8}$$

The emission line intensity is proportional to the product of the density of exciton states and the thermal distribution of excitons:

$$I(h\nu_S) \propto E^{1/2} \exp(-E/k_B T) \tag{4.9}$$

where $E = \hbar^2K^2/2M_X$ and k_B is the Boltzmann constant. Since E can be rewritten as $E = \frac{1}{2} k_BT$, the emission band peak is therefore given by

$$h\nu_S = E_g - E_X - \frac{1}{2}\left[M_X/m_e^*\right]k_BT . \qquad (4.10)$$

Over a decade ago, Akimoto and Hanamura[4.16] performed a theoretical calculation of the binding energy of the excitonic molecule E_M as a function of the effective mass ratio $\sigma = m_e^*/m_h^*$. It has been shown that the excitonic molecules should be stable in the whole range of σ. In the case of ZnSe, $\sigma = 0.3$ and E_M is calculated to be 1.1 meV. This low binding energy could explain why biexcitons have never previously been observed in the luminescence spectra of ZnSe, because of the high probability of the molecule being thermally dissociated. Recently, using an effective temperature for the free excitons, T_f, Isshiki and co-workers[4.17] fit the shape of the no-phonon free exciton luminescence line and obtained a value of $T_f = 5.6$K. Thus, assuming a binding energy of 1.1 meV for the excitonic molecule, E_M, and the well-known values for E_g, E_X, M_X and m_e^*, the different radiative recombination processes mentioned previously should appear at:

$$h\nu_M(\max) = 2800.6 \text{ meV}$$
$$h\nu_P = 2782 - E^K_{e,h} \text{ meV}$$
$$h\nu_{P_M} = 2799.5 \text{ meV}$$
$$h\nu_S = 2800.6 \text{ meV} \qquad (\text{for } T = 5 \text{ K})$$

As one can see, the biexciton emission and the exciton-electron collision recombination should appear at about the same energy for an exciton gas temperature of ~5 K.

A very useful tool to discriminate between different kinds of radiative processes and to measure the quality of a sample is time-resolved spectroscopy. Figure 4.2 shows the decay of the different lines observed in sample No. 5 for an excitation intensity of 0.2 kW/cm^2, which corresponds to the spectrum of Figure 4.1(c). The measured 5.7 ns lifetime of the free exciton is, to the author's knowledge, the longest reported for a ZnSe crystal[4.18] showing the high-quality of the sample.[4.10] The lifetime of the E_X-LO phonon replica is measured to be 6.6 ns. This small difference between the two decay times can be explained by the polariton nature of the free exciton. The LO phonon assisted luminescence is not reabsorbed by the crystal, so its intensity is proportional to the total number of free excitons, but the no-phonon E_X line results only from the fraction of the diffusing free exciton cloud which reaches the surface and is transmitted as photons. Thus the longer lifetime of the LO replica, which is the true lifetime of the free exciton population, reflects this diffusion away from the sample surface. Finally, the decay of the donor BE (I_2) and the S-line were comparable to the E_X-LO decay curve. This is to be expected since both processes involve single excitons, are fed by the free exciton population, and are expected to have short radiative lifetimes. The same decay behaviour for the different lines was also observed for sample No. 1

Figure 4.3 shows the decay curves of the different excitonic lines for sample No. 5 but at an intensity of 3 kW/cm^2, corresponding to the spectrum 4.1(e). Again, the difference in lifetimes between E_X and E_X-LO can be explained by the same effect as mentioned earlier for the low excitation intensity case. However, the M and P_M emission peaks,

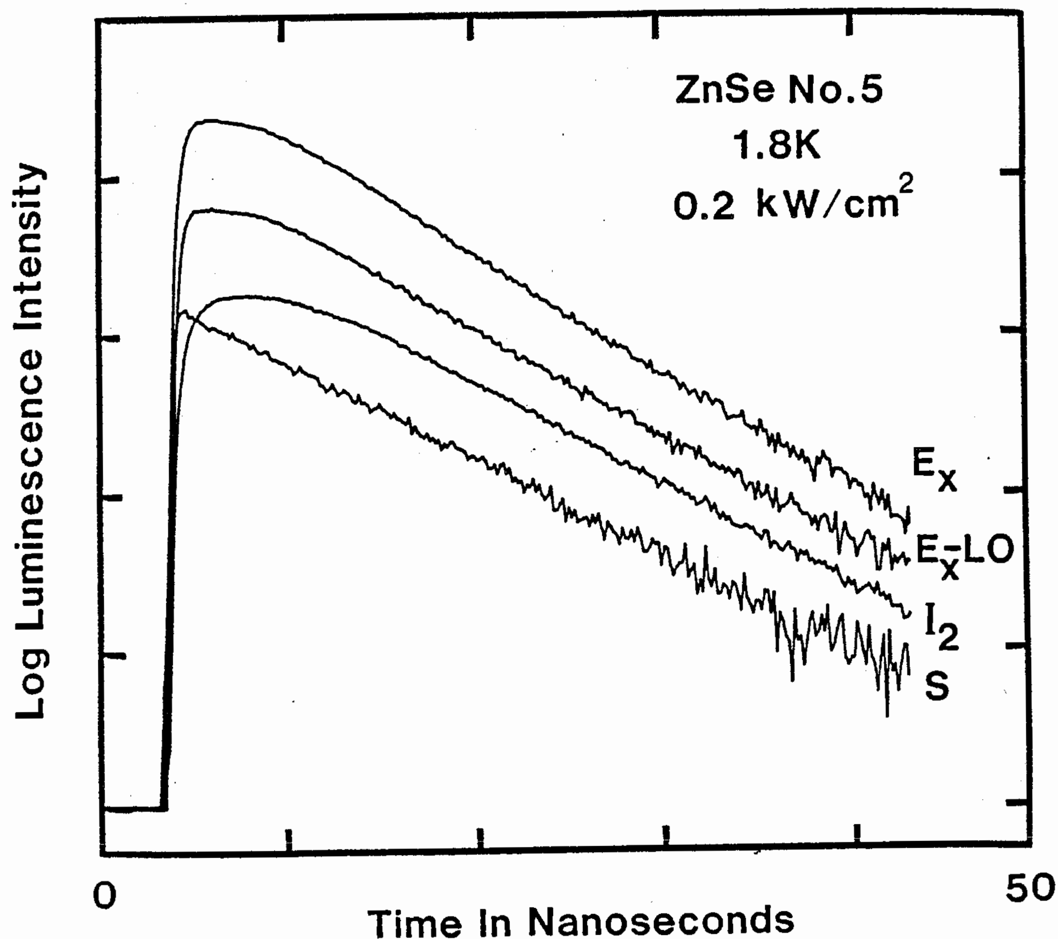

FIG. 4.2 The luminescence decay of the various exciton lines shown in Figure 4.1(c) (sample No. 5). The corresponding peak power was 0.2 kW/cm^2. Ex and Ex-LO represent the free exciton and its phonon-replica. I2 is the shallow donor bound exciton and S is due to radiative recombination of excitons associated with other free particles. Each of the tick marks on the vertical scale represents one decade of intensity. The decay curves represent exponential decays having time constants of τ_{Ex} = 5.7 ns, τ_{Ex-LO} = 6.6 ns, τ_{I_2} = 6.9 ns, τ_{S} = 7 ns. (The uncertainty $\Delta\tau$ = ±0.03 ns.)

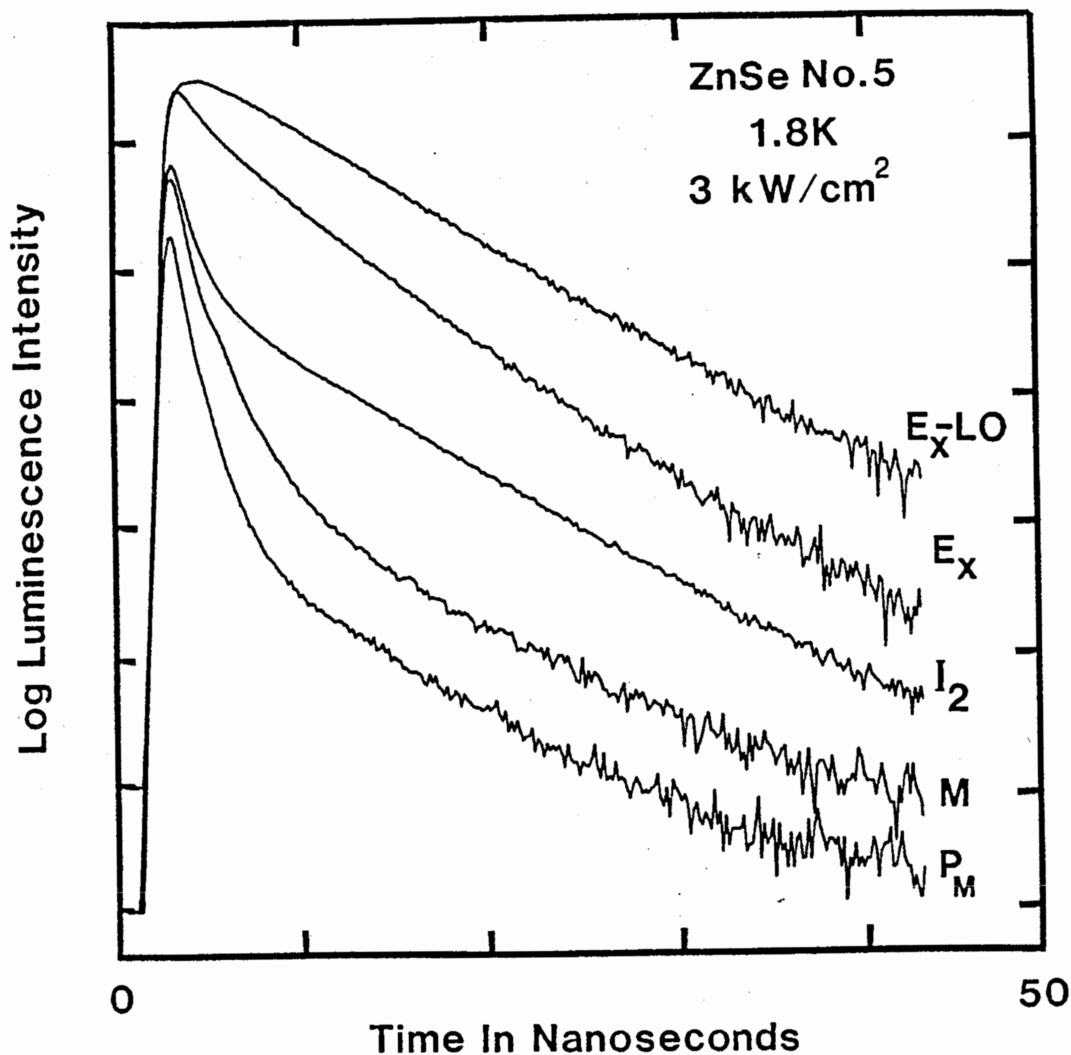

FIG. 4.3 The luminescence decay of the various lines shown in Figure 4.1(e) (sample No. 5) using an intensity of 3 kW/cm^2. The decay curves, when corrected for the instrumental response time, represent exponential decays having initial time constants of τ_{Ex} = 4 ns, $\tau_{Ex\text{-}LO}$ = 5.1 ns, τ_{I_2} = 5.1 ns, τ_M = 0.90 ns, τ_{P_M} = 0.45 ns. (The uncertainty $\Delta\tau$ = ±0.03 ns.)

which are only observed at high intensity excitation, show a very fast decay. Deconvoluting with the measured instrumental response function, the respective lifetimes were 0.9 ns and 0.45 ns. The donor BE decay curve, besides the fast initial decay which can be attributed to the low energy tail of P_M, follow exactly the E_X-LO decay just as in Figure 4.2. The same series of measurements were done on sample No. 1 and demonstrated the same general features as shown in Figure 4.4.

The fact that the lifetime of the S and M peaks, each normalized to the free exciton lifetime, are so different, and that the S peak does not show the superlinear dependence on pump power revealed by M (and P_M), suggests that there are two different radiative recombination processes at ~2800 meV. It is suggested that the S-line is attributed to electron-exciton collisions, as previously proposed by Ishhiki *et al.*,[4.10,4.11] and that the M band is due to biexciton emission. Biexcitons in ZnSe were experimentally observed by Itoh *et al.*[4.19] using two-photon-resonant Raman scattering where they obtained a binding energy of 2.2 meV. In their experiment, a peak power of 20 kW/cm^2 was necessary for the formation of biexcitons. Their theoretical fit for the M-band was done by adopting an effective temperature of the excitonic molecules of 30 K. In the present work, an intensity of 3 kW/cm^2 was sufficient to observe such effects. The long lifetime of the free exciton in the present samples is at the origin of the formation of biexcitons at such relatively low excitation power. The apparent biexciton lifetime should be shorter than the free exciton lifetime if the system is in quasi-equilibrium, since the rate of biexciton formation goes as the square of the free exciton density. If the free exciton photoluminescence decays with a lifetime τ, one would

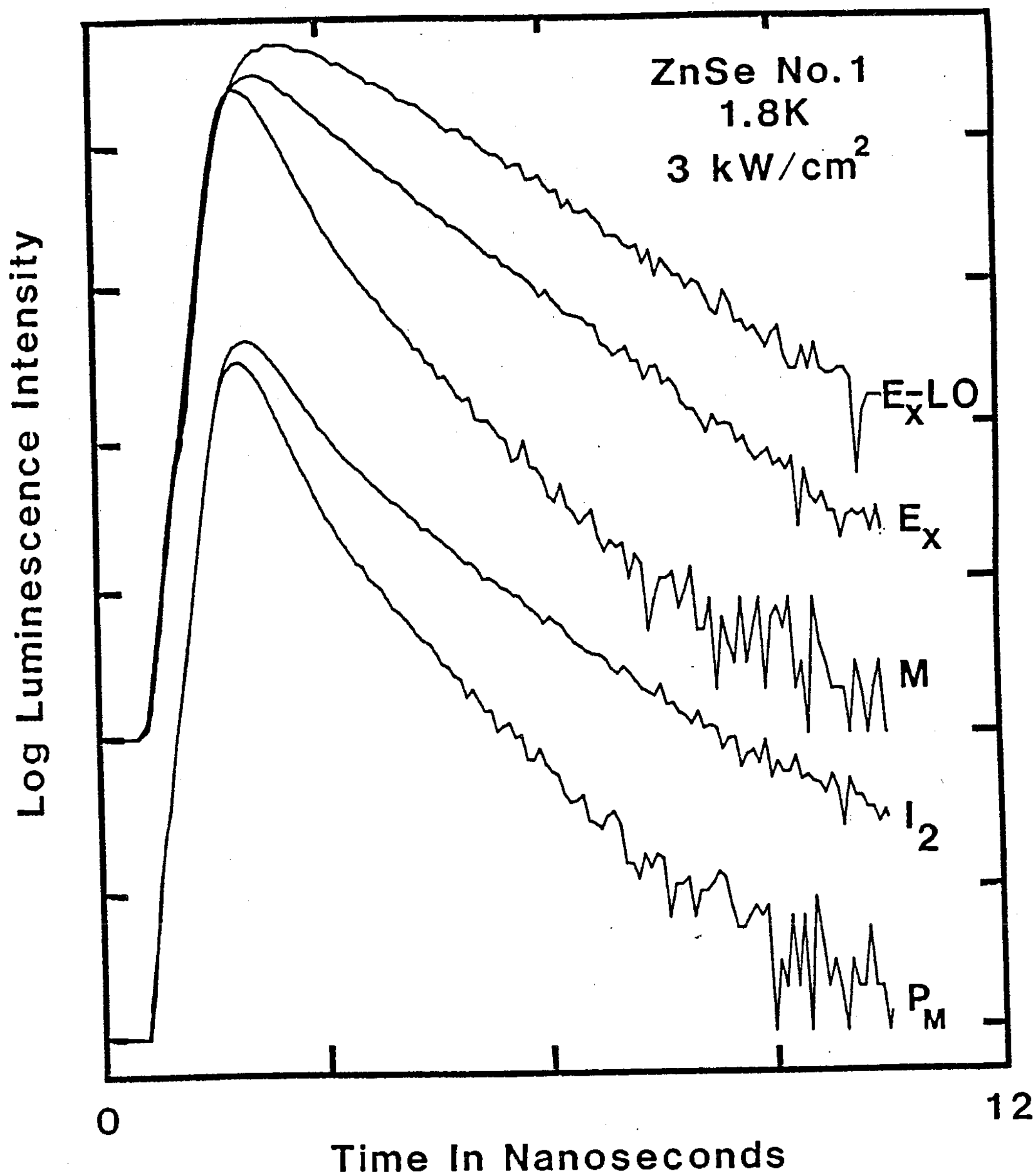

FIG. 4.4 The luminescence decay of the various lines shown in Figure 4.1(b) (sample No. 1) using an intensity of 3 kW/cm^2. The decay curves, when corrected for the instrumental response time, have initial exponential decays having time constants of τ_{Ex} = 1.08 ns, $\tau_{Ex\text{-}LO}$ = 1.28 ns, τ_{I_2} = 1.28 ns, τ_M = 0.45 ns, τ_{P_M} = 0.25 ns. (The uncertainty $\Delta\tau$ = ±0.03 ns.)

expect the apparent biexciton lifetime to be $\frac{1}{2}\tau$ (sample No. 1) in a system having uniform density. However, the free exciton <u>density</u> may also be decreased by diffusion into the sample resulting in an even shorter observed biexciton lifetime as seen in sample No. 5. In the case of the S-band, which has a decay time comparable to the free exciton, the free-electrons involved in the process could originate from the ionized donors.[4.10]

The peak P_M, which is always observed along with the M-line, and shows an even more superlinear dependence on pump power, can be attributed to biexciton-biexciton collisions. From Equation 4.5, the photon emitted from such a collision should appear at an energy of ~2799.5 meV, which is roughly the energy of the P_M line. Furthermore, the apparent lifetime of this line was observed to be half the lifetime of the biexciton (M-line), which is to be expected since the rate of biexciton-biexciton collisions should go as the square of the biexciton density.

In summary, the M-line has been identified as a radiative transition of an excitonic molecule to a free exciton on the basis of a consideration of luminescent intensity dependence on excitation power and also lifetime measurements. The P_M luminescence line is produced by the emission process of an excitonic molecule associated with the inelastic collision with another excitonic molecule, in which one of the four excitons involved is radiatively annihilated, leaving the other three as single excitons. These results are found to be in excellent agreement with the theoretical analysis of the energy balance equation for each emission band. The theoretical prediction of the biexciton binding energy of 1.1 meV was found to be most consistent with the

observed results.

4.3 Time Evolution of the Biexcitons in Bulk GaAs

As discussed in the previous section, when the concentration of free excitons or polaritons in a semiconductor obtained by optical excitation is sufficiently high, excitonic molecules or biexcitons can be formed. Such biexcitons are molecules formed with two excitons in a similar way to a hydrogen molecule. The radiative decay of such biexcitons corresponding to the annihilation of one exciton leaving a free exciton or polariton gives rise to a characteristic PL peak below the free exciton peak. A PL feature attributable to a biexciton in GaAs had, until recently, not been observed, presumably due to the small expected binding energy of the biexciton which must be less than the 1 meV binding energy of the neutral donor bound exciton (D^{o},X) in GaAs. This puts the spectral position of the biexciton in the same spectral region as the very strong (D^{o},X) luminescence peaks. However, improvement in the MBE growth technique has recently resulted in the growth of GaAs of sufficient purity that the luminescence is dominated by intrinsic recombination.[4.20]

The biexciton line in PL is characterized by a reverse Boltzmann-like lineshape which is due to the kinetics of the recombination.[4.21] A biexciton having a mass 2M and a velocity V has a mechanical momentum of 2MV and a kinetic energy of MV^2. As the biexcitons recombine, a photon is emitted and an exciton of mass M is left in the final state. Due to momentum conservation, this exciton must have a velocity 2V, neglecting the photon's momentum, and thus

possesses $2MV^2$ of kinetic energy. Thus hot biexcitons, i.e. those with larger kinetic energy, result in luminescence to lower energy than those with small initial biexciton kinetic energy. Corrections to this lineshape arise from collisions between excitons, biexcitons and free carriers.[4.22] The biexciton line is further characterized by a superlinear PL intensity *vs.* excitation density behaviour and by having a shorter lifetime than the free exciton. As already discussed in section 4.2, both of these effects are attributed to the fact that the biexciton density is proportional to the square of the free exciton density.

Time-resolved PL measurements, as well as excitation density dependence measurements, have been carried out on an extremely high-purity MBE-GaAs sample. The sample was grown at GTE Laboratories on (100) Silicon-doped GaAs substrates at a growth rate of 0.6 μm/hr. The bulk GaAs studied was actually a high-purity buffer layer (10 μm thick) on top of which were grown several quantum wells. The existence of the QW was irrelevant in the experiment since the luminescence feature of the bulk GaAs layer was at a lower energy than the QW luminescence. For the low temperature PL studies, the sample was mounted strain-free in an immersion dewar in superfluid He and excited with pulsed 660 nm radiation obtained from the mode-locked pumped dye laser system referred to in Chapter 2. The luminescence was detected with the Varian VPM-159A3 photomultiplier using the time-correlated photon counting technique resulting in a total system time resolution of 300±30 ps. The time windowing technique discussed in section 2.4 was also used.

Figure 4.5 shows the low temperature PL spectra taken at low (curve

a) and high (curve b) excitation density. The spectrum taken at low intensity is dominated by the free exciton peak (X), with very small contribution originating from the donor BE (D^{o},X) and the acceptor BE (A^{o},X). At higher excitation densities, however, the impurity recombination channel saturates and the luminescence shows contributions only from the free exciton X as well as a new line labeled X^2 which is attributed to the biexciton. This X^2 line was found to display the required superlinear excitation density dependence for a biexciton recombination. The fact that both the X and X^2 lines are substantially broadened compared to the X linewidth at low excitation densities can be interpreted as being due to the elevated temperature of the excitons and biexcitons at this higher excitation density as well as collision broadening due to the high density of excitons, biexcitons and free carriers.

In Figure 4.6 the PL decay of the exciton and biexciton are displayed. As required for a biexction, the lifetime was found to be substantially shorter than the exciton lifetime (1.8 ns for the biexciton compared to 2.4 ns for the free exciton). Spectra collected for different time windows after the laser pulse are shown in Figure 4.7. The temporal evolution of the free excitons and the biexcitons was studied for the first 10 nanoseconds after pulse laser excitation. This series of spectra shown in Figure 4.7 provide very convincing evidence of the biexciton nature of the X^2 line. In the early time windows, the exciton and biexciton gases are very hot and the respective Boltzmann and reverse Boltzmann distributions are far apart. As the distributions cool, with increasing time delay after the laser pulses, the exciton peak moves to lower energy while the peak of the biexciton distribution

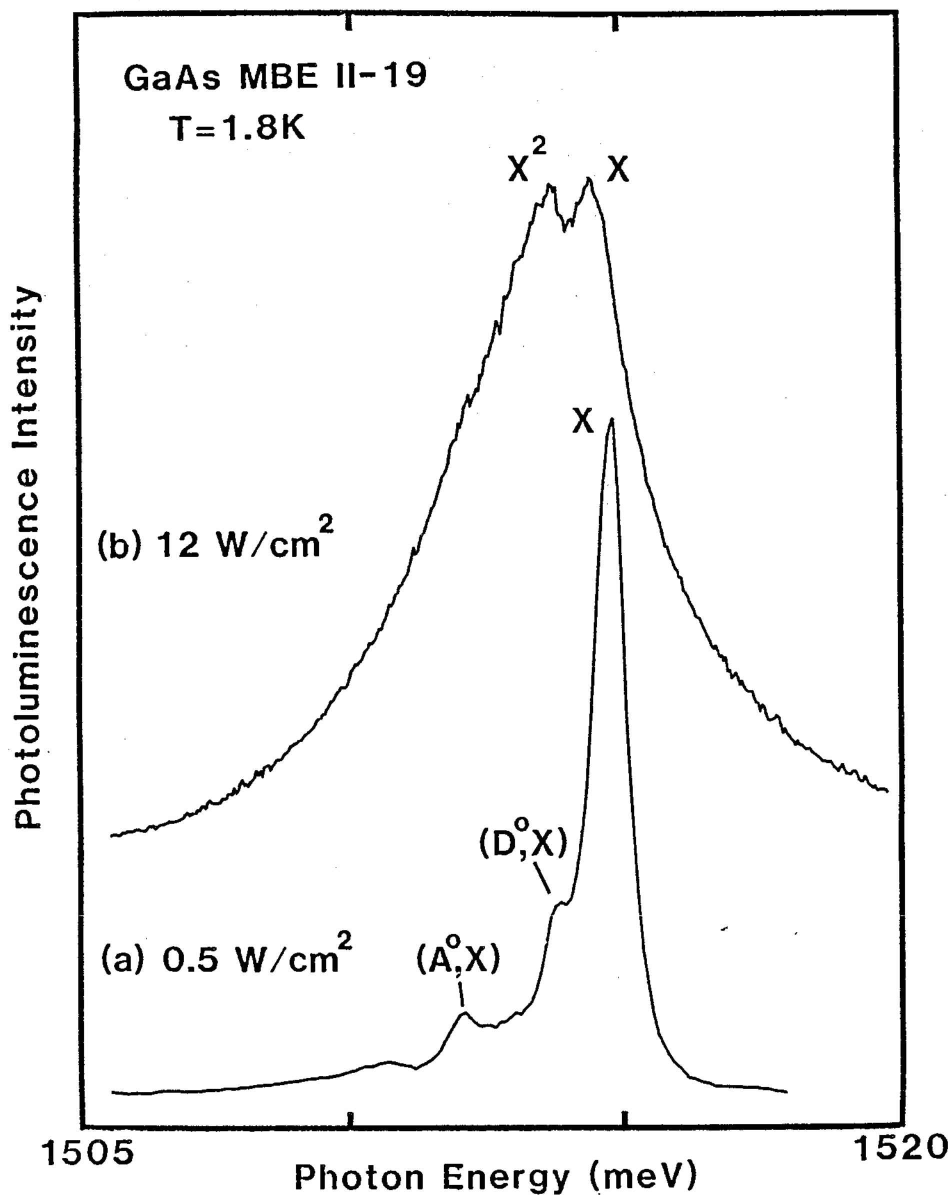

FIG. 4.5 Low temperature PL emission spectra taken at an average excitation intensity of $0.5 W/cm^2$ (a) and $12 W/cm^2$ (b). The pump wavelength was 660 nm at a repetition rate of 4 MHz.

FIG. 4.6 Luminescence decay of the free exciton (x) and the biexciton (x^2) obtained from the spectrum of Figure 4.5(b). Each of the tick marks on the vertical scale represents one decade of intensity. The time constant of the exponential decays were τ_{x^2} = 1.80±0.03 ns and τ_x = 2.40±0.03 ns.

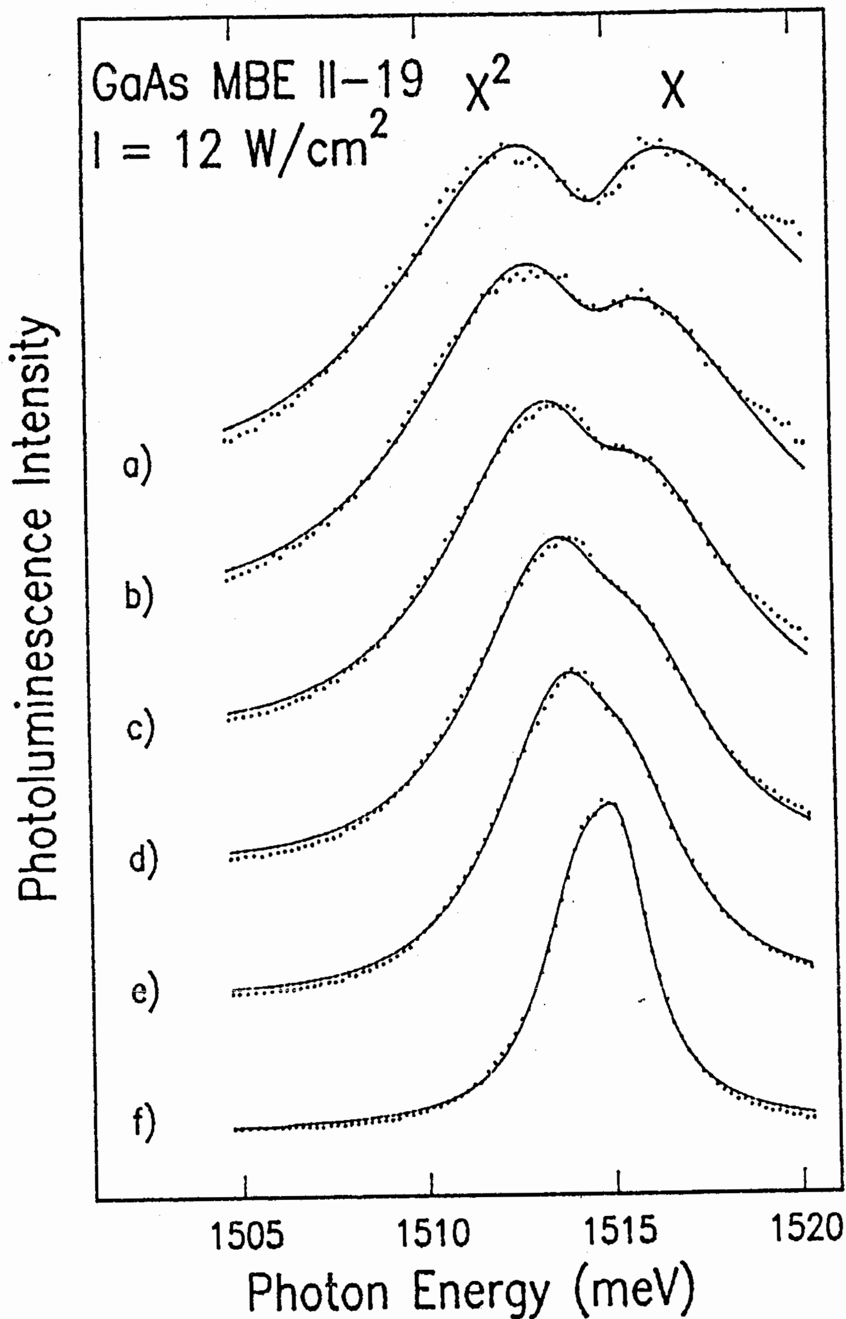

FIG. 4.7 Series of spectra acquired for different time windows following the pulsed laser excitation. The dots represent experimental data obtained and the lines were generated from the fit explained in the text. The different time windows are a) 0-0.07ns, b) 0.7-1.3ns, c) 1.3-2.0ns, d) 2.0-2.7ns, e) 2.7-3.4ns and f) 4.6-5.3ns.

moves to higher energy precisely as expected for the temperature dependence of a reverse Boltzmann-like distribution characteristic of biexcitons.

The fit to the biexciton lineshape shown in Figure 4.7 resulted in a biexciton binding energy of 0.7±0.2 meV. The fit was generated using available theories.[4.20,4.22-4.24] The effects of collisions of biexcitons with excitons and biexcitons were found to be essential to the quality of the fits. According to Hanamura,[4.25,4.26] a line shape obtained by the convolution of a Lorentzian function and a Boltzmann function could explain such scattering processes. Consequently, the fits were obtained by simply generating forward and reverse Boltzmann distributions for the free exciton and biexciton respectively and then convoluting these with Lorentzian broadenings to obtain the fitted spectrum. It was necessary to simultaneously fit both the free exciton and biexciton due to the substantial overlap of these luminescence features. Both the free exciton and the biexciton gases were allowed to have different temperatures and broadenings since the bulk of the luminescence intensity in these features could originate from different volume in the crystal. However, the temperature and broadening for both gases were found to be quite similar for each of the time windows. The temperatures and broadenings were found to decrease monotonically with increasing time as expected. A free exciton temperature of 37 K was found for the first time window compared to 7.5 K for the last time window. The binding energy in this model was simply obtained from the energy difference between the onset of the respective Boltzmann distributions. The best fit for all time windows was obtained by using a binding energy of 0.7 meV, whereas fits obtained using 0.5 and 0.9 meV

binding energies showed significantly worse results.

Over a decade ago, Brinkman and co-workers[4.3,4.27] calculated some theoretical binding energies of excitonic molecules for various semiconductors. Their variational calculations of the biexciton binding energy was calculated as a function of the mass ratio $\sigma = m_e^*/m_h^*$. The results obtained were easy to interpret for values of σ larger than 0.1. However, for values of $\sigma \leq 0.1$, the data were not found to be very accurate.[4.16,4.28] In the case of GaAs, $\sigma = 0.14$ and a biexciton binding energy of 0.4±0.1 meV can be extrapolated from their theory. This value is in reasonable agreement with the experimental binding energy of 0.7±0.2 meV obtained here.

In summary, the arguments in favor of the existence of biexcitons in bulk GaAs are very strong. The time evolution of the free exciton and the biexciton gases after pulse excitation has led to an experimental value of the biexciton binding energy which is in good agreement with the theory available.

4.4 Optical Investigation of Biexcitons and Bound Excitons in GaAs Quantum Wells

From the earliest work by Dingle *et al.*[4.29] on the optical properties of GaAs-$Al_xGa_{1-x}As$ quantum wells, it was evident that excitons play a much more significant role in these two-dimensional systems than in bulk GaAs. As discussed in section 1.4, the PL at low temperatures from a few microns of high-quality MBE-grown undoped GaAs is usually predominantly extrinsic in nature. This is in marked contrast to GaAs QW with similar purity to the bulk GaAs material mentioned above. Absorption, emission and excitation of high-quality

GaAs QW with good interfaces demonstrate that intrinsic free exciton recombination dominates the emission even at very low temperature where bound exciton and impurity processes dominate for the bulk GaAs.[4.30-4.31]

In a recent study, using low temperature PL from a number of high-quality multiple-GaAs-quantum well samples grown by MBE, Miller and co-workers[4.32,4.33] first reported a double peak whose splitting was ~1 meV. The high energy peak was attributed to the n = 1 heavy-hole free exciton transition. Based on the excitation intensity, temperature and polarization dependencies of the lower-energy peak, they concluded that this transition was due to biexcitons with a binding energy of about $B_{xx} = 1$ meV. These results were also supported by Kleinman[4.34] who, using the six-parameter wave function of Brinkman, Rice and Bell,[4.3,4.35] calculated variationally the binding energy of the biexcitons and the bound excitons in GaAs QW for various well thicknesses (L_z). This calculation contained no adjustable parameters other than the variational parameters and yields a value of $B_{xx} = 0.4$ meV for bulk GaAs.[4.3] For the GaAs QW it was found that the calculated biexciton binding energy obeyed Haynes' rule[4.36,4.37] and that in the 2D limit the ratio of the biexciton binding energy over the exciton binding energy was 2-3 times larger than the corresponding quantity in the 3D case. The calculated value of B_{xx} was found to be in good agreement with the 1 meV splitting mentioned above for wells narrower than 25 nm ($L_z < 25.0$ nm).

It has recently been proposed that interrupting the molecular beam epitaxial growth momentarily when changing from one type of semiconductor layer to another leads to smoother interfaces.[4.38] The

low temperature PL spectra of QW structures prepared with interrupted growth showed multiple peaks which have been interpreted as originating from within different atomically smooth regions in the QW layer which differ in width by exactly one monolayer.[4.38] (These results will be discussed in more detail in Chapter 5.) However, it must be remembered that fine structure in low temperature PL spectra may have other causes such as impurity transitions. Using this interrupted growth technique, one would expect the concentrations of residual impurities to increase at the interface which could give rise to additional structure in the low temperature PL. Kleinman[4.34] has also estimated the binding energy of excitons bound to neutral donors for the GaAs QW. These values are slightly larger than B_{xx} and are also found to obey Haynes' rule. Nomura and co-workers[4.39] used PL measurements to study single quantum wells inhomogeneously doped with Si. They identified the low energy peak as being due to excitons bound to donors localized at the centre of the well. The experimental data of the donor binding energy dependence on the well width agreed with the theoretical results obtained by Kleinman[4.34] for the well widths ranging from 7.4-15.4 nm. In this section it is shown that low temperature PL can be ambiguous and care must be taken in the interpretation of the results. The excitation density dependence of the luminescence intensity and time-resolved PL measurements were used in the investigation of a luminescent peak located ~1 meV below the n = 1 heavy-hole free exciton transition on two different QW samples, one grown using the interrupted growth technique and the other grown with conventional, uninterrupted growth.

The excitation source used in this experiment was the cavity dumped

dye laser system described in Chapter 2 with a repetition rate of 80 MHz and a pulse width of less than 30 ps. The excitation wavelength was 800 nm at an average power density of $I_o = 1.0\ W/cm^2$. The samples were mounted in a strain-free manner and immersed in 1.8 K superfluid He. The luminescence was dispersed by a double 3/4 m spectrometer coupled to a fast photomultiplier tube (ITT-F4128F). The lifetimes were obtained in the usual way (as discussed in section 2.4) by timing the interval between the laser pulses, detected by a fast Si-avalanche photodiode, and the luminescence photon pulses using a time-to-amplitude converter. The output of the TAC was then processed by a microcomputer based pulsed-height analyzer. This tube has an exponential decay time constant of 70±10 ps when used in conjunction with our photon counting electronics. Both $GaAs/Al_xGa_{1-x}As$ QW samples were grown at GTE Laboratories in a Riber 2300 MBE system. Growth conditions were optimized using reflection high energy electron diffraction (RHEED) intensity recovery and oscillation studies. For sample 212, grown continuously, the undoped substrate temperature was 650°C and the growth rate was 0.9 $\mu m/hr$. The narrowness of the low temperature PL peaks from the QW attested to the high quality of this sample.[4.40] For sample II-17 epitaxial layers were grown, using growth interruption, on (100) silicon-doped GaAs at substrate temperature of 600°C at a growth rate of 0.6 $\mu m/hr$. A superlattice buffer layer was grown on the substrates to provide a smoother and cleaner starting surface followed by a series of undoped single quantum wells of different widths. Growth interruption was accomplished at each interface by shuttering the ovens producing the group III elements for 60 seconds while maintaining an arsenic overpressure.

The excitation intensity dependent PL spectra for both QW samples are represented in Figure 4.8. Curves (a), (b) and (c), whose energy scale is indicated at the top of the figure, were obtained from sample MBE 212 having a well thickness L_z of 14.2 nm. The two peaks X and X^2 are clearly seen for the three excitation intensities with a separation of 1.25 meV. At the lowest value of excitation intensity, curve (c), the X-peak dominates the spectrum. As the laser intensity increases (curves (b) and (a)), the lower energy peak becomes dominant. If the intensities of these two peaks are plotted as a function of excitation power density (I_p), one obtains an approximately linear dependence $(I_p)^{0.98}$ for the X-peak while the lower energy peak, X^2, exhibits a superlinear dependence and grows approximately as $(I_p)^{1.25}$. Such linear dependence is expected for free excitons, whereas a superlinear behaviour is characteristic of biexcitons.[4.41] In order to confirm the intensity dependent results, the transient luminescence decays of both X and X^2 peaks have been measured at the three power densities used in Fig. 4.8. The results are shown in Fig. 4.9. One common feature of these decay curves, independent of the intensity of excitation used, is the shorter lifetime of peak X^2 as compared to that of the higher energy exciton line (X) (approximately 1.7 times faster). This is again what would be expected if the lower energy transition was due to the biexciton. In fact, the apparent decay rate of the biexciton is predicted to be two times faster than that of the free exciton for quasi-equilibrium as already discussed in section 4.1.

The same sets of experiments were done on a 18.0 nm wide QW in sample MBE-II-17 which was grown using the interrupted growth technique. In this sample, the doublets observed in the PL spectra of narrower QW

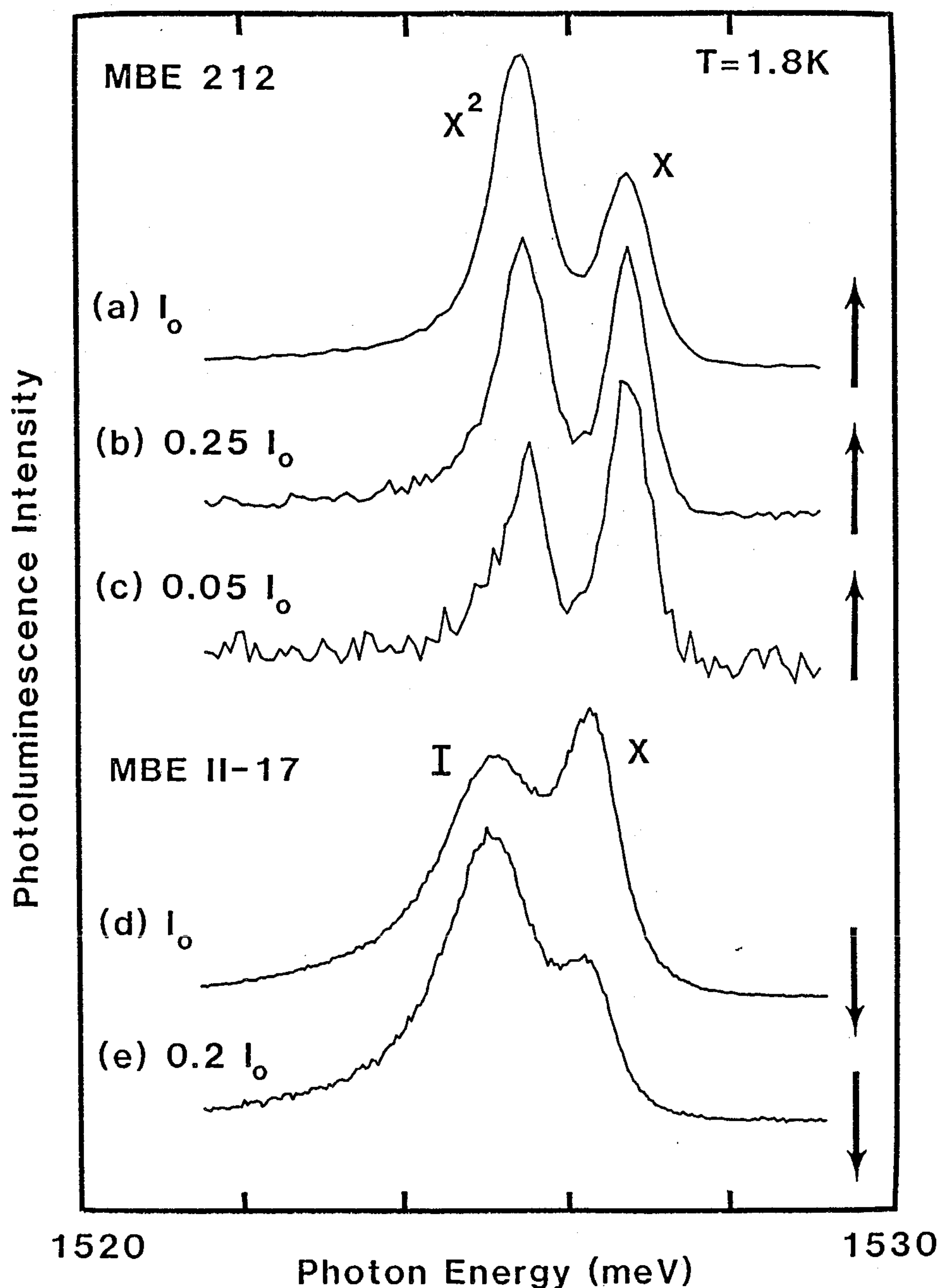

FIG. 4.8 Low temperature (1.8 K) PL spectra at different excitation powers. Curves (a), (b) and (c) correspond to a sample (MBE 212) which was grown with no growth interruption. The well thickness is L_z = 14.2 nm and the energy scale for the luminescence from this QW is located at the top of the figure. Curves (d) and (e) represent the PL spectra of sample MBE II-17 which was grown using the interruption growth technique. The well thickness is L_z = 18.0 nm and its photoluminescence energy scale is located at the bottom of the figure. For all the spectra collected, the laser wavelength was 800 nm at a maximum average power density I_o = 1.0 W/cm^2.

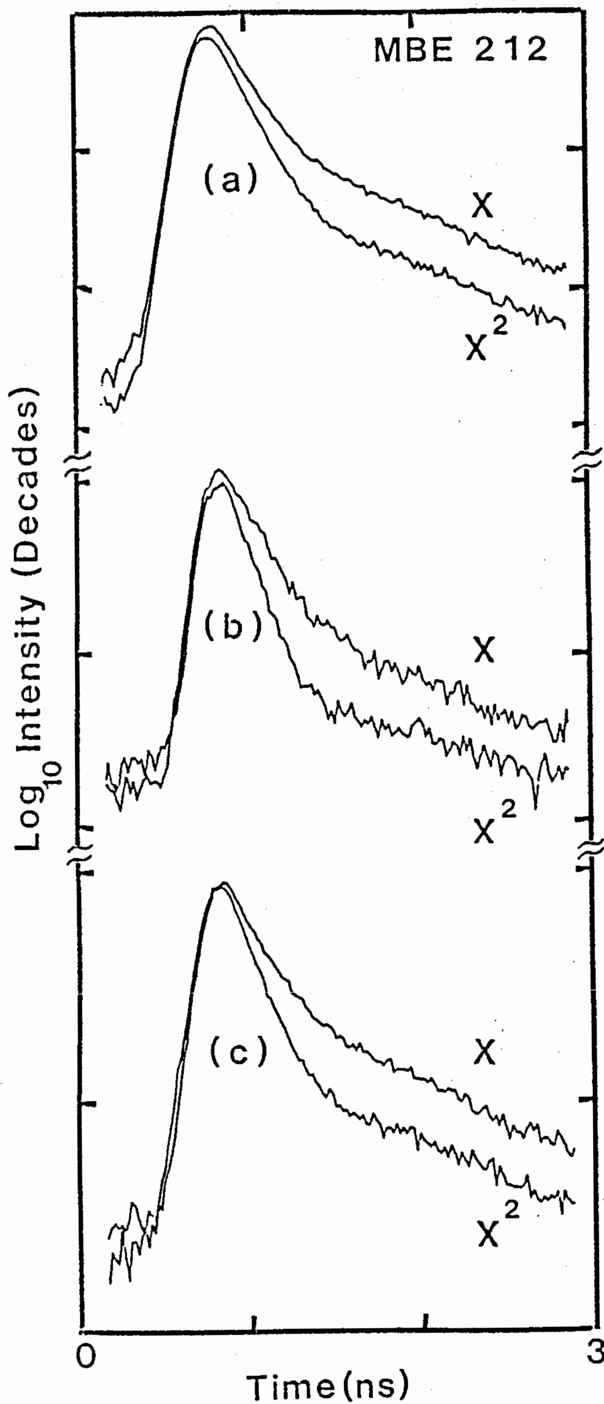

FIG. 4.9 The luminescence decay of the lines X and X^2 for sample MBE 212 corresponding to the conditions of excitation of Fig. 4.8(a), (b) and (c) respectively. Each of the tick marks on the vertical scale represents one decade of intensity. The decay curves represent exponential decays having time constants of (a) τ_X = 211 ps; τ_{X^2} = 178 ps, (b) τ_X = 246 ps; τ_{X^2} = 163 ps, (c) τ_X = 281 ps; τ_{X^2} = 187 ps. (The uncertainty $\Delta\tau = \pm$ 10 ps.)

(L_z = 3.0 nm) was attributed to free (X) and impurity-related (I) emission, although higher-lying structure due to large island formation could be distinguished using PL excitation spectroscopy, temperature dependent PL and time-resolved PL spectra.[4.38] These results will be discussed in detail in section 5.1. For wider QW this structure is unresolvable. The different thickness of the QW's studied in this work (L_z = 18.0 nm for MBE II-17, compared to L = 14.12 nm for MBE 212) is responsible for the different energy scale for use with Fig. 4.8(d) and (e). Again a doublet is observed with about the same energy spacing. However, when the intensity of excitation is decreased, the low energy component of the doublet becomes stronger relative to its high energy counterpart. This is the opposite effect of what is observed for sample MBE 212, but exactly what is expected for an extrinsic (bound exciton) process which saturates at higher excitation levels. As before, the decay curve of each peak was recorded for the different intensities of excitation and are shown in Figure 4.10. The decay of the free exciton luminescence X was exponential and faster than that of the I peak for both of the power densities used. Surprisingly, the lifetimes of the X and I lines were found to depend on the pump intensity. A saturation of the extrinsic recombination channels might be at the origin of the lengthening of the lifetimes with increasing pump power. The important point here, however, is that the decay time of the lower energy peak I of this sample follows very closely but always exceeds the decay time of the free exciton line, in contrast to what was found in sample MBE 212 for the peaks X^2 and X.

On the basis of these results obtained from the excitation density dependence of the PL intensity and the transient behaviour, it is clear

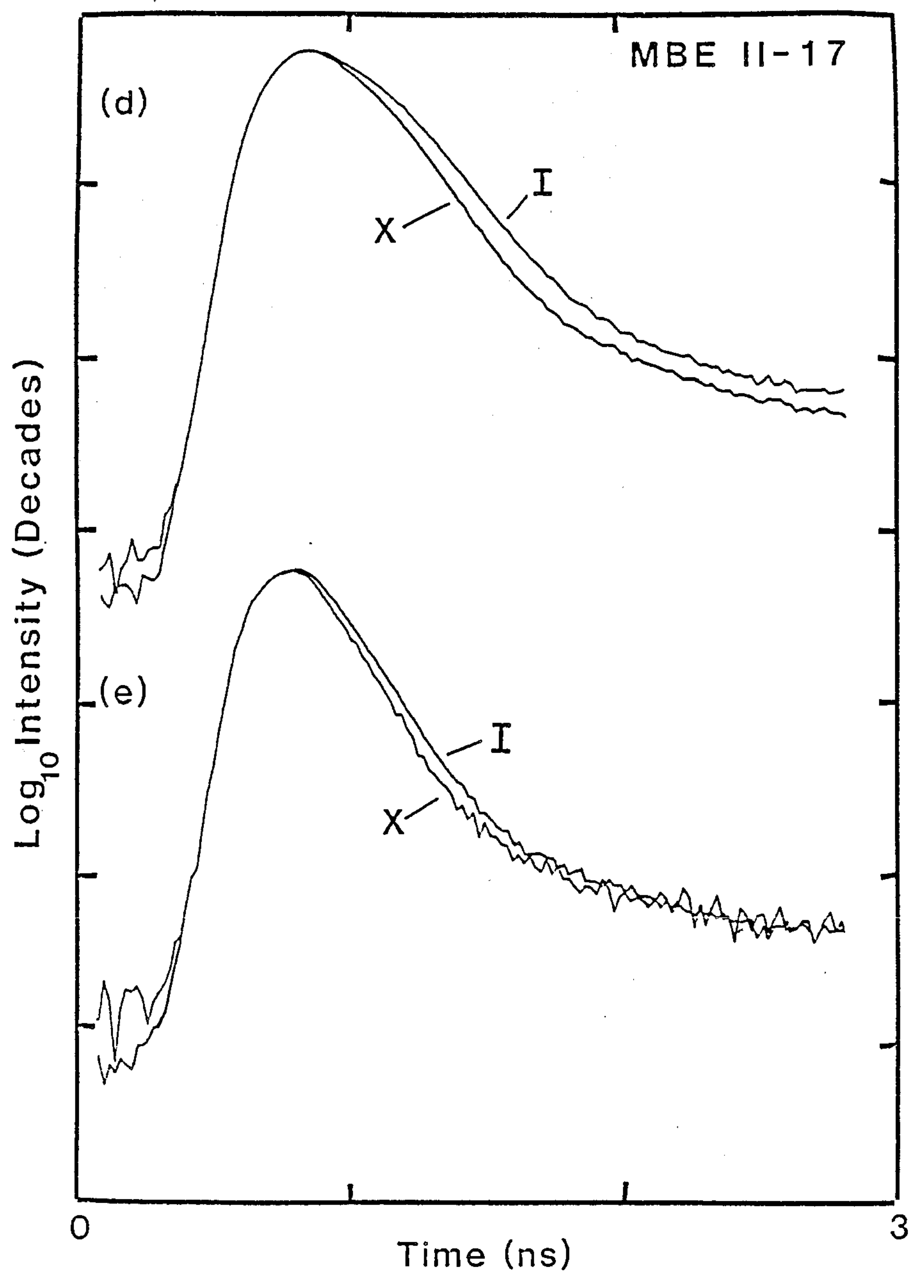

FIG. 4.10 The luminescence decay of the lines X and I of sample MBE II-17 for the two excitation conditions shown in Fig. 4.8 (d) and (e). The decay curves represent exponential decays having time constants of (d) τ_I = 232 ps; τ_X = 203 ps, (e) τ_I = 179 ps; τ_X = 171 ps. (The uncertainty $\Delta\tau$ = ±10 ps.)

that the low energy components of the doublets, i.e. X^2 for sample MBE 212 and I for sample MBE II-17, originate from very different recombination mechanisms. As discussed previously, one would expect the concentrations of residual impurities to be increased at the interface for samples grown under the interrupted growth technique (eg. MBE II-17). Both sets of results for this sample (excitation density dependence of the PL and the transient behaviour) are in good agreement with the attribution of peak I to an exciton bound to an impurity (probably donor) within the well. The saturation of the donor bound exciton line I with increasing excitation intensity is due to the finite concentration of impurities. This saturation effect was also observed by Nomura *et al.*[4.39] for their donor bound exciton peak in doped QW's. Furthermore, since the bound excitons are fed by the free excitons, the bound exciton line can never decay more rapidly than the free exciton, in agreement with our results. The theoretical calculation of Kleinman[4.34] for the binding energy of the donor bound exciton as a function of well thickness leads to a value of 1.4 meV for an 18.0 nm well. However, one should keep in mind the predicted systematic shift of the binding energy as the impurity's core comes closer to the edge of the QW which, for the interrupted growth conditions, has to be taken into consideration.[4.42] In sample MBE 212, however, the behaviour of the lower energy peak is clearly that of a biexciton.

In summary, experimental studies of the double peak observed in the PL spectra of QW have shown that care must be taken in the assignment of the low energy component of the doublet. This low energy peak may be due either to the biexciton or an impurity bound exciton (or both), depending on the growth technique and quality of the QW, and also on the

excitation conditions.

4.5 Conclusion

As discussed in this chapter, the arguments in favour of the observation of biexcitons are very strong for ZnSe, bulk GaAs and GaAs-$Al_xGa_{1-x}As$ QW. In these substances the value of the binding energy was found to be in reasonable agreement with the theory. The lifetime of the free excitons in both bulk ZnSe and GaAs were the longest reported for these direct gap semiconductors, showing the high-quality of the crystals studied. It was demonstrated that at high concentrations, inelastic collisions between biexcitons and biexcitons was a very important radiative recombination processes in high-purity ZnSe.

Finally, the low energy luminescent peak of the doublet observed in the high-purity GaAs-$Al_xGa_{1-x}As$ QW was assigned to either biexciton recombination or to bound exciton recombination depending on the growth technique used. In the case where growth interruption was used, it was reasonable to assume that concentrations of residual impurities are increased at the interface which give rise to additional structure, such as BE recombination, in the low temperature PL. However, several recent publications[4.43-4.45] have described dramatic changes in the character of GaAs/$Al_xGa_{1-x}As$ interfaces when their growth by MBE is interrupted by times of the order of 1 minute. PL spectra of GaAs QW grown using this technique have shown the high-quality of the interfaces.[4.17] The next chapter is dedicated to such QW structures and to some fascinating quantum effects related to these semiconductor quantum wells.

CHAPTER 5

PHOTOLUMINESCENCE OF EXCITONS IN QUANTUM WELLS

5.1 Introduction

With the development and improvement of semiconductor growth techniques such as MBE, the study of *artificial semiconductor* superlattices has rapidly advanced. The growth rate using MBE is slow enough (~1.0 μm/hr) that both material composition and impurities can be controlled on the atomic scale. Recent experiments suggest that multi-quantum well structures can be prepared with monoatomic layer smoothness and uniformity resulting in luminescence transition widths at 2 K of less than 0.15 meV for the GaAs-$Al_xGa_{1-x}As$ system.[5.1] This is comparable to the linewidths from high-quality bulk GaAs. For QW wider than ~100 Å, one observes PL spectra which look qualitatively quite similar to that of bulk GaAs, but each transition is shifted to a higher energy. In addition to peaks resulting from the recombination for both heavy and light-hole free excitons (as discussed in Chapter 1), additional peaks from the recombination of bound excitons, as well as transitions related to shallow impurity levels, are observed, as already reported in section 4.4.

Multiple peaks, recently observed in low temperature PL spectra of GaAs-AlGaAs single QW fabricated by momentarily interrupting the molecular beam epitaxial growth between adjacent but different semiconductor layers, have been interpreted as originating within smooth regions in the QW layer differing in width by exactly one monolayer.

The first part of this chapter deals with similar structure observed in similarly grown samples. It will be demonstrated that low temperature PL can be misleading but that higher temperature PL or PL excitation spectroscopy does provide unambiguous evidence for the model of interface smoothing due to growth interruption. Further, time-resolved spectra yield decay times of the individual peaks which are consistent with this model.

The second part of this chapter deals with structures employing more than one QW with interwell spacings and barriers sufficiently small so that significant amounts of interaction take place. In such structures, referred to as Coupled Quantum Wells,[5.2] one important issue arises: the effect of coupling on the energies of the electrons and holes located in adjacent wells. Since the hole and the electron can tunnel through the thin barrier, the wavefunctions are shared between both wells, and the distribution can be adjusted by applying an electric field to tilt the band. An electric field applied perpendicular to the layers of QW has been known to change the optical absorption, reflection and PL properties[5.3-5.5] of such structures. In addition, an increase of the recombination lifetime with applied electric field should be observed as a consequence of the decreased electron-hole wavefunctions overlap. A detailed experimental study of the influence of electric fields on exciton states and lifetimes in a GaAs-GaAlAs coupled double QW structure will be presented in section 5.3.

5.2 Photoluminescence Study of Single QW Fabricated Under Conditions of Interrupted Growth

Interface properties are thought to play a major role in

heterostructure devices and in the properties of light-emitting devices.[5.6-5.8] High-quality interfaces are important for obtaining a better understanding of the fundamental properties of these structures and for the optimization of novel devices based on them. It has recently been proposed that interrupting the MBE growth momentarily when changing from one type of semiconductor layer to another results in surface, and therefore interface, smoothing. Various groups have used low temperature PL spectra in attempts to confirm this idea.[5.9-5.11] It was demonstrated that in narrow QW (L_z < 6 nm), fine structure observed in the PL spectra could be interpreted as due to emission from free excitons in QW with atomically smooth interfaces and large areas (i.e. large compared with the size of a two-dimensional exciton). In this model, changes in QW width occur only in discrete monolayer steps at each interface (where a monolayer corresponds to a/2 = 0.283 nm where a is the lattice constant of GaAs). If only single monolayer steps are present at each interface, then only three free exciton peaks, corresponding to QW widths of $L_z = n(a/2)$, $n(a/2)+(a/2)$, $n(a/2)-(a/2)$ where n is an integer, would be possible.[5.10] The relative intensities of these peaks in the PL spectrum would be related to the relative areal densities of the three different QW widths, to the coupling among the wells and on thermalization factors. However, it must be remembered, as presented in section 4.4, that fine structure in low temperature PL spectra may have other causes such as impurity transitions and thus must be interpreted with care. As discussed in section 4.4, it is reasonable to assume that concentrations of residual impurities are increased at the interface in interrupted growth structures which could give rise to additional structure in the PL

spectra.

Low temperature PL is a standard technique used to characterize the quality of semiconductor materials. However, in GaAs QW structures in which light-hole (LH) and heavy-hole (HH) exciton energies are split due to spatial confinement, only states associated with HH excitons are populated at low temperatures and, therefore, observable in PL. Luminescence due to bound excitons or impurity transitions is usually also present, complicating the identification of the PL features. In contrast, PLE provides direct information not only about ground state LH and HH excitons, but also about their excited levels and, further, is much less sensitive to extrinsic transitions. This is a consequence of the fact that PLE spectroscopy is analogous to absorption spectroscopy. Thus, it is a measure of intrinsic transition probabilities independent of thermal population effects.

It is also possible to distinguish between intrinsic and extrinsic processes in PL by utilizing temperature. At higher temperatures, extrinsic transitions become thermalized more rapidly than intrinsic transitions (free exciton) due to their smaller binding energies and thus their intensities become weaker compared with those due to intrinsic processes. Also, higher energy intrinsic transitions, such as the LH excitons, become populated and thus are observable in PL.

In this section, higher temperature PL and PL excitation spectra will be used to discriminate between these two different recombination processes. Furthermore, the dynamics of the energy transfer among these spatially separated excitons will be investigated by measuring the evolution of the low temperature PL spectra as a function of time after laser pulse excitation.

The GaAs-$Al_xGa_{1-x}As$ QW samples studied were grown at GTE Laboratories in a MBE system. The layered structures were grown on (100) silicon-doped GaAs at substrate temperatures ranging from 600 to 620°C at a growth rate of 0.6 μm/hr. Growth interruption was accomplished at each interface by shuttering the ovens producing the Group III elements for ~60 seconds while maintaining an arsenic overpressure. Temperature dependent PL and PLE were obtained on samples mounted strain-free in a variable temperature cryostat. The excitation source was provided by the tunable dye laser system described in Chapter 2 and the luminescence, dispersed by a 3/4 meter double spectrometer, detected by a cooled ITT-F4128F PM tube operated in the photon counting mode. The low temperature time-resolved PL spectra were obtained on samples immersed in superfluid He and excited with the pulse laser system described previously. The laser repetition rate was 4 MHz and pulse width of ~10 ps were obtained. The system was computer operated and several spectra, corresponding to differnt time windows after the laser pulses, could be collected simultaneously with an instrumental response of ~60 ps.

The low temperature PL spectra of single quantum well (SQW) grown using conventional techniques (i.e. no growth interruption), exhibited broad single peaks and the corresponding PLE spectra also showed single peaks at HH and LH exciton energies. However, when growth interruption at each interface was introduced, significant changes in the optical spectra were observed. Figure 5.1[5.12] shows the temperature dependence of the PL spectrum of a 3 nm QW grown using growth interruption. At 5 K (top curve) the spectrum is dominated by two relatively sharp peaks denoted as I (at 1659 meV) and E_{HH1} (at

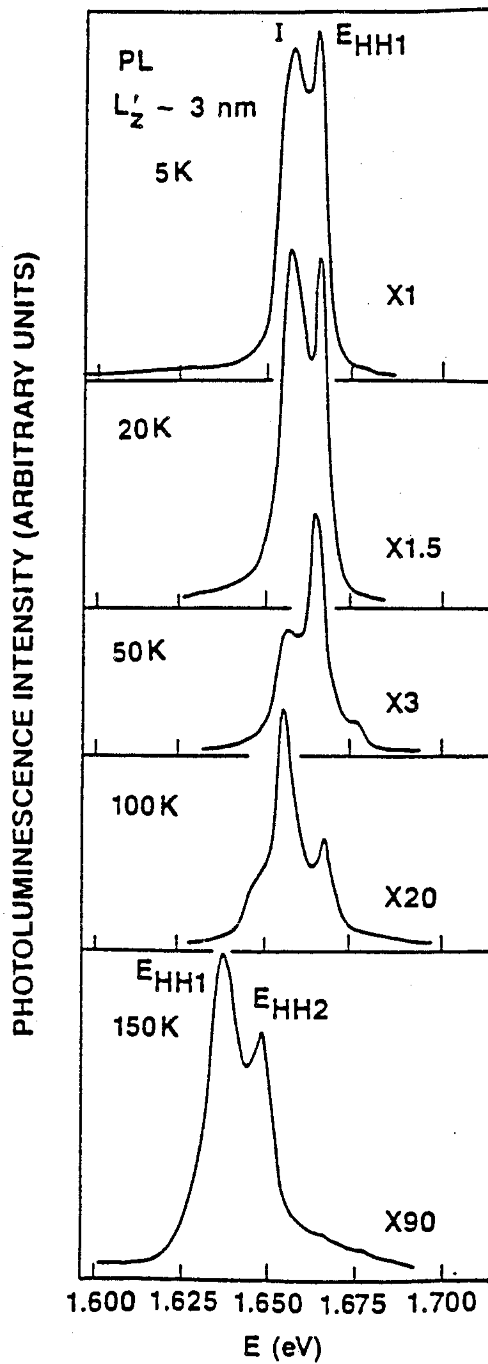

FIG. 5.1 PL spectra of a GaAs/GaAlAs single QW ($L_z' \cong 3$ nm) measured at five different temperatures.

1666 meV). It might appear that these two peaks represent emission from SQW differing in width by a/2. However, their energy difference (~7 meV) is about half predicted by calculations.[5.13] Thus, on the basis of the 5 K PL spectrum alone, the origin of the doublet is unclear. As the sample temperature is increased, the energies of these peaks shift to lower energies, tracking the temperature dependence of the GaAs band gap energy. The intensity of peak I rapidly decreases and by 150 K it has disappeared. This behaviour identifies peak I as being impurity-related. On the high energy side of E_{HH1}, barely visible at low temperatures, a weak peak (labeled E_{HH2}) increases in intensity with increasing temperatures, until by 150 K, it becomes comparable with E_{HH1}. This behaviour is consistent with E_{HH2} being intrinsic in nature, becoming populated and observable in PL at higher temperatures. Theoretical calculations[4.14] for a QW with a 3 nm width produce no energy state near the position of E_{HH2} (about 12 meV above E_{HH1}). However, 12 meV corresponds to the energy difference calculated for excitons in ~3 nm QW differing in width by one monolayer. Thus, while the doublet structure observed in the 5 K PL spectrum in this sample is due to a combination of both extrinsic (I) and intrinsic (E_{HH1}) transitions, the doublet observed at higher temperatures is intrinsic and due to regions of QW width differing by one monolayer within a single well layer.

This interpretation is confirmed by the PLE spectra shown in Figure 5.2.[5.12] Again, as the temperature is increased, the peak energies track the GaAs band gap energy. At all temperatures, the PLE spectrum consists of four main peaks whose energies correlate with emission from free excitons in two QW differing in width by a/2, E_{HH1}, E_{LH1} and E_{HH2},

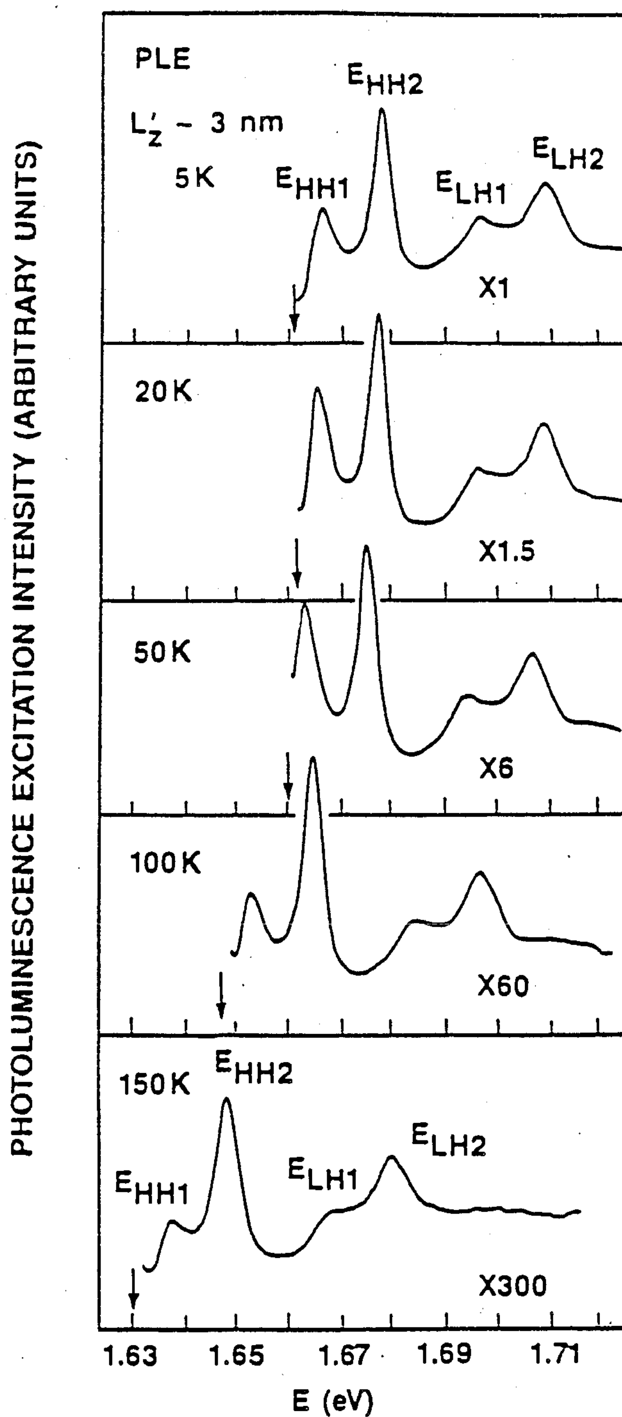

FIG. 5.2 PLE spectra of QW of Figure 5.1 measured at five different temperatures. The arrows indicate the fixed energy settings of the spectrometers.

E_{LH2} label exciton emission peaks from heavy and light excitons in QW with widths $L_{z'} + a/2$ and $L_{z'}$, respectively, where $L_{z'}$ is some average width as will be discussed. The peak positions of E_{HH1} and E_{HH2} and their energy difference are similar to those observed in PL spectra. Thus, both high temperature PL data and the temperature dependent PLE spectra yield the same conclusion. Further, the relative magnitude of E_{HH1} and E_{HH2} in the PLE spectra indicate that at this spot in the sample, the QW corresponding to E_{HH2} is more common than that giving rise to E_{HH1}. Even so, E_{HH2} is not observed in the low temperature PL since E_{HH1}, which is at lower energy, is preferentially occupied.

Such observation of emission peaks associated with large one monolayer growth islands within a single QW layer is consistent with results presented elsewhere.[5.6-5.8] However, if growth interruption at normal (AlGaAs grown on GaAs) and inverted (GaAs grown on AlGaAs) interfaces produces identically smooth interfaces with single monolayer steps, three excitonic peaks associated with QW widths $L_z = n(a/2)$ and $n(a/2) \pm a/2$ should be seen in the optical spectra.[5.10] The observation of only two peaks in this sample can be understood from the model of interface disorder. It has been known for some time that normal interfaces are usually smoother than inverted interfaces due to the superior crystal quality of GaAs as compared with AlGaAs and the lower surface diffusion of Aluminum. Thus, in a QW, one interface (the normal one) would be expected to be smoother than the other as illustrated in Figure 5.3. Assuming that the inverted interface is microscopically rough, a monolayer step fluctuation of the other, smoother interface, will generate a QW layer with two different average widths $L_{z'}$ and $L_{z'}+a/2$. Since the exciton averages over the rapid fluctuations in the

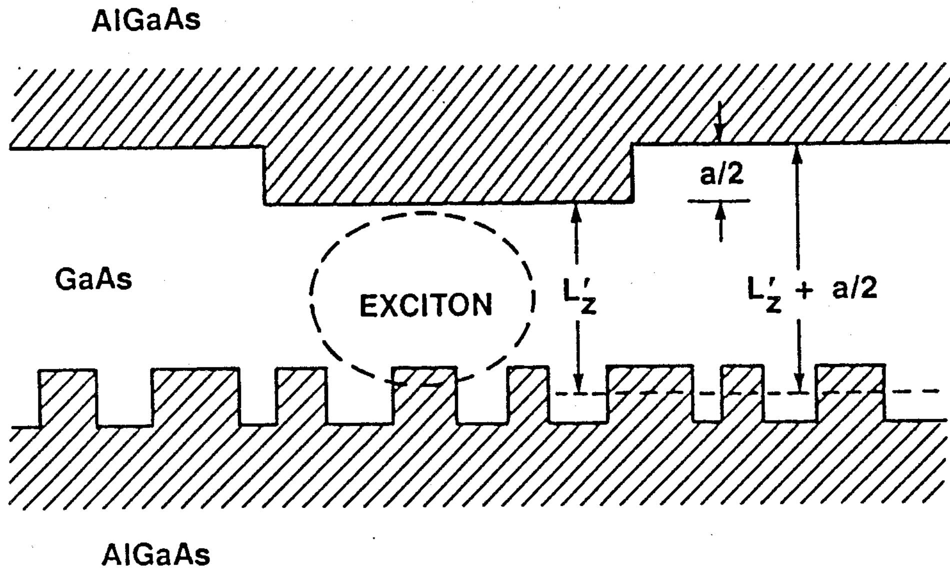

FIG. 5.3 Schematic diagram illustrating the smoothness of the normal and inverted interfaces which leads to QW width averaging L_z' and $L_z' + a/2$ within a single GaAs well layer. The average lateral area of monolayer islands at the normal interface is assumed larger than the two-dimensional exciton diameter.

inverted, rough interface, the exciton peak will be broadened and L_z' need not be equal to an integral number of monolayers. The difference between the two average QW widths, however, will be exactly one monolayer as observed.

This model for the explanation of peaks E_{HH1} and E_{HH2} has implications for the lifetimes of these two states which can be tested by time-resolved PL spectroscopy. The basic idea is that both peaks originate from ground state heavy-hole excitons spatially separated within the layer. In this view, if the excitons are isolated from one another, their lifetimes should be identical. However, since both states are observed simultaneously in the PLE spectrum of E_{HH1}, they must be coupled somehow. This implies that the lifetime of E_{HH2} must be shorter than that of E_{HH1} since this exciton has at least one extra decay channel in addition to those available to E_{HH1}, i.e. coupling to E_{HH1}. This is indeed the case as can be seen in Figure 5.4, which presents the time-resolved PL spectra of this sample. Each of the spectra have been integrated over a time window ranging from about 0.5 ns for the top spectrum, to about 1.5 ns for the bottom spectrum. Immediately after the pulse excitation (top curve), three peaks are clearly seen in the PL spectrum which correspond to the impurity-related peak, I, and the free exciton peaks E_{HH1} and E_{HH2}. At a later time (bottom curve), emission from E_{HH2} has faded. The change in the relative intensities of these three peaks is presented in Figure 5.5, a plot of the logarithm of the luminescence intensity as a function of time after laser pulse excitation. Immediately after excitation, state E_{HH2} has significant population; its intensity, however, decays away much more rapidly than that of either I or E_{HH1}. Typical lifetimes are

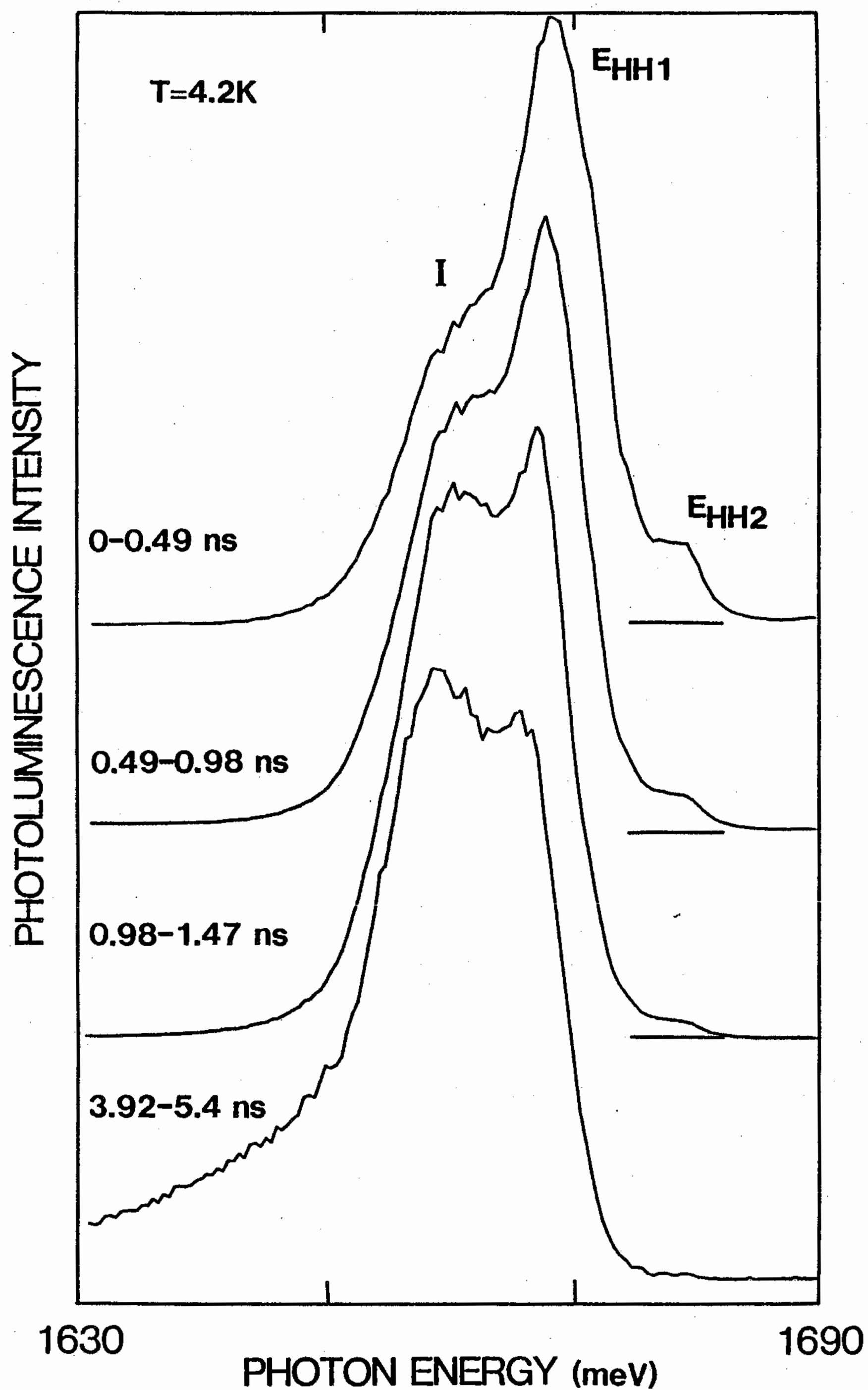

FIG. 5.4 A series of PL spectra showing the evolution of the PL peaks as a function of time after pulse excitation with 725.8 nm, 10 mW/cm^2 radiation. The time range to the left of each spectrum gives the time window over which each spectrum was averaged.

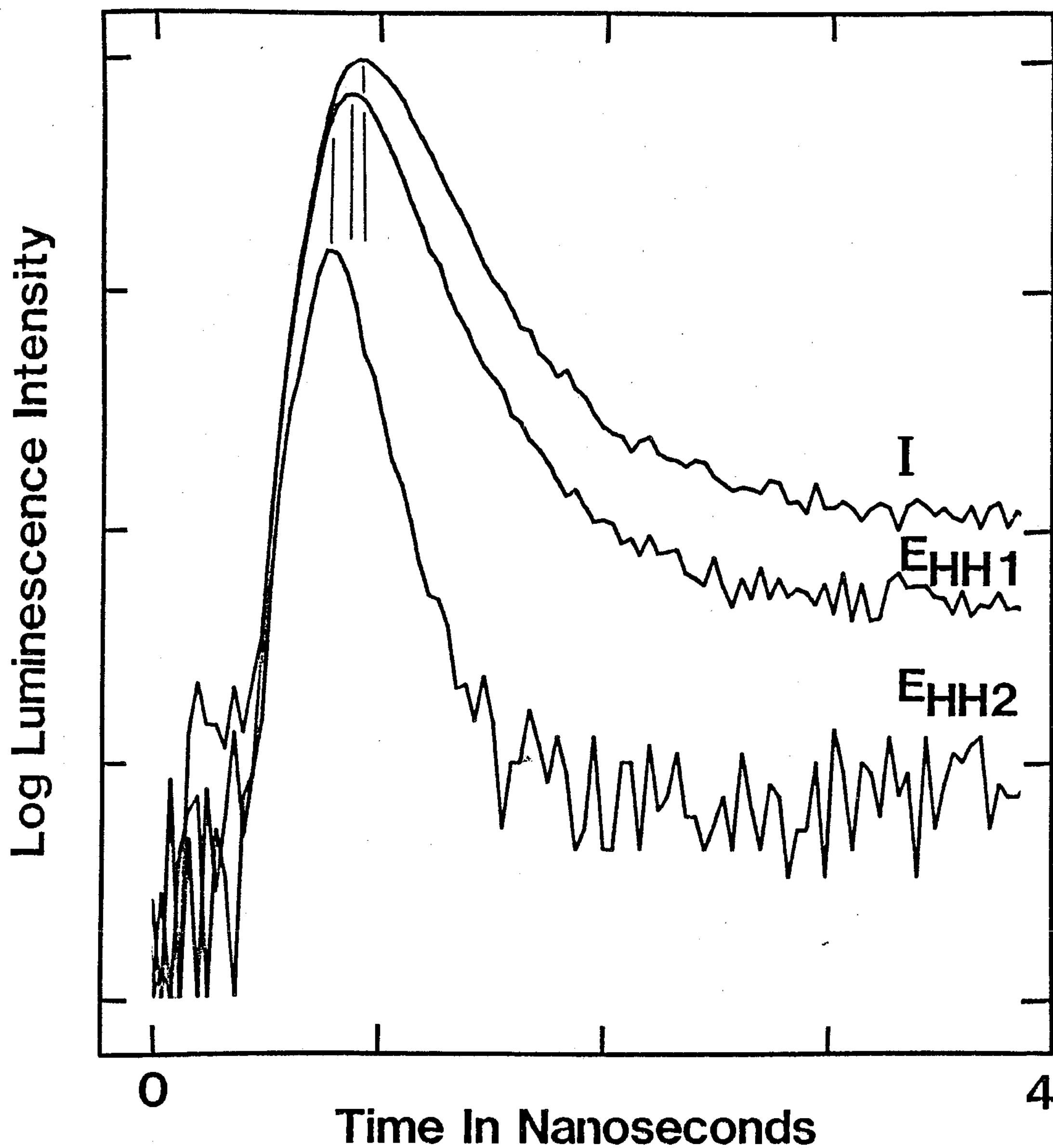

FIG. 5.5 Logarithm of the PL intensities for the three peaks as a function of time after dye laser pulse excitation. The vertical lines mark the time for maximum intensity for each peak. The measured time constants, deconvoluted from the instrumental response of 60 ps are $\tau_I = 240\pm10$ ps, $\tau_{HH1} = 185\pm10$ ps, $\tau_{HH2} = 92\pm10$ ps.

about 200 ps for E_{HH1} and about 100 ps for E_{HH2} compared to 240 ps for the extrinsic I peak. This implies that the lifetime for decay of E_{HH2} to E_{HH1} is about the same as that for E_{HH1} due to all its channels and that there is strong coupling between these spatially separated excitons.

In summary, the importance of temperature dependent PL and PLE spectroscopy have been demonstrated for the correct interpretation of low temperature PL spectra of QW grown using interrupted growth techniques. Finally, using time-resolved spectroscopy, coupling between excitons spatially separated within a single QW layer has been demonstrated.

5.3 Effect of Electric Fields on Excitons in a Coupled Double QW Structure

The effect of an electric field on the optical properties of QW structures has recently attracted a great deal of interest from both fundamental and practical points of view.[5.14-5.17] When an electric field is applied perpendicular to the layers of a QW structure, significant changes in the optical absorption, reflection and PL spectra can be observed and are attributed to modifications of the spatial confinement of the electron and hole wavefunctions.[5.18-5.20] A shift of the absorption edge caused by the quantum-confined Stark effect (QCSE) has been reported,[5.18,5.19] and applications of this effect have already been presented (e.g. high-speed optical modulators[5.21] and electro-optical bistable devices[5.22]). A similar shift to lower energy in the QCSE regime also occurs for the PL peak of the two-dimensional excitons in the QW.

Recently, coupled double quantum well (CDQW) structures have attracted increasing attention since the adjustable coupling of electronic levels in the two wells provides an additional parameter for modifying the properties of bandgap engineered structures and devices.[5.23-5.27] In an isolated, single QW, transitions between the ground state of the electron in the conduction band and the ground states of the heavy- and light-holes in the valence band give rise to a strong doublet in the PLE spectra related to the ground states of heavy- and light-hole excitons. When two SQWs are brought into close proximity, wavefunctions of the confined electrons and holes can overlap, leading to the mixing and splitting levels in the conduction and valence bands in a manner analogous to the splitting observed in the atomic levels of a diatomic molecule. In an unperturbed system of two identical QW separated by a thin penetrable barrier, degenerate single QW states split into symmetric and antisymmetric doublet states. In an isolated QW, the effect of the electric field is to reduce both conduction and valence band energies and exciton binding energies. In a CDQW, however, the split levels of each of the coupled electronic states move in opposite directions as a function of applied electric field, leading to several exciton transitions which shift rapidly to lower or higher energies as the electric field is increased. Transitions between these levels are either essentially interwell-like (spatially indirect) and associated with recombinations of electrons concentrated in one well and holes concentrated in the adjacent well, or intrawell-like (spatially direct). In the case of spatially indirect transitions, the wavefunction confinement will reduce the electron-hole spatial overlap, thus increasing the exciton radiative lifetime.

In a recent paper, Chen and co-workers[5.27] have studied the case of a symmetric CDQW structure, in which the two QW were identical. Low temperature CW photoluminescence, PL excitation and photocurrent spectroscopies were employed to study the different transitions involved in a CDQW as a function of bias voltage. The salient features of their PLE results are the abundance of spectral lines, the positive and negative Stark shifts, and the crossings of some of the levels. The spectral richness results from the breakdown of parity, which usually limits the number of observable optical transitions in symmetric QW. The following discussion will refer to the schematic diagrams of the energy levels given in Figure 5.6.[5.28] In the absence of net internal electric fields, designated the flat-band condition, the coupled electronic states have well-defined symmetries. In this situation, only transitions between electron and hole states of the same symmetry are allowed; transitions between states of opposite symmetry have zero net transition probabilities. This is illustrated on the left-hand side of Figure 5.6, in which symmetry-allowed transitions are denoted by solid lines (1,3,6,8) and symmetry-forbidden transitions by dashed lines (2,4,5,7). When the electric field is applied to the CDQW, wavefunction symmetries are distorted, selection rules are relaxed and all transitions become allowed. Furthermore, tilting of the potential well produces a redistribution of the wavefunctions (Figure 5.6, right). The low-energy coupled states (symmetric states under the flat-band condition) of the valence band concentrate mostly in the left well (designated L in Figure 5.6), while the low-energy coupled level of the conduction band resides primarily in the right well (designated R).

As shown in Figure 5.6, for $E > 0$, intrawell-like transitions in

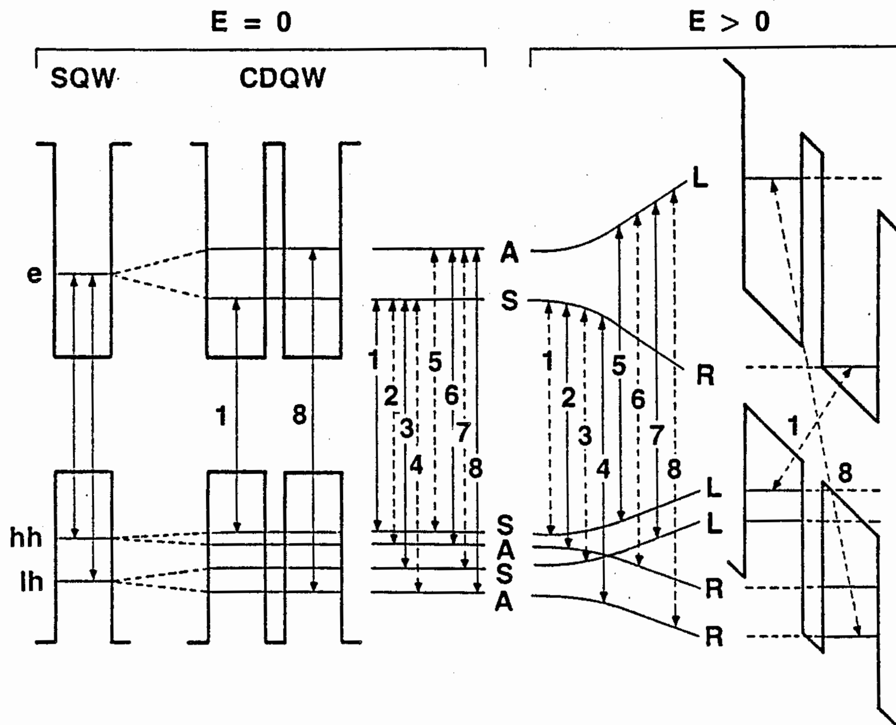

FIG. 5.6 Schematic diagrams of the energy levels of a single QW (left) and a symmetrical CDQW under flat-band conditions (middle), and in the presence of external DC electric fields (right). S and A correspond to symmetric and antisymmetric coupled states under flat-band conditions.

either the R (2 and 4) or L (5 and 7) QW experience the regular QCSE and are weakly affected by the coupling since the energy shifts of the electron and hole states cancel each other. On the other hand, energies of interwell-like transitions undergo much more rapid decreases (1 and 3) or increases (6 and 8) with increasing applied field since these transitions couple electron and hole states either moving toward or away from each other. As shown in Figure 5.6, the symmetry-allowed transitions under flat-band conditions become interwell-like transitions under an applied field (dashed lines), whereas symmetry-forbidden transitions become intrawell-like (solid line). Time-resolved spectroscopy should be of significant utility here since the decay of an interwell-like transition is expected to be much longer than that from an intrawell-like transition. This section examines the conditions under which this increase in lifetime exists. The luminescence decay time of these transitions was measured for various applied voltages in order to examine the effect of the electric field on the dynamics of excitons on a CDQW.

Time-resolved PL was used to study the lowest exciton state in a CDQW p-i-n structure as a function of applied bias voltage. The samples were grown by MBE on an n^+ GaAs buffer and consisted of a single pair of 7.5 nm GaAs QWs (L_z) separated by a 1.8 nm $Al_{0.27}Ga_{0.73}As$ barrier (L_B) surrounded by two 85 nm outer undoped $Al_{0.27}Ga_{0.73}As$ barriers, and a 20 nm p^+ GaAs contact layer on top, all grown on an n^+ GaAs substrate. A Ni/Au-Ge/Au metallization, with 3 minutes 450°C sintering, was employed to obtain an Ohmic contact to the n^+ substrate while Au-5 at.% Zn metallization provided the Ohmic contact to the p^+ layer. The samples, mounted on a sapphire holder, were placed in an immersion

liquid He cryostat and held at a temperature of 1.8 K. The excitation source used for time-resolved PL experiments was the pulsed system described in Chapter 2. The excitation wavelength was 660 nm at an average power density of 30 mW/cm^2. The pulse width was less than 30 ps and the repetition rate was 4 MHz. The luminescence was dispersed by a 3/4 m double spectrometer and detected by a cooled ITT-F4128F photomultiplier tube operated in the photon counting mode. The luminescence decay curves were obtained with the usual time-to-amplitude converter/pulse-height analyzer combination. The total system response to the dye laser excitation pulses had a decay time constant of 70 ps. By operating the system under computer control, eight spectra corresponding to different time windows after the laser pulses could be collected simultaneously.

Figure 5.7 shows typical PLE spectra as a function of bias voltage. The bottom spectrum (taken with a bias of 1.6 V, which corresponds to the flat-band condition since the external electric field exactly cancels the built-in internal field of the p-i-n diode), exhibited four peaks which correspond to the allowed 1, 3 ,6 and 8 exciton transitions (Figure 5.6, E = 0). As the external applied voltage was decreased, (i.e. the net internal electric field increased), additional peaks were observed. These peaks correspond to transitions 2, 4, 5 and 7, which were symmetry forbidden under flat-band conditions. From the energy position of the various transitions, a detailed derivation of all the splittings due to interwell coupling was presented by Chen *et al.*[5.27] The lowest energy peak, an interwell-like transition labeled 1 and peak 3, shifted rapidly to lower energies and lost PL intensity as the applied field was increased. A new, slightly higher energy peak,

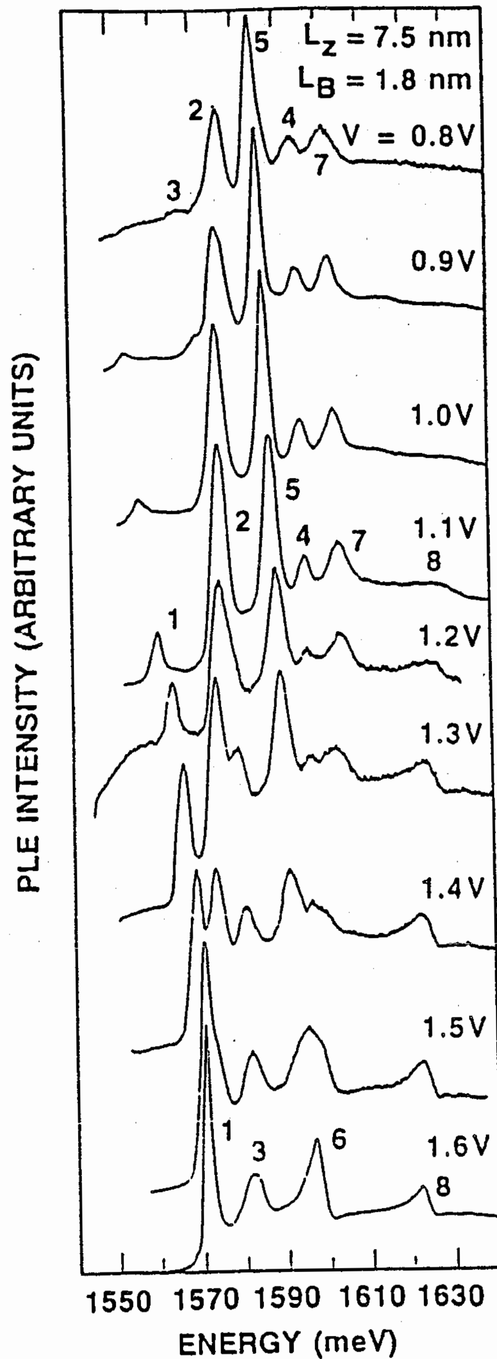

FIG. 5.7 PL excitation spectra of a CDQW under various bias voltages. The bottom spectrum corresponds to the flat-band condition (no net electric field on the CDQW), and, as the bias voltage decreases, the net applied electric field increases. The peaks are labeled according to the notation of Figure 5.6.

labeled 2, quickly became dominant at higher fields. This new transition is due to a heavy-hole intrawell-like transition, which is forbidden under flat-band conditions. The highest energy peak (8) is attributed to an interwell-like light-hole transition. With increasing field, its PL intensity dropped rapidly while its energy increased, in contrast to the behaviour of peaks 1 and 3 (which connect levels which move toward each other with increasing electric field as shown in Figure 5.6). On the other hand, transitions 8 and 6 connect levels moving apart with increasing field. At bias voltage of 0.8 V, the PLE spectrum was dominated by four peaks due to intrawell-like transitions of the R (2 and 4) and L (5 and 7) QW. Interwell-like transitions were much weaker and could barely be detected.

As mentioned previously, the effect of electric fields is to transform a strong allowed transition into a weak one.[5.27] Therefore, transition 1, which is the main transition observed in PL and symmetry-allowed under flat-band, becomes a transition between electrons primarily in one well and holes in the adjacent well when an electric field is applied to the CDQW. Since this transition is essentially indirect in real space (i.e. the electron and hole wavefunction overlap is significantly reduced), its oscillator strength declines rapidly with increasing field and an increase in lifetime is expected. On the other hand, transition 2, which is symmetry-forbidden under flat-band, becomes allowed and remains spatially direct under net internal electric field and thus one would expect a fast transient behaviour. A series of time-resolved PL spectra of the CDQW sample under an external bias voltage of 1 V is shown in Figure 5.8. Immediately after the excitation pulse (0-0.33 ns time window; top curve), two emission peaks are clearly

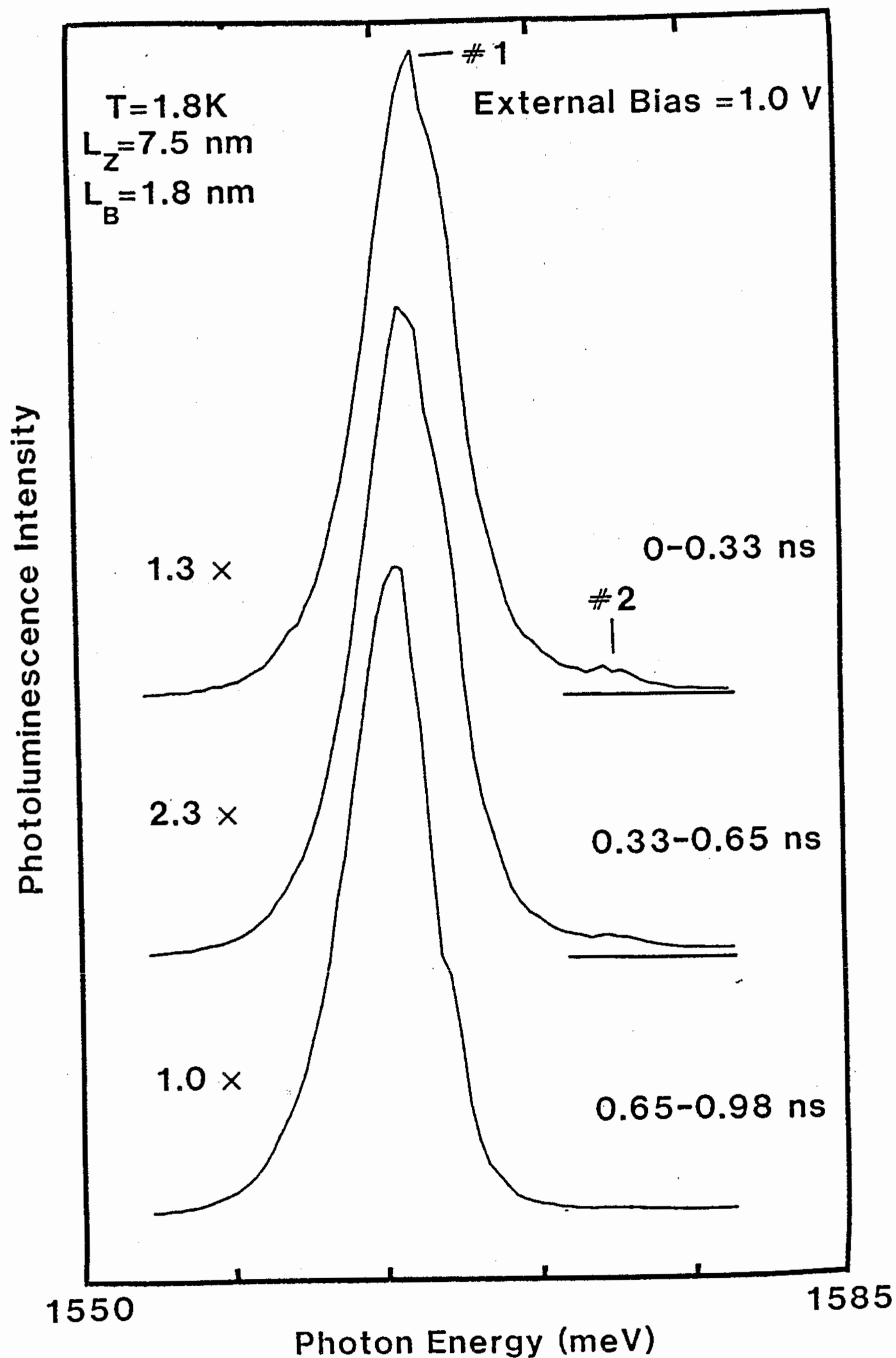

FIG. 5.8 A series of 1.8 K PL spectra showing the evolution of PL peaks as a function of time after pulse excitation. The time windows are indicated on the figure. An external forward bias voltage of 1 V was applied to the sample. The peaks are labeled according to the notation of Fig. 5.6.

visible; transition 1 at 1565.8 meV and transition 2 at 1574.1 meV. At a later time (0.65-0.98 ns time window; bottom curve), emission from transition 2 has faded. The change in the relative intensities of these two peaks for the different time windows is indicative of the different lifetimes for transitions 1 and 2. This is more readily seen in Figure 5.9, which presents luminescence decay curves for peak 1 (under various bias conditions (a-e)) and peak 2 (f). Note the dramatic, tenfold increase in PL lifetimes for peak 1 as the internal electric field on the CDQW is increased from 0 (flat-band condition). The flat-band condition, at which the external voltage exactly cancels the built-in internal electric field of the p-i-n diode, was achieved for an external bias of 1.6 V. One should keep in mind, for the CDQW p-i-n structure used in this study, that as the external bias voltage decreases below 1.6 V, the net internal electric field increases. These results are summarized in Figure 5.10 where the observed exciton transition energies and PL decay times are plotted as a function of forward bias voltage. As one can see, the dependence of the energy of transition 1 on bias voltage is quadratic-like at low fields in agreement with theory.[5.22] From the electric field dependence of the lifetime, peak 1 is assigned to an interwell-like transition involving an electron and a heavy-hole, in good agreement with the CW results obtained previously using the PLE technique.

The energy dependence of transition 2 on the applied external voltage was monitored only for some values of external bias ranging from 0.75 to 1.125 V. This emission, which appeared only weakly in the PL spectra, was observed more clearly using the PLE technique. The spectral position of peak 2 was found to be almost constant from 0.75 to

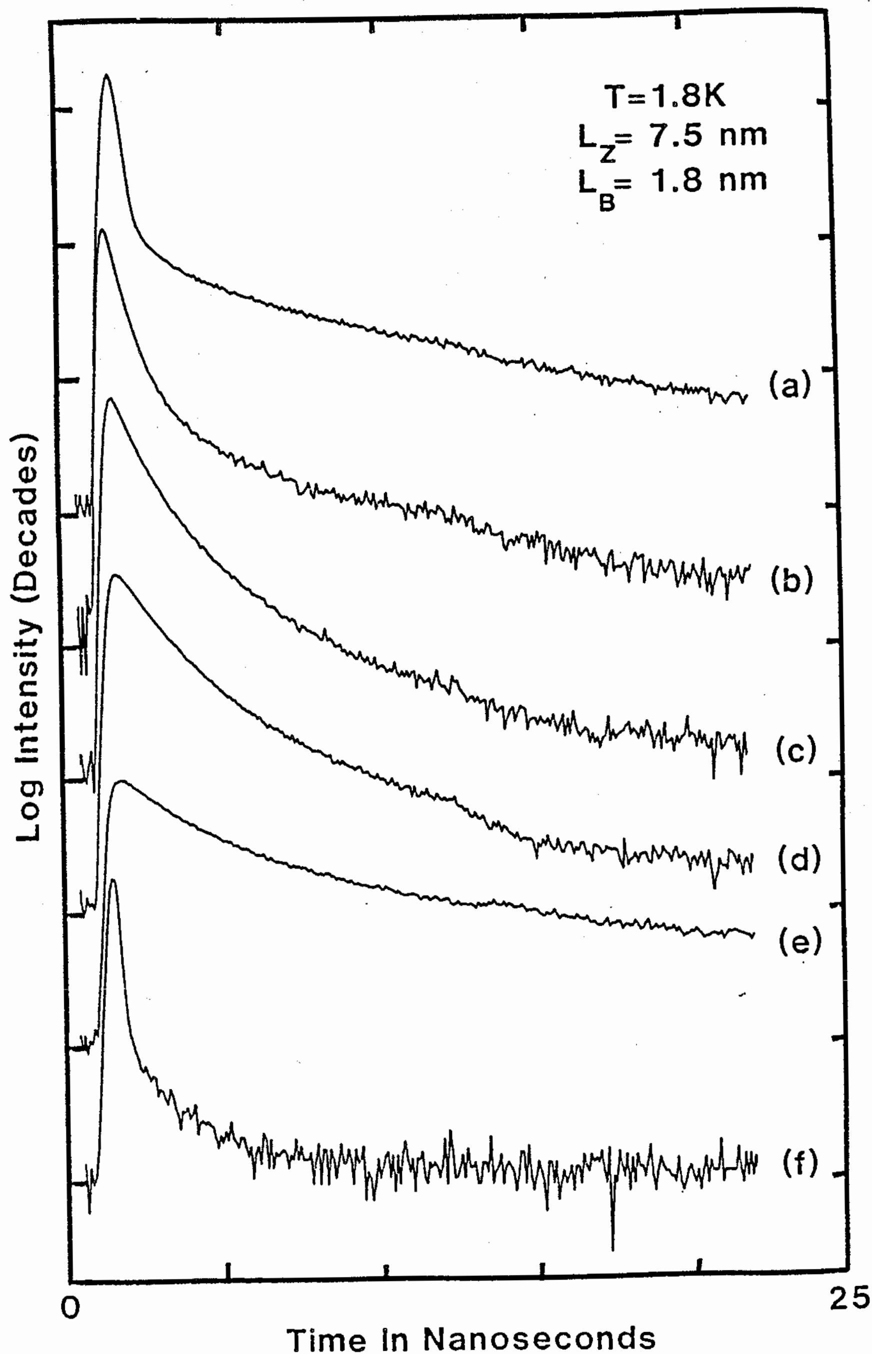

FIG. 5.9 The luminescence decay of exciton peaks (curves (a) to (e) correspond to transition 1 and curve (f) corresponds to transition 2) under various bias voltages. Each of the tick marks on the vertical scale represents one decade of intensity. The transient curves represent decays having time constants of: (a) V = 1.5 V; τ = 0.19±0.01 ns, (b) V = 1.0 V, τ = 0.31±0.01 ns, (c) V = 0.75 V; τ = 0.61±0.01 ns, (d) V = 0.50 V; τ = 1.0±0.01 ns, (e) V = 0.375 V; τ = 1.91±0.01 ns, (f) V = 1.0 V; τ = 0.10±0.01 ns (transition #2).

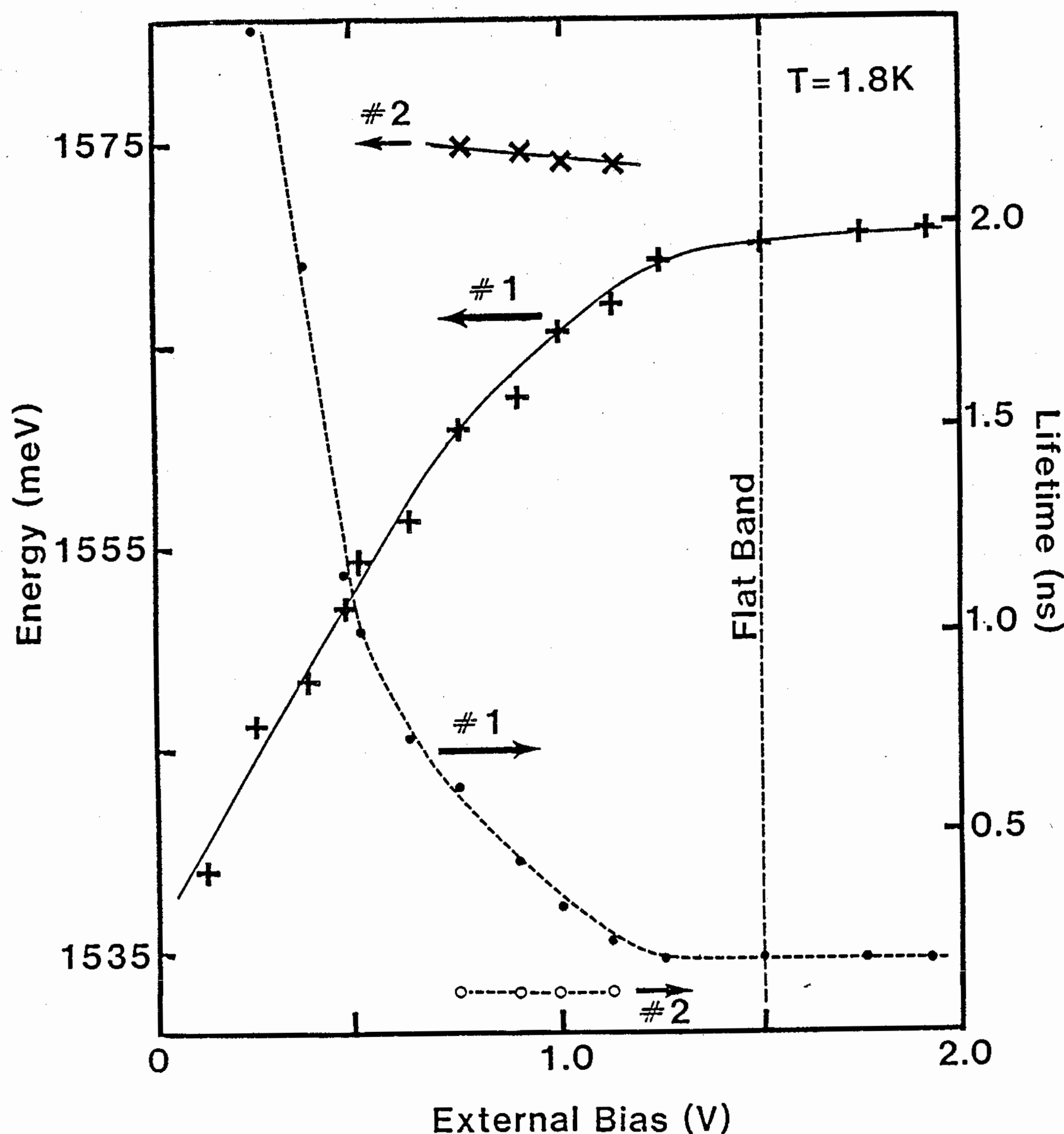

FIG. 5.10 Energies (crosses) and lifetimes (closed circles) of exciton peaks as a function of forward bias voltage measured using time-resolved photoluminescence spectroscopy. Solid and dashed lines through the data points are guides to the eye. The flat-band condition corresponds to the case where there is no net electric field on the CDQW. Due to the p-i-n structure used in this study, the net internal electric field increases as the external bias voltage decreases. The identities of transitions #1 and #2 are discussed in the text.

1.125 volts as shown in Figure 5.10. Transition 1, however, was found to change by more than 6 meV over the same bias range. From these observations, transition 2 is assigned to a heavy-hole intrawell-like transition in agreement with the PLE results obtained. This transition, which is symmetry-forbidden under flat-band conditions, remains spatially direct in an electric field and thus does not lose oscillator strength. The lifetime for such a recombination is expected to be fast because of the spatially direct nature of this transition and thus the strong overlap of the electronic wavefunctions, and also due to relaxation from state 2 to state 1. The transient PL decays of transition 2 were recorded for the various external bias voltages and are also summarized in Figure 5.10. The lifetimes of the state 2 transition were all found to be fast and constant at ~100 ps, independent of the applied field. Transition 2 is faster than transition 1, even under flat-band conditions, since its higher energy permits it one more decay channel than transition 1, i.e. decay to transition 1.

In summary, a detailed optical study of the influence of external electric fields on exciton transitions and lifetimes in a CDQW was presented. This work is strong evidence that the model proposed by Chen *et al.*[5.27] is accurate and details the clear observation of the transformation of a spatially direct exciton transition into a spatially indirect one.

5.4 Concluding Remarks

Advances in solid state device technology in the sixties established III-V materials as a new class of semiconductors for

high-speed electronic devices and highly efficient optical devices. Molecular beam epitaxy was found to be an extremely versatile technique producing single crystal layers with atomic dimensional controls and thus permitted the preparation of novel structures and devices designed to meet specific needs. In the late seventies, single crystal multi-layered structures with dimensions of only a few atomic layers started a new branch of experimental quantum physics. Today, with the ability to produce abrupt interfaces of the order of one monolayer, quantum well devices, such as the CDQW, may be fabricated and studied. This progress has led to a new understanding of the solid state at a fundamental level.

CHAPTER 6

CONCLUSIONS

During the course of this study, it has been shown that new time-resolved spectroscopic techniques can provide very detailed and useful information regarding the electronic states of both the binding centers associated with the BE and the BE themselves.

The results presented in Chapter 3 provided the first definitive proof of the acceptor BE nature of the complex PL line series often observed in MBE grown GaAs. The direct connection between these BE and the lower energy d_n lines was established and the results also confirmed that the Δ band (lines 1-4) consisted of replicas of the higher KP lines resulting from a ground state splitting of the defect acceptors. From the Zeeman data, the symmetry of the defects and the quantum numbers of the initial and final states of the recombination processes were derived. From the previously proposed models, only the exciton recombination at single acceptor pairs or double-acceptor-isoelectronic pairs are successful in explaining the results obtained.

In Chapter 4, intensity dependent PL and lifetime measurements were used jointly in the investigation of excitonic molecules in bulk GaAs, ZnSe and GaAs-$Al_xGa_{1-x}As$ QW. From these results, biexciton binding energies could be estimated and were found to be in good agreement with available theories.

A study of GaAs-$Al_xGa_{1-x}As$ QW concluded that care must be taken in the assignment of the low-energy component of the doublet emission observed in the PL spesctrum. It was due either to the biexciton or an impurity BE, depending on the growth technique used, the quality of the QW, and also on the excitation conditions.

PL techniques were used in Chapter 5 for the characterization of GaAs-$Al_xGa_{1-x}As$ QW. In the first part of the chapter, we have demonstrated the importance of temperature dependent PL and/or PL excitation spectroscopy for the correct interpretation of low temperature PL spectra of QW grown using interrupted growth techniques. Using time-resolved spectroscopy, the coupling between excitons spatially separated within a single QW layer was demonstrated.

Finally, a detailed optical study of the influence of external electric fields on exciton transitions in a coupled-double quantum well was presented. The experimental data provided clear evidence of features unique to this system. In particular, the electric-field-induced energy shifts of tarnsitions 1, 3 and 8 can only be understood within the coupled well model.

REFERENCES

1.1 J. Frenkel, Phys. Rev. **37**, 1276 (1931).

1.2 G.H. Wannier, Phys. Rev. **52**, 191 (1937); N.F. Mott, Proc. R. Soc. A **167**, 384 (1938).

1.3 L.J. Sham and T.M. Rice, Phys. Rev. **144**, 708 (1966).

1.4 H. Barry Bebb and E.W. Williams in *Semiconductors and Semimetals*, Vol. 8, edited by R.K. Willardson and A.C. Beer (1972) p. 279.

1.5 Y. Toyozawa, Prog. Theor. Phys. **20**, 53 (1958).

1.6 W.G. Spitzer in *Semiconductors and Semimetals*, Vol. 3, edited by R.K. Willardson and A.C. Beer (1967) p. 48.

1.7 This section has been inspired by P.J. Dean and D.C. Herbert, in *Topics in Current Physics*, Vol. 14, ed. K. Cho (Springer, Berlin, 1979).

1.8 J.J. Hopfield, Proc. 7th Int. Conf. Phys. Semicond., Paris, ed. Dunod, (1964) p. 725.

1.9 D.C. Herbert, J. Phys. C **10L**, 131 (1977).

1.10 J.R. Haynes, Phys. Rev. Lett. **4**, 361 (1960).

1.11 P.J. Dean in *Luminescence of Crystals, Molecules and Solutions*, ed. by F.E. Williams (Plenum Press, New York 1973) p. 538.

1.12 A. Baldereschi, N.O. Lipari, Proc. 13th Int. Conf. Phys. Semicond., Rome (1976) pp. 595-598.

1.13 C.H. Henry and K. Nassau, Phys. Rev. B **2**, 997 (1970).

1.14 H. Frölich, Adv. Phys. **3**, 325 (1954).

1.15 R.A. Cooke, R.A. Hoult, R.F. Kirkman and R.A. Stradling, J. Phys. D **11**, 945 (1978).

1.16 N.O. Lipari and A. Baldereschi, Phys. Rev. Lett. **25**, 1660 (1970).

1.17 E.I. Rashba and G.E. Gurgeneshrili, Sov. Phys. Solid State **4**, 759 (1962).

1.18 F. Williams, Phys. Status Solidi **25**, 493 (1968).

1.19 D.G. Thomas, M. Gershenzon and F.A. Trumfore, Phys. Rev. **133**, A 269 (1964).

1.20 R. Dingle, Phys. Rev. **184**, 788 (1969).

1.21 L. Esaki and R. Tsu, IBM J. Res. Develop. **14**, 61 (1970).

1.22 L.L. Chang, L. Esaki, W.E. Howard, L. Ludeke and G. Schul, J. Vacuum Sci. Technol. **10**, 655 (1973).

1.23 R. Dingle, W. Wiegmann and C.H. Henry, Phys. Rev. Lett. **33**, 827 (1974).

1.24 E.O. Kane, Phys. Rev. **180**, 852 (1969).

1.25 R. Dingle, C. Weisbush, H.L. Stormer, H. Morkoc and A.Y. Cho, Appl. Phys. Lett. **40**, 507 (1982).

1.26 J.R. Chelikowsky and M.L. Cohen, Phys. Rev. B **14**, 556 (1976).

1.27 C.W. Weisbuch, R.C. Miller, A.C. Gossard and W. Wiegmann, Solid State Commun. **37**, 219 (1981).

1.28 R.C. Miller, D.A. Kleinman, W.A. Norland and A.C. Gossard, Phys. Rev. B **22**, 863 (1980).

2.1 F.J. McClung, R.W. Hellworth, J. Appl. Phys. **33**, 838 (1962).

2.2 H.W. Mocker, R.J. Collins, Appl. Phys. Lett. **7**, 270 (1965).

2.3 Orazio Svelto, *Principles of Lasers* (Plenum, New York 1982).

2.4 W. Demtröder, *Laser Spectroscopy* (Springer, Berlin 1982).

2.5 *Physics of Quantum Electronics*, Vol. 2, *Laser Applications to Optics and Spectroscopy* (Addison-Wesley 1975).

2.6 F.P. Schäfer (ed.), *Dye Lasers*, 2nd Edition, *Topics in Applied Physics*, Vol. 1 (Springer, Berlin, Heidelberg, New York 1978).

2.7 J.W. Small, *The Dye Laser* in *Physics of Quantum Electronics*, Vol. 4 (Addison-Wesley, London 1976).

2.8 A.L. Bloom, J. Opt. Soc. Am. **64**, 447 (1974).

2.9 For a full derivation of equation (2.2), see Ref. 2.4, p. 178.

2.10 O. Svelto, *Principles of Lasers* (Plenum, New York 1982) p. 188.

2.11 A. Yariv, *Quantum Electronics* (Springer, Berlin 1982) p. 262.

2.12 W. Demtröder, *Laser Spectroscopy* (Springer, Berlin 1982) p. 549.

2.13 D.J. Bradley, *Ultrashort Light Pulses*, edited by S.L. Shapiro (Springer, Berlin 1977) p. 17.

2.14 H. Kogelnik, T. Li, Appl. Optics **5**, 1550 (1966).

2.15 A. Yariv, *Quantum Electronics* (Wiley, New York 1975) p. 256.

2.16 T. Steiner, Ph.D. Thesis (Simon Fraser University 1986) p. 45.

2.17 P.W. Smith, Proc. IEEE **58**, 1342 (1970).

2.18 T. Steiner, Ph.D. Thesis (Simon Fraser University 1986) p. 49.

2.19 T. Steiner, Ph.D. Thesis (Simon Fraser University 1986) Appendix 1.

2.20 W.H. Glenn, M.J. Brienza and A.J. DeMaria, Appl. Phys. Lett. **12**, 54 (1968).

2.21 D.J. Bradley in *Ultrashort Light Pulses*, edited by S.L. Shapiro (Springer, Berlin 1977).

2.22 A. Yariv, *Quantum Electronics* (Wiley, New York 1975) p. 356.

2.23 W. Demtröder, *Laser Spectroscopy* (Springer, Berlin 1982) p. 207.

2.24 W.G. McMullan, S. Charbonneau, and M.L.W. Thewalt, Rev. Sci. Instrum. **58**, 1626 (1987).

2.25 A. Hallam, R.E. Imhof, J. Phys. E **13** (1980).

2.26 G.R. Haugen, B.W. Wallin and F.E. Lytie, Rev. Sci. Instrum. **50** (1979).

2.27 EG&G ORTEC 934 Quad constant-fraction 100 MHz discriminator, data sheet.

2.28 EG&G ORTEC 457, Biased time-to-pulse-height converter, data sheet.

2.29 T. Steiner, Ph.D. Thesis (Simon Fraser University 1986) p. 63.

2.30 W.G. McMullan, Ph.D. Thesis (Simon Fraser University 1988).

3.1 A.P. Roth, S. Charbonneau and R.G. Goodchild, J. Appl. Phys. **54**, 5350 (1983).

3.2 Landolt-Börnstein, ed. O. Madelung, M. Schnitz and H. Weiss (Springer, New York 1982) Vol. 17.

3.3 W. Ruhle and W. Klingenstein, Phys. Rev. B **18**, 7011 (1978).

3.4 A.M. White, P.J. Dean, L.L. Taylor, R.C. Clarke, D.J. Ashen and J.B. Mulin, J. Phys. C **5**, 1727 (1972).

3.5 A.M. White, P.J. Dean and B. Day, J. Phys. C **7**, 1400 (1974).

3.6 H. Künzel and K. Ploog, Appl. Phys. Lett. **37**, 416 (1980).

3.7 K. Ploog, H. Künzel and D.M. Collins, J. Appl. Phys. **53**, 6467 (1982).

3.8 H. Künzel and K. Ploog, Inst. Phys. Conf. Ser. No. **56**, 519 (1981).

3.9 P.K. Bhattacharya, H.J. Buhlmann and M. Ilegems, J. Appl. Phys. **53**, 6391 (1982).

3.10 F. Briones and D.M. Collins, J. Electron. Mater. **11**, 847 (1982).

3.11 A. Akimoto, M. Dohsen, M. Arai and N. Watanabe, Appl. Phys. Lett. **45**, 922 (1984).

3.12 K. Kudo, Y. Makita, I. Takayasu, T. Nomura, T. Kobayashi, T. Izumi and T. Matsumori, J. Appl. Phys. **59**, 888 (1986).

3.13 A.P. Roth, R.G. Goodchild, S. Charbonneau and D.F. Williams, J. Appl. Phys. **54**, 3427 (1983).

3.14 D.C. Reynolds, K.K. Bajaj, C.W. Litton, E.B. Smith, P.W.Yu, W.T. Masselink, F. Fisher and H. Morkoc, Solid State Commun. **52**, 685 (1984).

3.15 L. Eaves and D.P. Halliday, J. Phys. C **17**, L705 (1984).

3.16 D.P. Halliday, L. Eaves and P. Davison, 13th Int. Conf. on Defects in Semiconductors, edited by L.C. Kimerling and J.M. Parsey, Coronado, CA, August 12-17 (1984).

3.17 D.C. Reynolds, C.W. Litton, E.B. Smith, K.K. Bajaj, T.C. Collins and M.H. Pilkunh, Phys. Rev. B **28**, 1117 (1983).

3.18 D.C. Reynolds, K.K. Bajaj, C.W. Litton, G. Peters, P.W. Yu, R. Fischer, D. Huang and H. Morkoc, J. Appl. Phys. **60**, 2511 (1986).

3.19 J.P. Contour, G. Neu, M. Leroux, C. Chaix, B. Levesque and P. Etienne, J. Vac. Sci. Technol. B **1**, 811 (1983).

3.20 T. Steiner, M.L.W. Thewalt, E.S. Koteles and J.P. Salerno, Appl. Phys. Lett. **47**, 257 (1985).

3.21 M.S. Skolnick, T.D. Harris, C.W. Tu, T.M. Brennan and M.D. Sturge, Appl. Phys. Lett. **46**, 427 (1985).

3.22 L. Eaves, M.S. Skolnick and D.P. Halliday, J. Phys. C **19**, L445 (1986).

3.23 A.C. Beye and G. Neu, J. Appl. Phys. **58**, 3549 (1985).

3.24 A.C. Beye, B. Gil, G. Neu and C. Vèrié, Phys. Rev. B **37**, 4514 (1988).

3.25 E.V.K. Rao, F. Alexandre, J.M. Masson, M. Alloron and L. Goldstein, J. Appl. Phys. **57**, 503 (1985).

3.26 B.J. Skromme, S.S. Bose, B. Lee, T.S. Lour, T.R. Lepkowski, R.Y. DeJule, G.E. Stillman and J.C.M. Hwang, J. Appl. Phys. **58**, 4685 (1985).

3.27 M.S. Skolnick, C.W. Tu and T.D. Harris, Phys. Rev. B **33**, 8468 (1986).

3.28 M.S. Skolnick, Int. Conf. on Physics of Semiconductors, Stockholm (1986), edited by O.Engstrom (World Scientific, Singapore 1987) p. 1388.

3.29 D.J. Ashen, P.J. Dean, D.T.J. Hurle, J.B. Mullin, A.M. White and P.D. Greene, J. Phys. Chem. Solids **36**, 1041 (1975).

3.30 B.J. Skromme, S.S. Bose and G.E. Stillman, J. Elects. Material **15**, 345 (1986).

3.31 D.W. Kisher, H. Tews and W. Rehm, J. Appl. Phys. **54**, 1332 (1983).

3.32 A.T. Hunter and T.C. McGill, Appl. Phys. Lett. **40**, 169 (1982).

3.33 J.R. Haynes, Phys. Rev. Lett. **4**, 361 (1960).

3.34 *Semiconductors and Semimetals*, Vol. 8, edited by R.K. Willardson and A.C. Beer (1972).

3.35 W. Schairer, D. Bimberg, W. Kottler, K. Cho and M. Schmidt, Phys. Rev. B **13**, 3452 (1976).

3.36 M. Leroux, G. Neu, J.P. Contour, J. Massies and C. Verie, J. Appl. Phys. **59**, 2996 (1986).

3.37 B.V. Shanabrook, W.J. Moore and S.G. Bishop, Phys. Rev. B **33**, 5943 (1986).

3.38 Y. Makita, T. Nomura, M. Yokota, T. Matsumori, T. Izumi, Y. Takeuchi and K. Kudo, Appl. Phys. Lett. **47**, 623 (1985).

3.39 Y. Makita, M. Yokota, T. Nomura, H. Tamoue, I. Takayasu, S. Kataoka, T. Izumi and T. Matsumori, Nucl. Instr. and Meth. **B7/8**, 433 (1985).

4.1 M.A. Lampert, Phys. Rev. Lett. 1, 450 (1958).

4.2 R.K. Wehner, Solid State Commun. **9**, 457 (1969).

4.3 W.F. Brinkman, T.H. Rice and B. Bell, Phys. Rev. **8**, 1570 (1973).

4.4 M. Aven and R.E. Halsted, Phys. Rev. **137**, A228 (1964).

4.5 M. Aven, J. Appl. Phys. **42**, 1204 (1971).

4.6 P.J. Dean, W. Stutius, G.F. Neumark, B.J. Fitzpatrick and R.N. Bhargava, Phys. Rev. B **27**, 2419 (1983).

4.7 P.J. Dean, D.C. Herbert, C.J. Werkhoven, B.J. Fitzpatrick and R.N. Bhargava, Phys. Rev. B **23**, 4888 (1981).

4.8 V.V. Serdyuk, N.N. Korneva and Yu. F. Vaksman, Phys. Stat. Sol.(a) **91**, 173 (1985).

4.9 M. Isshiki, T. Yoshida, T. Tomizono, S. Satoh and K. Igaki, J. Cryst. Growth **73**, 221 (1985).

4.10 M. Isshiki, T. Yoshida, K. Igaki, W. Uchida and S. Suto, J. Cryst. Growth **72**, 162 (1985).

4.11 M. Isshiki, T. Kyotani, K. Masumoto, W. Uchida and S. Suto, Solid State Commun. **62**, 487 (1987).

4.12 Y. Toyozawa, Prog. Theor. Phys. (Kyoto) **20**, 53 (1958).

4.13 A. Mysyrowicz, A. Gun, J.B. Levy, R. Biras, A. Nikitine, Phys. Rev. Lett. **26A**, 615 (1968).

4.14 C.B. á la Guillaume, J.-M. Debever and F. Salvan, Phys. Rev. **177**, 567 (1969).

4.15 H. Saito, S. Shionoya, E. Hamamura, Solid State Commun. **12**, 227 (1973).

4.16 O. Akimoto, E. Hanamura, Solid State Commun. **10**, 253 (1969).

4.17 M. Isshiki, T. Kyotani, M. Masumoto, W. Uchida and S. Suto, Phys. Rev. B **36**, 2568 (1987).

4.18 T. Steiner, M.L.W. Thewalt and R.N. Bhargava, Solid State Commun. **56**, 933 (1985).

4.19 M. Itoh, Y. Nozue, T. Itoh, M. Ueta, S. Satoh and K. Igaki, J. Lumin. **18/19**, 568 (1979).

4.20 G.W. 't Hooft, W.A.J.A. van der Poel, L.W. Molenkamp and C.T. Foxon, Phys. Rev. B **35**, 8281 (1987).

4.21 S. Nikitine, Chapter 2, *Excitons at High Density* (Springer-Verlag) Vol. 73, edited by H. Haken and S. Nikitine (1975).

4.22 S. Shionoya, H. Saito, E. Hanamura and O. Akimoto, Solid State Commun. **12**, 223 (1973).

4.23 K. Cho, Optics Commun. **8**, 412 (1973).

4.24 E.I. Rashba in *Excitons at High Density* (Springer-Verlag) Vol. 73, (1975) p. 151.

4.25 E. Hanamura, Conf. on Luminescence, Leningrad (1972).

4.26 S. Shionoya, H. Saito, E. Hanamura, O. Akimoto, Solid State Commun. **12**, 223 (1973).

4.27 W.F. Brinkman, T.M. Rice, P.W. Anderson and S.T. Chui, Phys. Rev. Lett. **28**, 961 (1972).

4.28 E. Hanamura, J. Phys. Soc. Jpn. **29**, 50 (1970).

4.29 R. Dingle, W. Wiegmann and C.H. Henry, Phys. Rev. Lett. **33**, 827 (1974).

4.30 R. Dingle, C. Weisbuch, H.L. Stormer, H. Morkoc and A.Y. Cho, Appl. Phys. Lett. **40**, 507 (1982).

4.31 C. Weisbuch, R.C. Miller, R. Dingle, A.C. Gossard and W. Wiegmann, Solid State Commun. **37**, 219 (1981).

4.32 R.C. Miller, D.A. Kleinman, A.C. Gossard and O. Munteanu, Phys. Rev. B **25**, 6545 (1982).

4.33 R.C. Miller and D.A. Kleinman, J. Lumin. **30**, 520 (1985).

4.34 D.A. Kleinman, Phys. Rev. B **28**, 871 (1983).

4.35 W.F. Brinkman and T.M. Rice, Phys. Rev. B **7**, 1508 (1973).

4.36 O. Akimoto and E. Hanamura, J. Phys. Soc. Jpn. **33**, 1537 (1972).

4.37 J.R. Haynes, Phys. Rev. Lett. **4**, 361 (1960).

4.38 See, for example, B.S. Elman, Emil S. Koteles, C. Jagannath, Y.J. Chen, S. Charbonneau and M.L.W. Thewalt in *Modern Optical Characterization Techniques for Semiconductors and Semiconductor Devices*, O.J. Glembocki, Fred H. Pollack, J.J. Song, editors, Proc. SPIE 794, p. 44, 1987 and references therein.

4.39 Y. Nomura, K. Shimozaki and M. Isshiki, J. Appl. Phys. **58**, 1864 (1985).

4.40 Y.J. Chen, Emil S. Koteles, Johnson Lee, J.Y. Chi and B. Elman in *Quantum Well and Superlattice Physics*, Gottfried H. Dohler, Joel N. Schulman, editors, Proc. SPIE 792, p. 162, 1987.

4.41 P.L. Gourley and J.P. Wolfe, Phys. Rev. B **20**, 3319 (1979).

4.42 G. Bastard, Phys. Rev. B **24**, 4714 (1981).

4.43 M. Tanaka, H. Sakaki, J. Yoshino and T. Furuta, Surf. Sci. **174**, 65 (1986).

4.44 T. Fukumaga, K.L.I. Kobayashi and H. Nakashima, Surf. Sci. **174**, 71 (1986).

4.45 D. Bimberg, D. Mars, J.W. Miller, R. Bauer and D. Oertels, J. Vac. Sci. Technol. B **4**, 1014 (1986).

5.1 D.C. Reynolds, K.K. Bajaj, C.W. Litton, P.W. Yu, W.J. Masselink, R. Fischer and H. Morkoc, Phys. Rev. B **29**, 7038 (1984).

5.2 M.N. Islam, R.L. Hillman, D.A.B. Miller, D.S. Chemla, A.C. Gossard and J.H. English, Appl. Phys. Lett. **50**, 1098 (1987).

5.3 D.A.B. Miller, D.S. Chemla, T.C. Damen, A.C. Gossard, W. Wiegmann, T.H. Wood and C.A. Burrus, Phys. Rev. B **32**, 1043 (1985).

5.4 D.A.B. Miller, D.S. Chemla, T.C. Damen, A.C. Gossard, W. Wiegmann, T.H. Wood and C.A. Burrus, Phys. Rev. Lett. **53**, 2173 (1984).

5.5 T.H. Wood, C.A. Burrus, D.A.B. Miller, D.S. Chemla, T.C. Damen, A.C. Gossard and W. Wiegmann, IEEE J. Quantum Electron. **21**, 117 (1985).

5.6 C. Weisbuch, R. Dingle, A.C. Gossard and W. Wiegmann, Solid State Commun. **38**, 709 (1981).

5.7 B. Deveaud, J.Y. Emery, A. Chomette, B. Lambert, and M. Baudet, Appl. Phys. Lett. **45**, 1078 (1984).

5.8 B. Deveaud, A. Regreny, J.Y. Emery, and A. Chomette, J. Appl. Phys. **59**, 1633 (1986).

5.9 H. Sakaki, M. Tanaka and J. Yoshino, Jpn. J. Appl. Phys. **24**, L417 (1985).

5.10 T. Hayakawa, T. Suyama, K. Takahashi, M. Kondo, S. Yamamoto, S. Yano and T. Hijikata, Appl. Phys. Lett. **47**, 952 (1985).

5.11 F. Voillot, A. Madhukar, J.Y. Kim, P. Chen, N.M. Cho, W.C. Tang and P.G. Newman, Appl. Phys. Lett. **48**, 1009 (1986).

5.12 B.S. Elman, E.S. Koteles, C. Jagannath, Y.J. Chen, S. Charbonneau and M.L.W. Thewalt in *Interfaces, Superlattices and Thin Films* (Materials Research Society Symposia, Vol. 77), ed. J.D. Dow and I.K. Schuller (1987) p. 461.

5.13 Johnson Lee, Emil S. Koteles and M.O. Vassell, Phys. Rev. B **33**, 5512 (1986).

5.14 E.E. Mendez, G. Bastard, L.L. Chang and L. Esaki, Phys. Rev. B**26**, 7101 (1982).

5.15 G.E. Stillman, C.M. Wolfe, C.O. Bozler and J.A. Rossi, Appl. Phys. Lett. **28**, 544 (1976).

5.16 T.H. Wood, Appl. Phys. Lett. **48**, 1413 (1986), and references therein.

5.17 T.H. Wood, C.A. Burrus, D.A.B. Miller, D.S. Chemla, T.C. Damen, A.C. Gossard and W. Wiegmann, Appl. Phys. Lett. **44**, 16 (1984).

5.18 D.A.B. Miller, D.S. Chemla, T.C. Damen, A.C. Gossard, W. Wiegmann, T.H. Wood and C.A. Burrus, Phys. Rev. **B32**, 1043 (1985).

5.19 D.A.B. Miller, D.S. Chemla, T.C. Damen, A.C. Gossard, W. Wiegmann, T.H. Wood and C.A. Burrus, Phys. Rev. Lett. **53**, 2173 (1984).

5.20 J.A. Kash, E.E. Mendez and H. Morkoc, Appl. Phys. Lett. **46**, 173 (1985).

5.21 T.H. Wood, C.A. Burrus, D.A.B. Miller, D.S. Chemla, T.C. Damen, A.C. Gossard and W. Wiegmann, IEEE J. Quantum Electron. 21, 117 (1985).

5.22 D.A.B. Miller, D.S. Chemla, T.C. Damen, A.C. Gossard, W. Wiegmann, T.H. Wood and C.A. Burrus, Appl. Phys. Lett. **45**, 13 (1984).

5.23 E.J. Austin and M. Jaros, J. Phys. C **19**, 533 (1986).

5.24 H. Kawai, J. Kaneko and N. Watanabe, J. Appl. Phys. **58**, 1263 (1985).

5.25 A. Yariv, C. Lindsey and U. Siran, J. Appl. Phys. **58**, 3669 (1985).

5.26 H.Q. Le, J.J. Zayhowski and W.D. Goodhue, Appl. Phys. Lett. **50**, 1518 (1987).

5.27 Y.J. Chen, Emil S. Koteles, B.S. Elman and C.A. Armiento, Phys. Rev. **B36**, 4562 (1987).

5.28 S. Charbonneau, M.L.W. Thewalt, E.S. Koteles and B. Elman (to be published in Phys. Rev. B, Rapid Communications).